Strong-field ionization of atoms and molecules by short femtosecond laser pulses

Christian Per Juul Martiny

Department of Physics and Astronomy
Aarhus University

PhD thesis
August 2010

This thesis has been submitted to the Faculty of Science at Aarhus University in order to fulfill the requirements for obtaining a PhD degree in physics. The work has been carried out under the supervision of associate professor Lars Bojer Madsen at the Department of Physics and Astronomy.

2nd Edition
Compared to the 1st edition a few minor typographical and grammatical errors have been corrected
This document was compiled and typeset in LaTeX

October 16, 2010

Contents

Acknowledgements

First and foremost, I would like to use the opportunity to thank my supervisor Lars Bojer Madsen for competent supervision during the last four years. Thomas Kim Kjeldsen is gratefully acknowledged for help with several technical issues during my first two years as a PhD student. Furthermore, I would like to thank postdocs Mahmoud Abu-samha and Darko Dimitrovski for a very fruitful collaboration and for many interesting discussions regarding strong-field physics. I have also benefitted from the collaboration with the experimental group of Henrik Stapelfeldt, Department of Chemistry, Aarhus University, and would therefore like to use the opportunity to thank Henrik Stapelfeldt and his group. My fellow students and group members from the Lundbeck Foundation Theoretical Center for Quantum System Research are acknowledged for good and cheerful company during my time in the group. Moreover, Jan Conrad Baggesen and Maj-Britt Suhr Kirketerp are acknowledged for proofreading this thesis. Finally, I would like to thank my family and friends for encouragement and support during the last four years.

Christian Per Juul Martiny, July 2010

List of publications

This thesis is based on the following publications:

- **C. P. J. Martiny** and L. B. Madsen, *Symmetry of Carrier-Envelope Phase Difference Effects in Strong-Field, Few-Cycle Ionization of Atoms and Molecules*, Physical Review Letters **97**, 093001 (2006)
- **C. P. J. Martiny** and L. B. Madsen, *Finite bandwidth effects in strong-field ionization of atoms by few-cycle circularly polarized laser pulses*, Physical Review A. Atomic, Molecular, and Optical Physics **76**, 043416 (2007)
- V. Kumarappan, L. Holmegaard, **C. P. J. Martiny**, C. B. Madsen, T. K. Kjeldsen, S. Viftrup, L. B. Madsen and H. Stapelfeldt, *Multiphoton Electron Angular Distributions from Laser-Aligned* CS_2 *Molecules*, Physical Review Letters **100**, 093006 (2008)
- **C. P. J. Martiny** and L. B. Madsen, *Ellipticity dependence of the validity of the saddle-point method in strong-field ionization by few-cycle laser pulses*, Physical Review A. Atomic, Molecular, and Optical Physics **78**, 043404 (2008)
- **C. P. J. Martiny**, M. Abu-samha and L. B. Madsen, *Counterintuitive angular shifts in the photoelectron momentum distribution for atoms in strong few-cycle circularly polarized laser pulses*, Journal of Physics B: Atomic, Molecular and Optical Physics **42**, 161001 (2009)
- **C. P. J. Martiny**, M. Abu-samha and L. B. Madsen, *Ionization of oriented targets by intense circularly polarized laser pulses: Imprints of orbital angular nodes in the two-dimensional momentum distribution*, Physical Review A. Atomic, Molecular, and Optical Physics **81**, 063418 (2010)

- D. Dimitrovski, **C. P. J. Martiny** and L. B. Madsen, *Strong-field ionization of polar molecules: Stark shift corrected strong-field approximation*. Submitted to Physical Review A. Atomic, Molecular, and Optical Physics

Additional publications:

- L. Holmegaard, J. L. Hansen, L. Kalhøj, S. L. Kragh, H. Stapelfeldt, F. Filsinger, J. Küpper, G. Meijer, D. Dimitrovski, M. Abu-samha, **C. P. J. Martiny** and L. B. Madsen, *Photoelectron angular distributions from strong-field ionization of oriented molecules*, Nature Physics **6**, 428 (2010)

- J. L. Hansen, L. Holmegaard, L. Kalhøj, S. L. Kragh, H. Stapelfeldt, F. Filsinger, J. Küpper, G. Meijer, D. Dimitrovski, M. Abu-samha, **C. P. J. Martiny** and L. B. Madsen, *Ionization of oriented asymmetric top molecules by intense circularly polarized femtosecond laser pulses*. Submitted to Physical Review A. Atomic, Molecular, and Optical Physics

CHAPTER 1

Introduction

The laser was first demonstrated, by T. Maiman at Hughes Research Laboratories, 50 years ago and despite being as considered a curiosity at first the development of the laser has lead to an enormous number of different applications ranging from medicine to femtochemistry. It is safe to say, that the development of the laser is one of the most important breakthroughs in science during the 20th century, underlining the importance of basic research in topics which might, at the time, seem to have limited applications. Furthermore, laser technology has revived the field of atomic, molecular and optical physics into a very thriving branch of physics.

There has been a tremendous development in pulsed laser source technology since the first demonstration of the laser. Pulses with a duration of only a few femtoseconds, with stable carrier-envelope phase, and intensities comparable to the Coulomb interaction between the electron and the nuclei ($I = 1.0 \times 10^{13}$ W/cm^2-$I = 1.0 \times 10^{18}$ W/cm^2) are now available for a broad range of wavelengths (800 nm to 2000 nm) [1]. This development has paved the way for exciting new research fields such as attoscience and femtochemistry. The development of femtosecond pulses has paved the way for femtochemistry where femtosecond pulses are used to study chemical reactions, occurring on a femtosecond timescale, in real time, e.g., directly monitoring how bonds are broken or created during chemical reactions [2]. The characteristic timescale for nuclear motion in diatomic molecules is femtoseconds. It is therefore also possible to investigate nuclear motion in real time, using

femtosecond pulses [3]. The typical timescale for the electron dynamics in an atom or molecule can be estimated using the oscillatory period for an electron in the 1s state of hydrogen, being of the order 100 as. This prevents electron dynamics from being studied using femtosecond pulses, femtosecond pulses are simply too long to capture the electron dynamics. However, it is possible to generate XUV attosecond pulses using femtosecond pulses [1, 4], utilizing high-harmonic generation (HHG), and consequently generate pulses short enough to capture electron dynamics within an atom or molecule. Consider an atom ionized by a femtosecond pulse. The ejected electron is shaken back and forth by the field which can drive the electron back towards the residual atom. High-harmonic generation occurs when the electron recombines with the residual atom, emitting the excess energy in one photon with a frequency of $N\omega$, where ω is the laser frequency and N is an integer. Attosecond pulses have already been used to study electronic motion in atoms and solids, electronic excitation and relaxation dynamics [1, 4]. In fact, the development of attosecond pulses has paved the way for a whole new research field, named attoscience, which hold promise for a large number of unprecedented applications. For a recent review see [4].

High-harmonic generation is furthermore used in molecular-orbital tomography [5, 6]. The HHG signal contains information of the ionizing and recombining system and the HHG signal can therefore, if an inversion is possible, be used as a source of information regarding the ultra-fast time-evolution of the initial system [7, 8].

In strong-field physics single ionization stands out as a fundamental process because it triggers the subsequent electron wave packet dynamic in the continuum and hence affects important processes such as HHG. Optimal usage of a process like HHG, or coherent control with few-cycle pulses, requires a detailed knowledge of the first step, namely the ionization step. Strong-field ionization is also a very interesting process in its own right due to a number of interesting phenomena, e.g., carrier-envelope phase effects. Furthermore, measuring the photoelectron angular distribution provides detailed information about the ionizing system and hence pump-probe experiments, where the pump pulse initiates some dynamics and the system subsequently is probed by the ionizing pulse, can be used to gain dynamical information [9, 10].

Ionization by an external electromagnetic field can be divided into three different regimes: (1) The tunneling regime. (2) The multiphoton regime. (3) The over-the-barrier regime. If the laser frequency is sufficiently small we can consider the laser field as quasi-static. The presence of the field modifies the binding potential, as shown in Figure 1.1, allowing the electron to tunnel through the mod-

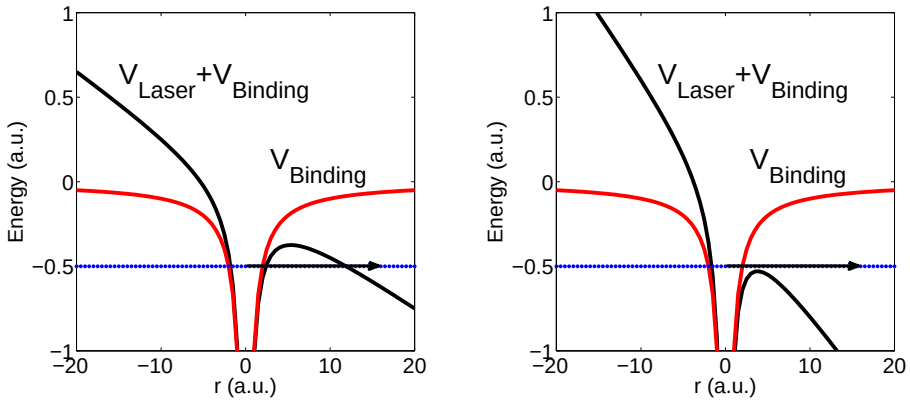

Figure 1.1. *Consider an atom interacting with an (static) electric field. The presence of the field modifies the potential, along the direction of the field, felt by the electrons, as shown in the two plots. The left inset shows the atomic potential, $V_{Binding}$ (red), and the modified atomic potential, $V_{Binding} + V_{Laser}$, in the tunneling regime. The right inset shows the atomic potential, $V_{Binding}$ (red), and the modified atomic potential, $V_{Binding} + V_{Laser}$, in the over-the-barrier regime.*

ified barrier into the continuum. On the other hand, if the laser frequency is large and the intensity low the electron may not have time to tunnel and the ionization process is best described by the absorption of discrete photons, i.e., by multiphoton ionization. Finally, at very high intensities the field completely removes the barrier allowing the electron into the continuum, see Figure 1.1. The distinction between the tunneling regime and the multiphoton regime can be quantified using the Keldysh parameter [11]. The Keldysh parameter is defined as

$$\gamma = \frac{\omega}{\omega_t} = \frac{\omega\sqrt{2I_p}}{E_0}, \tag{1.1}$$

where ω is the laser frequency, ω_t is the frequency associated with the tunneling process, I_p is the ionization potential and E_0 is the electric field amplitude. If $\omega \gg \omega_t$, that is $\gamma \gg 1$, ionization occurs via multiphoton absorption. On the other hand, if $\omega \ll \omega_t$, that is $\gamma \ll 1$, the field can be treated as quasi-static and ionization occurs via tunneling[1]. There is no clear transition between the tunneling and multiphoton regimes and they both contribute in the intermediate region $\gamma \approx 1$. However, studies have shown that tunneling actually dominates in the intermediate

[1]Note that increasing the electric field amplitude takes us into the tunneling regime until we reach the over-the barrier regime.

region, but this tunneling process, coined non-adiabatic tunneling, differs significantly from the quasi-static tunneling seen in the limit $\gamma \ll 1$ [12]. Notice, that the Keldysh parameter, strictly speaking, only has a well defined meaning for long monochromatic pulses. Accordingly, one should be a little careful when using the Keldysh parameter for short pulses.

The photoelectron momentum distribution, i.e., the ionization signal resolved in both direction and energy, is the quantity containing the most information about the ionization process and the photoelectron momentum distribution is therefore the main quantity of interest in this thesis. Regarding strong-field ionization, the first experiments measured the total ionization probability using time of flight techniques, e.g., the total ionization probability as a function of peak intensity. This quantity does not tell you much about the ionization process, energy-resolved or even better momentum resolved measurements contains much more information but are, of course, also more difficult to measure. The process of above-threshold ionization (ATI), requiring energy-resolved measurements, was first observed in 1979 by P. Agostini *et.al* [13]. Above-threshold ionization is a strong-field process where the atom, or molecule, absorbs more photons than needed to overcome the ionization threshold, giving rise to discrete peaks in the photoelectron energy distribution, corresponding to different number of absorbed photons. It is now possible to resolve the direction as well as the energy of the photoelectron using velocity imaging techniques. It is actually possible to measure molecular-frame photoelectron angular distributions using either the COLTRIMS technique or alignment and orientation techniques [14–16].

As the title reveals, the topic of this thesis is a theoretical investigation of strong-field ionization of atoms and molecules using femtosecond pulses, ranging from a few optical cycles up to about 20. We will examine different aspects of the ionization process, e.g., carrier-envelope phase effects for atoms and symmetry effects for molecules. The next 3 chapters are devoted to a review of some of the theoretical framework, namely *ab-initio* theory based on the the time-dependent Schrödinger equation and the strong-field approximation, used in the modeling of strong-field ionization. In addition, we characterized the effect of a change in the carrier-envelope phase from first principle in chapter 3. This characterization is based on the following publications:

- **C. P. J. Martiny** and L. B. Madsen, *Symmetry of Carrier-Envelope Phase Difference Effects in Strong-Field, Few-Cycle Ionization of Atoms and Molecules*, Physical Review Letters **97**, 093001 (2006). (Copyright (2006) by the American Physical Society)

- **C. P. J. Martiny**, M. Abu-samha and L. B. Madsen, *Ionization of oriented targets by intense circularly polarized laser pulses: Imprints of orbital angular nodes in the 2D momentum distribution*, Physical Review A. Atomic, Molecular, and Optical Physics **81**, 063418 (2010). (Copyright (2010) by the American Physical Society)

In chapter 5 and 6, we apply the developed theory, thereby examining different aspects of strong-field ionization. Chapter 5 is based on the following publications:

- **C. P. J. Martiny** and L. B. Madsen, *Finite bandwidth effects in strong-field ionization of atoms by few-cycle circularly polarized laser pulses*, Physical Review A. Atomic, Molecular, and Optical Physics **76**, 043416 (2007). (Copyright (2007) by the American Physical Society)

- **C. P. J. Martiny** and L. B. Madsen, *Ellipticity dependence of the validity of the saddle-point method in strong-field ionization by few-cycle laser pulses*, Physical Review A. Atomic, Molecular, and Optical Physics **78**, 043404 (2008). (Copyright (2008) by the American Physical Society)

- **C. P. J. Martiny**, M. Abu-samha and L. B. Madsen, *Counterintuitive angular shifts in the photoelectron momentum distribution for atoms in strong few-cycle circularly polarized laser pulses*, Journal of Physics B: Atomic, Molecular and Optical Physics **42**, 161001 (2009). (Copyright (2009) by IOP Publishing Ltd)

Chapter 6 is based on the following publications:

- V. Kumarappan, L. Holmegaard, **C. P. J. Martiny**, C. B. Madsen, T. K. Kjeldsen, S. Viftrup, L. B. Madsen and H. Stapelfeldt, *Multiphoton electron angular distributions from laser-aligned* CS_2 *molecules*, Physical Review Letters **100**, 093006 (2008). (Copyright (2008) by the American Physical Society)

- **C. P. J. Martiny**, M. Abu-samha and L. B. Madsen, *Ionization of oriented targets by intense circularly polarized laser pulses: Imprints of orbital angular nodes in the 2D momentum distribution*, Physical Review A. Atomic, Molecular, and Optical Physics **81**, 063418 (2010). (Copyright (2010) by the American Physical Society)

- D. Dimitrovski, **C. P. J. Martiny** and L. B. Madsen, *Strong-field ionization of polar molecules: Stark shift corrected strong-field approximation*. Submitted to Physical Review A. Atomic, Molecular, and Optical Physics.

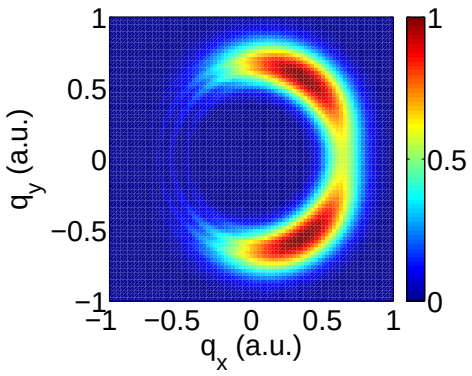

Figure 1.2. *This figure illustrates the linear color scale used throughout this thesis.*

1.1 Conventions

The strong-field ionization process is modeled throughout this thesis using semi-classical theory, where the atomic or molecular system is treated quantum mechanically while the laser field is treated classically. This is a good approximation in strong-fields, where the number of photons can be approximated by a continuous variable, thus making the field classical. We furthermore neglect the influence of the atom or molecule on the laser field. In addition, we are going to use the single active electron approximation (SAE) throughout this thesis, unless stated otherwise. The laser field is assumed to couple primarily with the least bound electron while the other electrons are frozen during the interaction. Hence, our attention is restricted to the least bound electron, with the remaining electrons described by an effective potential.

Molecules have a richer geometry than atoms and are, consequently, also considerably harder to treat theoretically. Luckily, it is possible to simplify the problem using different approximations. The large difference in timescale between the electronic and nuclear motion leads to the Born-Oppenheimer approximation, separating the electronic and nuclear motion. Furthermore, since the characteristic timescale for rotations, 100 fs, is much larger than the interaction times considered in this thesis, the rotational degree of freedom can be considered frozen. The characteristic timescale for vibrations are of the order 10 fs (H_2^+) and hence cannot, in general, be neglected for, say, a 10-cycle 800 nm laser pulses interacting with H_2^+. However, the molecules studied in this thesis are usually much heavier than H_2^+ and it is therefore reasonable to neglect the nuclear vibrations. Accordingly,

with these approximations, we treat the different nuclei as fixed in space during the interaction with the laser pulse.

Atomic units $m_e = e = \hbar = a_0 = 1$ are used throughout this thesis, unless otherwise stated.

Finally, a short comment regarding the color plots shown in this thesis. The color scale is linear, unless stated otherwise, with deep blue corresponding to zero and dark red corresponding to 1 in normalized units. The crossover between blue and yellow corresponds to half the maximum value. The color scale is exemplified in Figure 1.2.

CHAPTER 2

The motion of a charged particle in a classical electromagnetic field

This chapter is meant as a very brief introduction to a few topics which will become useful for us at a later stage. As discussed in the introduction, we treat the laser field classically while the atomic or molecular system is described using quantum theory. We therefore start by reviewing some basic classical electrodynamics which eventually leads to the presentation of the vector potential for a few-cycle laser pulse. Along the way, we also meet the dipole approximation which consists of neglecting the laser field spatial dependence. Next we proceed to present the Lagrange and Hamiltonian equations of motion for an electron in an electromagnetic field. This part is particularly important, since it allows us to write up the quantum mechanical Hamiltonian for an electron in an electromagnetic field, which, of course, is important for a quantum mechanical description of the ionization process. Finally, we present the velocity gauge and length gauge descriptions of an electron in an electromagnetic field. They correspond to two different forms of the light-matter interaction operator and are related via a unitary transformation.

2.1 Classical description of the electromagnetic field

The force on a charged particle in an electromagnetic field is given by the Lorentz force law

$$\vec{F}(\vec{r},t) = q_c(\vec{E}(\vec{r},t) + \vec{v} \times \vec{B}(\vec{r},t)), \tag{2.1}$$

where q_c is the charge of the particle, $\vec{v}$ the velocity, $\vec{E}(\vec{r},t)$ the electric field and $\vec{B}(\vec{r},t)$ the magnetic field. Hence, in order to determine the trajectory of the particle one has to calculate the electromagnetic field, which in turn is generated by the charge and current densities according to Maxwell's four equations [17]

$$\nabla \cdot \vec{E} = \frac{1}{\epsilon_0}\rho, \tag{2.2}$$

$$\nabla \cdot \vec{B} = 0, \tag{2.3}$$

$$\nabla \times \vec{E} = -\frac{\partial \vec{B}}{\partial t}, \tag{2.4}$$

$$\nabla \times \vec{B} = \mu_0 \vec{J} + \epsilon_0 \mu_0 \frac{\partial \vec{E}}{\partial t}, \tag{2.5}$$

where ρ is the charge density and $\vec{J}$ is the current density. Maxwell's equations are, except in the simplest cases, quite difficult to solve. It is therefore often convenient to express the electromagnetic field via the vector and scalar potentials. According to Helmholtz's theorem, $\vec{E}$ and $\vec{B}$ can be written as [18]

$$\vec{E} = -\nabla\Phi - \frac{\partial \vec{A}}{\partial t}, \tag{2.6}$$

$$\vec{B} = \nabla \times \vec{A}, \tag{2.7}$$

where $\Phi(\vec{r},t)$ is the so called scalar potential and $\vec{A}(\vec{r},t)$ is the so called vector potential. Then $\vec{E}$ and $\vec{B}$ automatically fulfill Eq. (2.3) and Eq. (2.4), while Eq. (2.2) and Eq. (2.5) are transformed into the following pair of coupled differential equations [17]

$$\nabla^2\Phi + \frac{\partial}{\partial t}(\nabla \cdot \vec{A}) = -\frac{\rho}{\epsilon_0}, \tag{2.8}$$

$$\left(\nabla^2\vec{A} - \mu_0\epsilon_0\frac{\partial^2\vec{A}}{\partial t^2}\right) - \nabla\left(\nabla\cdot\vec{A} + \mu_0\epsilon_0\frac{\partial\Phi}{\partial t}\right) = -\mu_0\vec{J}. \tag{2.9}$$

The introduction of the potentials reduces the original six dimensional problem to a four dimensional problem. However, Eq. (2.8) and (2.9) are quite complicated and hence it is not obvious that the introduction of Φ and $\vec{A}$ has simplified our goal of solving the four Maxwell equations. What saves us is the concept of gauge freedom. It is easily checked that the gauge transformations $\vec{A} \rightarrow \vec{A} + \nabla f$ and $\Phi \rightarrow \Phi - \frac{\partial f}{\partial t}$, where f is a scalar function, does not change the physical fields, $\vec{E}$ and $\vec{B}$, i.e., we are allowed to modify the vector potential and scalar potential according to these transformations, without changing the physical quantities. This is of large importance, since it allows us to choose a gauge such that the mathematical description of a given problem becomes as simple as possible. There are several different gauges on the market and the optimal choice typically depends on the given physical problem. We will use the so called Coulomb gauge throughout this thesis. In the Coulomb gauge we demand that $\nabla\cdot\vec{A} = 0$, which leads to the following equation for the scalar potential $\nabla^2\Phi = -(1/\epsilon_0)\rho$, i.e., the scalar potential satisfies the Poisson equation. The Coulomb gauge is a good choice if no source is present, which is the case considered here. Since $\rho = 0$, we can take $\Phi = 0$, which together with $\vec{J} = 0$ implies that the vector potential, the electromagnetic field is now completely determine by the vector potential, satisfies the three dimensional wave equation

$$\nabla^2\vec{A} = \frac{1}{c^2}\frac{\partial^2\vec{A}}{\partial t^2}. \tag{2.10}$$

2.1.1 Few-cycle laser pulses

The monochromatic plane wave solution to Eq. (2.10), describing an elliptically polarized electromagnetic field propagating in the z direction with frequency ω, is in general given by [19]

$$\begin{aligned}\vec{A}(\vec{r},t) =& A_0\cos(\omega t - \vec{k}\cdot\vec{r} + \phi)\cos\left(\frac{\epsilon}{2}\right)\vec{e}_x \\ &+ A_0\sin(\omega t - \vec{k}\cdot\vec{r} + \phi)\sin\left(\frac{\epsilon}{2}\right)\vec{e}_y.\end{aligned} \tag{2.11}$$

Here A_0 is the amplitude, ϕ is a phase, $\vec{k} = k_z\vec{e}_z$ is the wave vector and ϵ is the ellipticity describing all degrees of elliptical polarization when varied within the interval $[0;\frac{\pi}{2}]$[1]. The amplitude A_0 is related to the electric field amplitude by $E_0 = \omega A_0$ and the relation to the intensity is $I = \frac{1}{2}\epsilon_0 c E_0^2$.

[1] $\epsilon = 0$ corresponds to linear polarization while $\epsilon = \frac{\pi}{2}$ corresponds to circular.

Atoms and (small) molecules typically extend over distances of the order one Ångstrøm (10^{-10}m), i.e., the wave function describing such systems typically extend over distances of the order one Ångstrøm . The wavelength of the light we are going to consider is, however, of the order 1000 Ångstrøm, thousand times larger than the typical atomic distance. This implies that the light field practically does not change over the spatial region of the atom or molecule, since $kr \ll 1$. As a consequence, we can neglect the spatial dependence of the fields, $\vec{A}(\vec{r},t) = \vec{A}(t)$,

$$\vec{A}(t) = A_0 \left(\cos(\omega t+\phi)\cos\left(\frac{\epsilon}{2}\right)\vec{e}_x + \sin(\omega t+\phi)\sin\left(\frac{\epsilon}{2}\right)\vec{e}_y\right). \qquad (2.12)$$

This is the dipole approximation, which holds as long as

$$ka \ll 1 \Leftrightarrow a \ll \lambda, \qquad (2.13)$$

with λ being the wavelength and a a measure of the linear extend of the atomic or molecular wave function. Notice, that the B-field component of the electromagnetic field vanishes in the dipole approximation, since $\vec{B} = \nabla \times \vec{A}$. The dipole approximation will be assumed implicitly throughout the thesis unless otherwise stated.

It is obvious that a field like Eq. (2.12) with infinite temporal extension cannot describe a few-cycle pulse, i.e., a pulse with a finite duration. Such a short pulse can be produced by a superposition of plane waves, Eq. (2.12), with different frequencies. A popular form for the vector potential describing a few-cycle pulse is

$$\vec{A}(t) = A_0 f(t) \left(\cos(\omega t+\phi)\cos\left(\frac{\epsilon}{2}\right)\vec{e}_x + \sin(\omega t+\phi)\sin\left(\frac{\epsilon}{2}\right)\vec{e}_y\right), \quad (2.14)$$

where f is the envelope. The envelope f is a slowly varying function compared to the carrier wave $\left(\cos(\omega t+\phi)\cos(\frac{\epsilon}{2})\vec{e}_x + \sin(\omega t+\phi)\sin(\frac{\epsilon}{2})\vec{e}_y\right)$. There are several forms of envelopes on the market, e.g., $\sin^2$-, square-, trapezoidal- and Gaussian-envelopes. The Gaussian pulses have the smallest possible frequency width and is therefore the pulses normally produced in experiments. However, Gaussian pulses are somewhat inconvenient from a theoretical modeling perspective, due to the, in principle, infinite pulse length. We will use a $\sin^2-$envelope

$$f(t) = \begin{cases} \sin^2\left(\frac{\omega t}{2N}\right) & t \in [0,\tau] \\ 0 & \text{elsewhere,} \end{cases}$$

where N is the number of optical cycles and τ is the pulse length. This envelope gives pulses that closely resembles Gaussian pulses, especially for the dominant

part of the pulse near $t = \tau/2$. The field described by Eq. (2.14) is no longer monochromatic, it is composed of a large number of different frequencies, with the bandwidth being inversely proportional to the pulse length. The quantity ω is called the central frequency and it is (close to) the most dominant frequency, among the frequencies of which the pulse is composed. The electric field $\vec{E}(t) = -\frac{\partial}{\partial t}\vec{A}(t)$ originating from Eq. (2.14) depends highly on the phase ϕ, as shown in Figure 2.1. A few-cycle pulse is in general quite asymmetric and the phase ϕ determines this

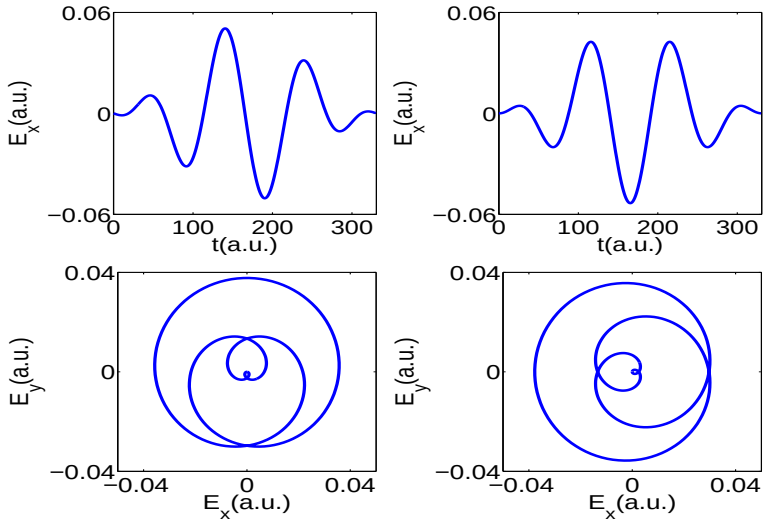

Figure 2.1. *The electric field obtained from Eq. (2.14) for two different polarizations and two different values of CEP. The upper row shows the electric field in the case of linear polarization for $\phi = 0$ (left) and $\phi = \frac{\pi}{2}$ (right). The lower row shows the electric field in the case of circular polarization for $\phi = 0$ (left) and $\phi = \frac{\pi}{2}$ (right). The laser parameters used are peak intensity $I = 1.0 \times 10^{14}$ W/cm^2, central frequency $\omega = 0.057$ (corresponding to a central wavelength of 800 nm) and three optical cycles, $N = 3$.*

asymmetry. It is called the carrier-envelope phase difference (CEP), since it gives the phase difference between the carrier wave and the envelope in the linear case. Notice, that the electric field in the circular case rotates around the z axis by an angle $\Delta\phi$ when the CEP is changed by $\Delta\phi$. We will return to this point in chapter 3, where we fully characterize the response of atomic and molecular systems under a change of the CEP.

The electric field originating from Eq. (2.14) satisfies the relation

$$\int_0^\tau \vec{E}dt = \vec{0}. \tag{2.15}$$

A physical pulse has to obey this relation, otherwise it would contain a DC component ($\vec{E}(\omega = 0) = \int_0^\tau \vec{E}dt$), which is, of course, not possible for a propagating pulse [20].

2.2 The motion of a charged classical particle in an electromagnetic field

The purpose of this section is to review the Lagrangian and Hamiltonian formulations for a charged particle in an electromagnetic field. Let us start with the Lagrangian formulation of the problem. The Lagrange equations of motion states that

$$\frac{d}{dt}\left(\frac{\partial T}{\partial \dot{q}_i}\right) - \frac{\partial T}{\partial q_i} = Q_i, \tag{2.16}$$

where T is the kinetic energy, q_i the generalized coordinates and Q_i the generalized force. We assume that the generalized force can be written on the form

$$Q_i = \frac{d}{dt}\left(\frac{\partial U}{\partial \dot{q}_i}\right) - \frac{\partial U}{\partial q_i}, \tag{2.17}$$

where $U(\{q_i\}, \{\dot{q}_i\}, t)$ is some function. For a conservative system

$$U(\{q_i\}, \{\dot{q}_i\}, t) = U(\{q_i\}) \tag{2.18}$$

is the usual potential energy of the system. When put into Eq. (2.16), this relation leads to the following equation

$$\frac{d}{dt}\left(\frac{\partial L}{\partial \dot{q}_i}\right) - \frac{\partial L}{\partial q_i} = 0, \tag{2.19}$$

where $L = T - U$ is the Lagrangian. Now consider a charged particle interacting with an electromagnetic field described by the scalar potential Φ and vector potential $\vec{A}$. As generalized coordinates we pick the Cartesian coordinates describing the position of the particle $\vec{r} = (x = x_1, y = x_2, z = x_3)$ and therefore $Q_i = F_i = q_c(\vec{E} + \vec{v} \times \vec{B})_i$ ($i = x, y, z$). The electromagnetic force is not conservative and hence we have to find a function U such that

$$F_{x_i} = \frac{d}{dt}\left(\frac{\partial U}{\partial \dot{x}_i}\right) - \frac{\partial U}{\partial x_i}, \tag{2.20}$$

in order to meaningfully define a Lagrangian L. However, it is easy to show that the function U defined by

$$U(\vec{r},\dot{\vec{r}},t) = q_c(\Phi(\vec{r},t) - \dot{\vec{r}}\cdot\vec{A}), \tag{2.21}$$

satisfies Eq. (2.20). Thus, the full dynamics of our particle is governed by Eq. (2.21), together with Eq. (2.19).

Now let us turn to the Hamiltonian formulation. We start by defining the generalized momentum as

$$p_i = \frac{\partial L(\{q_i\},\{\dot{q}_i\},t)}{\partial \dot{q}_i}. \tag{2.22}$$

The step from the Lagrangian formulation to the Hamiltonian formulation is achieved by considering the generalized velocities as a function of the generalized coordinates and the generalized momenta, using Eq. (2.22). Accordingly, the variables in the Lagrangian formulation $\{q_i\},\{\dot{q}_i\}$ is changed into $\{q_i\},\{p_i\}$ in the Hamiltonian formulation. The dynamics is now governed by the Hamilton equations of motion

$$\frac{\partial H}{\partial q_i} = -\frac{dp_i}{dt} \tag{2.23}$$

and

$$\frac{\partial H}{\partial p_i} = \frac{dq_i}{dt}. \tag{2.24}$$

Here

$$H(\{q_i\},\{p_i\},t) = \sum_j p_j\dot{q}_j(\{q_i\},\{p_i\},t) - L, \tag{2.25}$$

is called the Hamiltonian, which, in the case of a conservative system, is nothing but the total energy of the system. Returning to our charged particle interacting with an electromagnetic field, one sees that

$$H(\vec{r},\vec{p},t) = \frac{1}{2m}(\vec{p} - q_c\vec{A})^2 + q_c\Phi, \tag{2.26}$$

where m is the mass of the particle and $\vec{p}$ denotes the canonical momentum of the particle. Hence, the dynamics in the electromagnetic field, within the Hamiltonian formulation, is given by Eq. (2.23), Eq. (2.24) and Eq. (2.26). Equation (2.26) is the main result in this section, since it allows us to obtain the Hamiltonian operator for a charged particle in an electromagnetic field. We obtain

$$\hat{H} = \frac{1}{2m}(\hat{\vec{p}} - q_c\vec{A})^2 + q_c\Phi, \tag{2.27}$$

using canonical quantization. The Hamiltonian for an electron moving in a binding potential $V(\vec{r})$ interacting with an electromagnetic field then reads,

$$\hat{H} = \frac{1}{2m}(\vec{\hat{p}} - q_c\vec{A})^2 + q_c\Phi + V(\vec{r}). \tag{2.28}$$

2.3 Quantum description of a charged particle in an electromagnetic field

The time-dependent Schrödinger equation (TDSE) for an electron, moving in a binding potential, interacting with an electromagnetic field reads

$$i\frac{\partial}{\partial t}\Psi(\vec{r},t) = \left(-\frac{1}{2}\nabla^2 + \vec{A}(t)\cdot\vec{\hat{p}} + \frac{1}{2}\vec{A}(t)^2 + V(\vec{r})\right)\Psi(\vec{r},t), \tag{2.29}$$

if we adopt the Coulomb gauge along with the dipole approximation. Here V is the atomic or molecular binding potential, the term $\vec{A}(\vec{r},t)\cdot\vec{\hat{p}}$ describes the interaction between the active electron and the field while $\frac{1}{2}\vec{A}(\vec{r},t)^2$ is the energy associated with the field itself. Even for the simplest systems, this equation cannot be solved analytically and hence we have to resort to numerical solutions, or to approximate solutions. We will return to this point in chapter 3 and chapter 4, where we describe the general theory for strong-field ionization of atoms and molecules by few-cycle laser pulses.

2.3.1 Velocity and length gauge

It is well known that quantum mechanics is invariant with respect to unitary transformations, i.e., transformations which fulfill the identity

$$\hat{T}^\dagger\hat{T} = \hat{T}\hat{T}^\dagger = 1, \tag{2.30}$$

where 1 denotes the identity operator. Suppose that $\hat{Q}$ is some observable, $\hat{T}$ a unitary operator and that Ψ is a solution to the TDSE, $i\partial\Psi/\partial t = \hat{H}\Psi$. The transformed wave function $\Psi' = \hat{T}\Psi$ then fulfills the transformed Schrödinger equation $i\partial\Psi/\partial t = \hat{H}'\Psi$, with

$$\hat{H}' = \hat{T}\hat{H}\hat{T}^\dagger + i\frac{\partial\hat{T}}{\partial t}\hat{T}^\dagger \tag{2.31}$$

and $\langle\hat{Q}\rangle_\Psi = \langle\Psi|\hat{Q}|\Psi\rangle = \langle\hat{Q}'\rangle_{\Psi'}$, with $\hat{Q}' = \hat{T}\hat{Q}\hat{T}^\dagger$. Hence, instead of describing the system using Ψ we could equally well describe the system using the transformed wave function Ψ', provided that we remember to transform the Hamiltonian and the observables.

Now assume that Ψ^{VG} is a solution to Eq. (2.29), e.g., the wave function for the highest occupied molecular orbital (HOMO) electron in a molecule interacting with an electric field. Transforming Eq. (2.29) using the unitary transformation $\hat{T} = \exp(i\vec{r} \cdot \vec{A})$ gives

$$i\frac{\partial}{\partial t}\Psi^{\mathrm{LG}}(\vec{r},t) = \left(-\frac{1}{2}\nabla^2 + \vec{E}\cdot\vec{r} + V(\vec{r})\right)\Psi^{\mathrm{LG}}(\vec{r},t), \tag{2.32}$$

where $\Psi^{\mathrm{LG}} = \hat{T}\Psi^{\mathrm{VG}}$. The former description is said to be in the velocity gauge, the light-matter interaction operator is $\vec{A}(t)\cdot\vec{\hat{p}} + (1/2)\vec{A}(t)^2$, while the latter is said to be in the length gauge, the light-matter interaction operator is $\vec{E}\cdot\vec{r}$. The two gauges are, of course, completely equivalent and the use of a specific gauge is merely a matter of convenience. Regarding *ab-initio* calculations in the strong-field regime, it is, for example, typically easier to obtain convergence in velocity gauge compared to length gauge [21]. However, this equivalence breaks down when approximations are introduced into the theory, in which case the two gauges can give dramatically different results [22–24]. This is most easily understood by looking at the interaction operators in the two gauges; $\vec{A}\cdot\vec{\hat{p}}$ in velocity gauge is related to the momentum operator $\vec{\hat{p}} = -i\nabla$, while $\vec{r}\cdot\vec{E}$ is related to the position $\vec{r}$. This means that the interaction operator in velocity gauge probes the region of space where the wave function oscillates the most, typically the small r part of the space. On the other hand, the interaction operator in length gauge probes the asymptotic part of space due to the present of $\vec{r}$. Hence, if the invoked approximation is expected to be more accurate for large (small) distances then the above analysis suggest that length (velocity) gauge may be superior to velocity (length) gauge. The argument presented is, of course, not meant as a rigorous derivation and in the end what determines whether our description is acceptable is either a comparison with experimental data or alternatively an *ab-initio* calculation, where the two gauges are bound to give identical results[2]. We will return to this point in chapter 3 and chapter 4.

2.3.2 The Volkov wave function

Consider a free electron interacting with a oscillating electric field $\vec{E}(t)$ described by the vector potential $\vec{A}(t)$. The velocity gauge TDSE for this system reads,

$$i\frac{\partial}{\partial t}\Psi(\vec{r},t) = \left(-\frac{1}{2}\nabla^2 + \vec{A}(t)\cdot\vec{\hat{p}} + \frac{1}{2}\vec{A}(t)^2\right)\Psi(\vec{r},t). \tag{2.33}$$

[2]In fact, gauge equivalence can be used as a test of convergence.

It is easily checked, by direct substitution, that

$$\Psi_{\vec{q}}^{\mathrm{V,VG}}(\vec{r},t) = \frac{1}{\sqrt{(2\pi)^3}} \exp\left(i\vec{q}\cdot\vec{r} - \frac{i}{2}\int_0^t (\vec{q}+\vec{A})^2 dt'\right) \tag{2.34}$$

is a solution. The corresponding wave function in length gauge is given by

$$\Psi_{\vec{q}}^{\mathrm{V,LG}}(\vec{r},t) = \frac{1}{\sqrt{(2\pi)^3}} \exp\left(i(\vec{q}+\vec{A})\cdot\vec{r} - \frac{i}{2}\int_0^t (\vec{q}+\vec{A})^2 dt'\right). \tag{2.35}$$

The two wave functions are called the Volkov wave function in velocity gauge and length gauge, respectively. They describe the quantum mechanical dynamics of a free electron in a laser field and reduce to plane wave solutions when the field is zero. In the strong-field approximation, which is an approximate way of calculating the probability amplitude for strong-field ionization of atoms and molecules, the Volkov wave function is used as an approximation for the final continuum state.

CHAPTER 3

General theory for strong-field ionization of atoms and molecules by few-cycle laser pulses

All information regarding the dynamics of an electron, bound by an electrostatic potential, interacting with an external radiation field is contained in the wave function Ψ of the system. If we, by some method, are able to calculate this quantity we can, in principle, calculate everything of interest, i.e., momentum distribution, energy spectrum, ionization probability etc.

Assume that we want to calculate the momentum distribution, $\partial^3 P/\partial q_x \partial q_y \partial q_z$, which actually is the quantity containing the most information about the ionization process. Scattering theory tells us that

$$\frac{\partial^3 P}{\partial q_x \partial q_y \partial q_z} = \lim_{t\to\infty} |\langle \phi_{\vec{q}} | \mathcal{P}_C \Psi(\vec{r}, \tau + t)\rangle|^2, \tag{3.1}$$

where τ is the pulse length, $\phi_{\vec{q}}$ denotes a plane wave with momentum $\vec{q}$ and $\mathcal{P}_C$ projects onto the continuum. Using this formula requires knowledge of the wave function at large times after the interaction with the pulse, allowing the wave packet to moved into the asymptotic region where the potential can be neglected, making momentum a constant of motion. Hence, Eq. (3.1) is not useful for practical calculations. A better alternative is to use the correct scattering state $\psi_{\vec{q}}$, with

asymptotic momentum $\vec{q}$, of the field-free Hamiltonian

$$\frac{\partial^3 P}{\partial q_x \partial q_y \partial q_z} = |\langle \psi_{\vec{q}} | \Psi(\vec{r}, \tau) \rangle|^2, \tag{3.2}$$

where we only need the wave function at the end of the pulse.

On the other hand, the wave function is strictly necessary if we want to capture the full complexity of the dynamics of our electron [25]. There is no easy way out, if we wish a complete description, we are simply forced to calculate the wave function. This chapter is therefore devoted to a discussion of the ionization process from an *ab-initio* point of view. The main quantity is, of course, the wave function and the relevant dynamics is governed by the TDSE. The TDSE cannot be solved analytically for any strong-field process and hence in order to solve the TDSE one has to invoke different numerical methods. The first two sections are therefore devoted to a brief description on how to solve the TDSE numerically, with particular emphasis on the circularly polarized case, i.e., an atom or diatomic molecule interacting with a circularly polarized laser pulse.

Theoretical investigation of strong-field dynamics usually requires a large element of modeling, however, it turns out that, the physical meaning of a change in the CEP of the pulse can be characterized from first principle. This is the subject of the last section in this chapter.

3.1 Exact description of the ionization process

The wave function satisfies the TDSE which reads

$$i\frac{\partial}{\partial t}\Psi(\vec{r}, t) = \left(-\frac{(-i\nabla + \vec{A}(\vec{r}, t))^2}{2} + V(\vec{r}) \right) \Psi(\vec{r}, t), \tag{3.3}$$

where $\vec{A}$ is the vector potential and $V(\vec{r})$ is the binding potential. Invoking the dipole approximation leads to[1]

$$i\frac{\partial}{\partial t}\Psi(\vec{r}, t) = \left(-\frac{\nabla^2}{2} - i\vec{A}(t) \cdot \nabla + V(\vec{r}) \right) \Psi(\vec{r}, t), \tag{3.4}$$

in velocity gauge and

$$i\frac{\partial}{\partial t}\Psi(\vec{r}, t) = \left(-\frac{\nabla^2}{2} + \vec{E}(t) \cdot \vec{r} + V(\vec{r}) \right) \Psi(\vec{r}, t), \tag{3.5}$$

[1]The term $\vec{A}^2$ is eliminated by applying the unitary transformation $\exp(-i \int_0^t \vec{A}(t')^2 dt')$.

in length gauge. At first glance, it might seem appropriate to work in a Cartesian coordinate system where the kinetic energy operator $\nabla^2 = \partial^2/\partial x^2 + \partial^2/\partial y^2 + \partial^2/\partial z^2$ has a particularly simple form. However, from a numerical point of view, the Cartesian coordinate system is not the optimal choice for atomic and molecular processes due to difficulties in the handling of the Coulomb potential. For spherical symmetric problems spherical coordinates (r, θ, φ) are preferable due to the separability of the TDSE into radial and angular coordinates. Even for non-spherical problems, e.g., an atom interacting with a linearly polarized laser field, the use of spherical coordinates is often preferable compared to Cartesian coordinates.

It is natural, working in spherical coordinates, to introduce the reduced wave function

$$\Phi(r, \theta, \varphi, t) = r\Psi(r, \theta, \varphi, t), \tag{3.6}$$

which satisfies the reduced TDSE

$$i\frac{\partial}{\partial t}\Phi(r, \theta, \varphi, t) = \mathcal{H}^{\mathrm{LG/VG}}\Phi(r, \theta, \varphi, t), \tag{3.7}$$

where

$$\mathcal{H}^{\mathrm{LG}} = -\frac{1}{2}\frac{\partial^2}{\partial r^2} + \frac{\hat{L}^2}{2r^2} + \vec{E}\cdot\vec{r} + V(\vec{r}), \tag{3.8}$$

in length gauge and

$$\mathcal{H}^{\mathrm{VG}} = -\frac{1}{2}\frac{\partial^2}{\partial r^2} + \frac{\hat{L}^2}{2r^2} - i\vec{A}(t)\cdot\left(\nabla - \frac{\hat{r}}{r}\right) + V(\vec{r}), \tag{3.9}$$

in velocity gauge. Here $\hat{L}^2$ denotes the ordinary angular momentum operator. Our ultimate goal is to solve Eq. (3.7) obtaining the reduced wave function and hence the wave function. Needless to say, this cannot be done analytically and we therefore have to resort to numerical methods. In the strong-field regime, it is hard to obtain convergence in length gauge compared to velocity gauge [21], especially if the wave function is expanded in a spherical harmonics basis, the natural choice when using spherical coordinates. This is essentially caused by the fact that the canonical momentum has different meanings in the two gauges. While the kinetic momentum $\Pi = d\vec{r}/dt$ and canonical momentum $\vec{p}$ are equal in length gauge, they differ in the velocity gauge $\Pi = \vec{p} + \vec{A}(t)$. Thus, the canonical momentum is a somewhat more slowly varying variable in the velocity gauge case due to the fact that the strong oscillating field has been subtracted from Π. Since $\vec{L} = \vec{r}\times\vec{p}$, this implies that the size and spread of the angular momentum is smaller in the velocity gauge compared to the length gauge. Accordingly, a large number of spherical

harmonics are needed in order to obtain convergence in the length gauge compared to the velocity gauge. We will therefore restrict the following discussion to the velocity gauge. The solution method used in this thesis is very briefly described in the next section. Regarding the pure computational and numerically issues of the method we refer to [26] for a detailed discussion.

3.1.1 The time-dependent Schrödinger equation: Solution strategy

All the calculations in this thesis are performed using a grid-based split-step method. The reduced wave function is expanded in a basis of spherical harmonics

$$\begin{aligned}\Phi(r,\theta,\varphi,t) &= \sum_{l=0}^{l_{\max}} \sum_{m=-l}^{l} f_{lm}(r,t) Y_{lm}(\theta,\varphi) \\ &= \sum_{lm} f_{lm}(r,t) Y_{lm}(\theta,\varphi), \end{aligned} \tag{3.10}$$

where we represent the radial wave function f_{lm} on an equidistant grid, with step size Δr, extending to $r = r_{\max}$, i.e., the radial coordinate is fixed on a grid while the angular coordinates are allowed to vary continuous. The split-step scheme is based on the time-evolution operator for the system. By definition

$$\Phi(r,\theta,\varphi,t+\Delta t) = U(t+\Delta t)\Phi(r,\theta,\varphi,t), \tag{3.11}$$

where U is the time-evolution operator for the reduced Hamiltonian,

$$i\frac{\partial}{\partial t'}U(t',t) = \mathcal{H}^{\mathrm{VG}}(t')U(t',t). \tag{3.12}$$

If the time-step is sufficiently small, U can be approximated by

$$U(t+\Delta t,t) = \exp\left(-i\mathcal{H}^{\mathrm{VG}}\left(t+\frac{\Delta t}{2}\right)\Delta t\right). \tag{3.13}$$

Now, operating on the reduced wave function with the full operator, U, is difficult due to the different properties of the individual operators. While $-\frac{\partial^2}{\partial r^2}$ is diagonal in momentum space representation, $V(\vec{r})$, for instance, is diagonal in coordinate space representation. From a numerical point of view, it is therefore desirable to split the full time-evolution operator into a product of time-evolution operators, corresponding to each term in the reduced Hamiltonian. However, the different operators do not necessarily commute and hence such a splitting is, in principle,

not possible. Nevertheless

$$\exp\left(-i\mathcal{H}^{\mathrm{VG}}\left(t+\frac{\Delta t}{2}\right)\Delta t\right) = \exp\left(i\frac{\Delta t}{4}\frac{\partial^2}{\partial r^2}\right)\exp\left(i\frac{\Delta t}{2}\frac{\hat{L}^2}{2r^2}\right)$$
$$\times\exp\left(-i\frac{\Delta t}{2}V\right)\exp\left(i\Delta t\vec{A}(t+\Delta t/2)\cdot\left(\nabla-\frac{\hat{r}}{r}\right)\right)\exp\left(-i\frac{\Delta t}{2}V\right)$$
$$\times\exp\left(i\frac{\Delta t}{2}\frac{\hat{L}^2}{2r^2}\right)\exp\left(i\frac{\Delta t}{4}\frac{\partial^2}{\partial r^2}\right)+O(\Delta t^3), \tag{3.14}$$

and as a result we can split the full time-evolution operator, provided that third order terms in the time-step are negligible. Each operator can now be handled in an optimal way, e.g., Crank-Nicolson method or Fourier spectral method for the radial kinetic energy operator and grid-Legendre representation method for the potential [26].

The solution strategy is now clear. First the initial wave function is found by propagating in imaginary time [26]. Then the wave function is calculated at each time-step using Eq. (3.14). The parameters Δr, r_{max}, l_{max} and Δt depend both on the given problem at hand and on the quantity you wish to calculate. It is clear that the calculation, in principle, only is exact in the limit $\Delta r \to 0$, $r_{\mathrm{max}} \to \infty$, $l_{\mathrm{max}} \to \infty$ and $\Delta t \to 0$. For real world numerical calculations, one chooses the parameters in such a way that the relevant result, e.g., momentum distribution, does not change substantially when you change the parameters. For the calculation of the momentum distribution for hydrogen, interacting with three-cycle circularly polarized laser field with central frequency $\omega = 0.057$ (wavelength 800 nm) and peak intensity 1.0×10^{14}W/cm^2, convergence is achieved with $\Delta r = 0.073$, $r_{\mathrm{max}} = 300$, $l_{\mathrm{max}} = 35$ and $\Delta t = 0.01$[2].

Our method is particularly suited for cylindrically problems, e.g., an atom interacting with a linearly polarized field, due to the symmetry of the system. Let the z-axis coincide with the symmetry axis. Then the Hamiltonian commutes with the z component of the angular momentum, $[\hat{H}, \hat{L}_z] = 0$, and thus the magnetic quantum number m is conserved. The φ dependence of the wave function is therefore known and our originally three-dimensional problem reduces to a two-dimensional problem, which is considerable easier to solve compared to the full three-dimensional problem [26]. While an atom interacting with a linearly polarized field represents a cylindrically problem, our main problem, an atom interacting with a circularly polarized field, does not. In the general case ($[\hat{H}, \hat{L}_z] \neq 0$) couplings often introduce a mixing of different m's across l's, which tends to increase the complexity of the

[2] Chapter 5

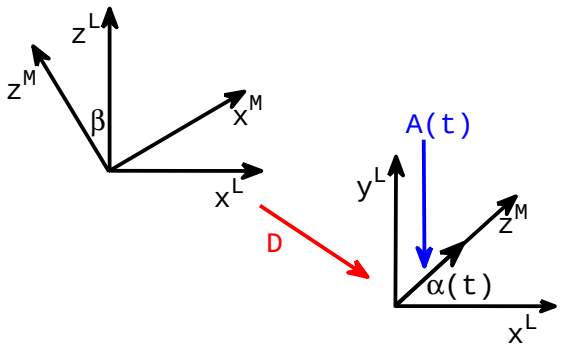

Figure 3.1. *The left inset shows the M/L-frame while the right inset shows the L-frame and the z^M-axis after applying the rotation $\hat{D}$ (see text). The molecule is aligned along the z^M-axis and hence β is the angle between the internuclear axis z^M and the axis of field propagation z^L.*

problem at hand considerably [27,28]. This problem is referred to as the m-mixing problem. The m-mixing problem for atoms in elliptically polarized laser fields was solved several years ago by Muller [27], recently Kjeldsen *et.al.* [28] generalized Muller's method to the special case where the Hamiltonian is a sum of operators cylindrically symmetric around different axis and applied it to the interaction of linearly polarized laser pulses with linear molecules. We will finish this section by applying this method to the case of a diatomic molecule (or atom) interacting with an elliptically polarized laser field described by Eq. (2.14).

The molecular frame is denoted by superscript M while the lab frame is denoted by superscript L (the setup is shown in Figure. 3.1). Let us assume that the molecule is oriented along the z^M-axis and that the L-frame is obtained from the M-frame by the rotation $\mathbf{R}(\alpha = 0, \beta, \gamma = 0)$, where (α, β, γ) denotes the Euler angles [29]. The split-step scheme reads

$$\Phi(r,\theta,\varphi,t+\Delta t) = \exp\left(i\frac{\Delta t}{4}\frac{\partial^2}{\partial r^2}\right)\exp\left(i\frac{\Delta t}{2}\frac{\hat{L}^2}{2r^2}\right)$$
$$\times\exp\left(-i\frac{\Delta t}{2}V\right)\exp\left(i\Delta t\vec{A}(t+\Delta t/2)\cdot\left(\nabla-\frac{\hat{r}}{r}\right)\right)\exp\left(-i\frac{\Delta t}{2}V\right)$$
$$\times\exp\left(i\frac{\Delta t}{2}\frac{\hat{L}^2}{2r^2}\right)\exp\left(i\frac{\Delta t}{4}\frac{\partial^2}{\partial r^2}\right)\Phi(r,\theta,\varphi,t), \tag{3.15}$$

The kinetic energy operators, $\exp(i(\Delta t/4)\partial^2/\partial r^2)$ and $\exp(i(\Delta t/2)\hat{L}^2/2r^2)$, does not induce any m-mixing and, hence, do not pose any problem in the three-dimensional case. The $\exp(-i(\Delta t/2)V)$ operator is cylindrically symmetric in the M-frame, accordingly this operator does not induce any m-mixing if we choose to work in the M-frame. Consequently, the first three operators can be applied separately on each m-system, utilizing the methods from the cylindrical case, provided that we work in the M-frame. Unfortunately, the operator $\exp(i\Delta t\vec{A}(t+\Delta t/2)\cdot(\nabla-\hat{r}/r))$ does induce m-mixing if the wave function is expressed in the M-frame. Nevertheless, this operator does not induce any m-mixing if the wave function is expressed in a frame where the z-axis is aligned along the instantaneous direction of the vector potential[3]. This means that it may be advantageous to represent $\exp(i\Delta t\vec{A}(t+\Delta t/2)\cdot(\nabla-\hat{r}/r))$ and the wave function in such a frame when propagating with this particular operator, since this would allow us to apply this operator separately on each m-system. One question remains, is it possible to effectively transform from the M-frame and back again. Luckily, the answer is yes due to the nice analytical properties of the rotation operator in the spherical harmonic basis. Let

$$\hat{D} = \hat{\mathcal{D}}_P(\alpha(t),\frac{\pi}{2},0)\hat{\mathcal{D}}_P(0,\beta,0), \tag{3.16}$$

where $\hat{\mathcal{D}}_P$ denotes the rotation operator in the passive view[4] [30] and α denotes the time-dependent angle between $\vec{A}(t)$ and $\hat{x}^L$. Thus, we are led to the following propagation scheme in the velocity gauge

$$\Phi(r,\theta,\varphi,t+\Delta t) = \exp\left(i\frac{\Delta t}{4}\frac{\partial^2}{\partial r^2}\right)\exp\left(i\frac{\Delta t}{2}\frac{\hat{L}^2}{2r^2}\right)$$
$$\times\exp\left(-i\frac{\Delta t}{2}V\right)\hat{D}^\dagger\exp\left(i\Delta t\vec{A}(t+\Delta t/2)\cdot\left(\nabla-\frac{\hat{r}}{r}\right)\right)\hat{D}\exp\left(-i\frac{\Delta t}{2}V\right)$$
$$\times\exp\left(i\frac{\Delta t}{2}\frac{\hat{L}^2}{2r^2}\right)\exp\left(i\frac{\Delta t}{4}\frac{\partial^2}{\partial r^2}\right)\Phi(r,\theta,\varphi,t). \tag{3.17}$$

[3]Electric field in the length gauge case.

[4]The coordinate system is rotated and $\hat{\mathcal{D}}_P\Phi$ is the wave function in the new coordinate system.

The passive rotation operator $\hat{\mathcal{D}}_P$ is in general given by

$$\hat{\mathcal{D}}_P(\alpha,\beta,\gamma) = \exp(i\gamma\hat{L}_z)\exp(i\beta\hat{L}_y)\exp(i\alpha\hat{L}_z), \tag{3.18}$$

i.e., the rotation operator in the passive view is just the inverse of the rotation operator in the active view [30]. The distinction between the two is unimportant in the cases involving only a single β rotation [27, 28] but it is essential when dealing with successive rotations around different axes. Hence, it is very important to make a distinction when dealing with a molecule interacting with an elliptically polarized field. It is interesting to note that there exist several erroneous expressions for $\hat{\mathcal{D}}_P$ in the literature. The interested reader is referred to [30] and references therein. The above propagation scheme ensures that we always have axially symmetric operators and hence do not mix different m-states during the propagation of a particular operator. Thus, we have reduced our three-dimensional problem to a number of two-dimensional problems, one for each m-system, in addition to four rotations. This speeds up the propagation of the wave function considerably due to the analytical properties of the rotation operator in the spherical harmonic basis

$$\langle lm'|\hat{\mathcal{D}}_P|lm\rangle = e^{im'\gamma+im\alpha}d^l_{m'm}(-\beta), \tag{3.19}$$

where $d^l_{m'm}$ denotes the Wigner d-rotation function, which can be calculated and applied very effectively from a numerical point of view [26]. The computational complexity of the method scales as $O(l^{2.7}_{\text{max}})$ while the computational complexity of the full three-dimensional approach scales as $O(l^4_{\text{max}})$ [26, 28].

Let us finish this section by showing a few results obtained using the described method. Figure 3.2 shows the probability density $|\Psi_{\text{H}_2^+}(x,y,z=0,t=\tau)|^2$, in the x^Ly^L plane, for H_2^+ interacting with a laser pulses characterized by the parameters: Angular frequency $\omega = 0.057$ (800 nm), peak intensity $I \in \{2.0\times 10^{14}\,\text{W/cm}^2, 5.0\times10^{14}\,\text{W/cm}^2\}$, ellipticity $\epsilon = \pi/2$, $\phi = \pi/2$, $\beta \in \{0^\circ, 90^\circ\}$(see Figure 3.1) and number of optical cycles $N = 2$. We used a time-step of $\tau = 0.005$, 4096 radial grid points equally distributed from zero to $r_{\text{max}} = 600$ and $l_{\text{max}} = 45$. The initial state $\Psi(\vec{r}, t = 0)$ is projected out using the projection operator

$$\hat{\mathcal{P}} = 1 - |\Psi(t=0)\rangle\langle\Psi(t=0)|. \tag{3.20}$$

This is done, in order, to better identify the wave packet dynamics induces by the intense laser pulse. The probability density is clearly seen to consist of a part situated near origo and a liberated wave packet which is being rotated anti-clockwise around the origin in a spiral like orbit. This behavior resembles what we would expect in the case of an atom. The electron is ionized and subsequently driven away

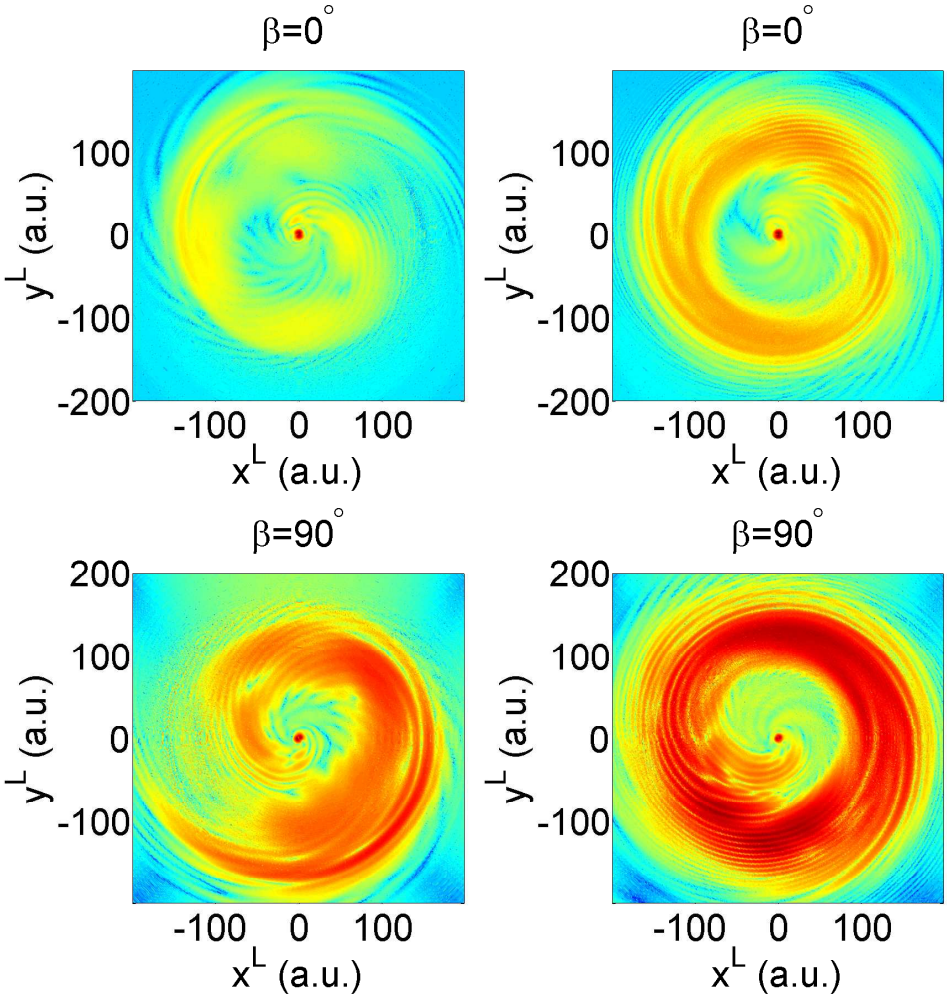

Figure 3.2. *Probability density in xy plane $|\Psi_{H_2^+}(x, y, z = 0, t = \tau)|^2$ for the following choice of parameters: Angular frequency $\omega = 0.057$ (800 nm), peak intensity $I = 5.0 \times 10^{14} W/cm^2$(right panel), $I = 2.0 \times 10^{14} W/cm^2$ (left panel) ,ellipticity $\epsilon = \pi/2$, CEP $\phi = \pi/2$ and number of optical cycles $N = 2$. The color scale is logarithmic.*

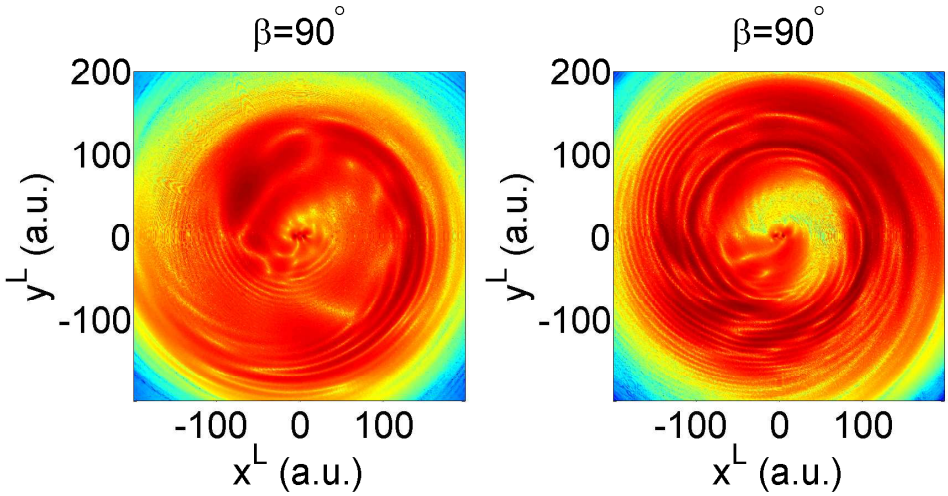

Figure 3.3. *Probability density in xy plane $|\Psi_{H_2^+}(x, y, z = 0, t = \tau)|^2$ for the following choice of parameters: Angular frequency $\omega = 0.057$ (800 nm), peak intensity $I = 5.0 \times 10^{14} W/cm^2$(right), $I = 2.0 \times 10^{14} W/cm^2$ (left), ellipticity $\epsilon = \pi/2$, CEP $\phi = \pi/2$ and number of optical cycles $N = 2$. The color scale is logarithmic.*

from the origin by the laser field. Our results does not show any sign of two-center interference due to the one-center $l = 0$ character of the H_2^+ ground state. However, if we increase the nuclear separation beyond the equilibrium distance we would expect to see signs of two-center interference appear. Figure 3.3 shows results obtained with a nuclear separation of 8 a.u. and indeed we observe sign of two-center interference. The effect is most pronounced in the case of 2.0×10^{14} W/cm^2, compared to the 5.0×10^{14} W/cm^2 case. This can be explain by noting that the quiver radius for the electron increases as a function of intensity.

3.2 Characterization of the CEP for circularly polarized pulses

The temporal shape of the electric field for a few-cycle pulse depends critically on the CEP of the pulse, as shown in Figure 2.1. Consequently, a process like ionization and processes induced by ionization, e.g., HHG, are highly dependent on the CEP. This has motivated a wealth of theoretical and experimental research with emphasis on CEP induced effects, e.g., asymmetries in the photoelectron angular

distribution [31–39].

In this section, we present an exact characterization of the response of atomic and molecular systems under a change of the CEP for circularly polarized laser pulses. This is done by proving the following statement: Consider an atomic or molecular system interacting with a circularly polarized few-cycle laser pulse and assume that the field-free Hamiltonian is invariant under rotations around the propagation direction, $\hat{z}$. If the initial state is invariant with respect to rotations around the propagation direction then

$$\Psi(t;\phi) = \hat{\mathcal{D}}_z(\phi)\Psi(t;\phi=0), \tag{3.21}$$

where $\hat{\mathcal{D}}_z$ is the rotation operator, in the active view, which generates counterclockwise rotations around the z-axis [29].
If the system initially is described by a uniform incoherent mixture of magnetic substates then

$$\left[\frac{\partial^3 P}{\partial q_x \partial q_y \partial q_z}(\mathbf{R}_z(\phi)\vec{q},\phi)\right] = \left[\frac{\partial^3 P}{\partial q_x \partial q_y \partial q_z}(\vec{q},\phi=0)\right], \tag{3.22}$$

with [] denoting the ensemble average [40] and $\mathbf{R}_z$ the 3×3 matrix which generates counterclockwise rotations around the z-axis. Thus, a change $\Delta\phi$ in CEP corresponds to an overall rotation of the wave function (ensemble average of the momentum distribution) around the propagation direction by $\Delta\phi$. Notice, that the physics behind all of this is, of course, that the field itself rotates when we change CEP (see Figure 2.1). It is clear, that the characterization does not hold for $\epsilon \neq \frac{\pi}{2}$, since the field does not have the required symmetry. As shown by Roudnev and Esry, however, it is still possible to find a unitary operator relating $\Psi(\phi=0)$ to $\Psi(\phi\neq 0)$ [38, 39], but it does not have the nice geometrical meaning as in the $\epsilon = \frac{\pi}{2}$ case. CEP effects are in general caused by interferences between different multiphoton channels [38, 39].

We will start out by treating the case where the initial state is invariant with respect to rotations around the propagation direction. The wave function for the system satisfies the TDSE

$$i\frac{\partial}{\partial t}\Psi = \left(\hat{H}_0 + \sum_{j=1}^{n}\vec{A}(\vec{r_j},t;\phi)\cdot\vec{\hat{p}}_j + \frac{nA_0^2}{4}f^2(t)\right)\Psi, \tag{3.23}$$

together with the initial condition $\lim_{t\to-\infty}\Psi = \psi_i$, with ψ_i the state of the system before the pulse. Here $\hat{H}_0$ denotes the field-free Hamiltonian, n the number of

electrons and $\vec{A}$ denotes the vector potential given by Eq. (2.11), with the inclusion of the envelope

$$f(t) = \begin{cases} \sin^2\left(\frac{\omega t - \vec{k}\cdot\vec{r}}{2N}\right) & t \in [0,\tau] \\ 0 & \text{elsewhere.} \end{cases}$$

We are interested in relating this equation to an equation for the $\phi = 0$ case. To this end, we note that the z component of the total angular momentum, $\hat{J}_z$, generates rotations around the z axis, implying that the unitary operator $\hat{\mathcal{D}}_z^\dagger(\phi) = \exp(i\hat{J}_z\phi)$ corresponds to a rotation of our system by an angle $-\phi$ around the z-axis [40]. Since $\hat{H}_0$ is invariant under rotations around the z-axis, $[\hat{H}_0, \hat{J}_z] = 0$, the transformed wave function $\Psi' = \hat{\mathcal{D}}_z^\dagger(\phi)\Psi$ satisfies the equation

$$\begin{aligned} i\frac{\partial}{\partial t}\Psi' =& (\hat{H}_0 + \sum_{j=1}^{n} \hat{\mathcal{D}}_z^\dagger(\phi)\vec{A}(\vec{r}_j,t;\phi)\cdot\vec{\hat{p}}_j\hat{\mathcal{D}}_z(\phi) \\ &+ \frac{nA_0^2}{4}\hat{\mathcal{D}}_z^\dagger(\phi)f^2(\eta)\hat{\mathcal{D}}_z(\phi))\Psi'. \end{aligned} \tag{3.24}$$

Using the Baker-Hausdorff lemma [40]

$$\exp(i\hat{G}\lambda)\hat{A}\exp(-i\hat{G}\lambda) = \hat{A} + i\lambda[\hat{G},\hat{A}] + \frac{i^2\lambda^2}{2!}[\hat{G},[\hat{G},\hat{A}]] + ..., \tag{3.25}$$

we obtain after some algebra (see appendix A)

$$i\frac{\partial}{\partial t}\Psi' = \left(\hat{H}_0 + \sum_{j=1}^{n}\vec{A}(\vec{r}_j,t;0)\cdot\vec{\hat{p}}_j + \frac{nA_0^2}{4}f^2(\eta)\right)\Psi'. \tag{3.26}$$

Furthermore, we note that $\lim_{t\to-\infty}\Psi' = \psi_i$ due to the assumption that the initial state is invariant under rotations around the axis of propagation. Equation (3.26) together with the above initial condition determines the wave function for the system in the $\phi = 0$ case. Hence, we conclude that a change in the CEP from $\phi = 0$ to $\phi = \phi\,'$ corresponds to a rotation of our system around the z-axis by the angle $\phi\,'$. In the above derivation, it is essential that the field-free Hamiltonian $\hat{H}_0$ is invariant to rotations around the z-axis. If this is not the case our proof breaks down. Figure 3.4 presents the LG-SFA (see chapter 4) (q_x, q_y) distribution, $\partial^2 P/\partial q_x \partial q_y$, for strong-field ionization of H(1s) for various values of ϕ, with $I = 5.0\times10^{13}$ W/cm^2, $\omega = 0.057$(800 nm) and three cycles, $N = 3$. The calculations illustrate nicely that a change in ϕ corresponds to a rotation around the z-axis.

Having treated the case where the initial state is invariant with respect to rotations around the propagation direction, we proceed to the more general case where

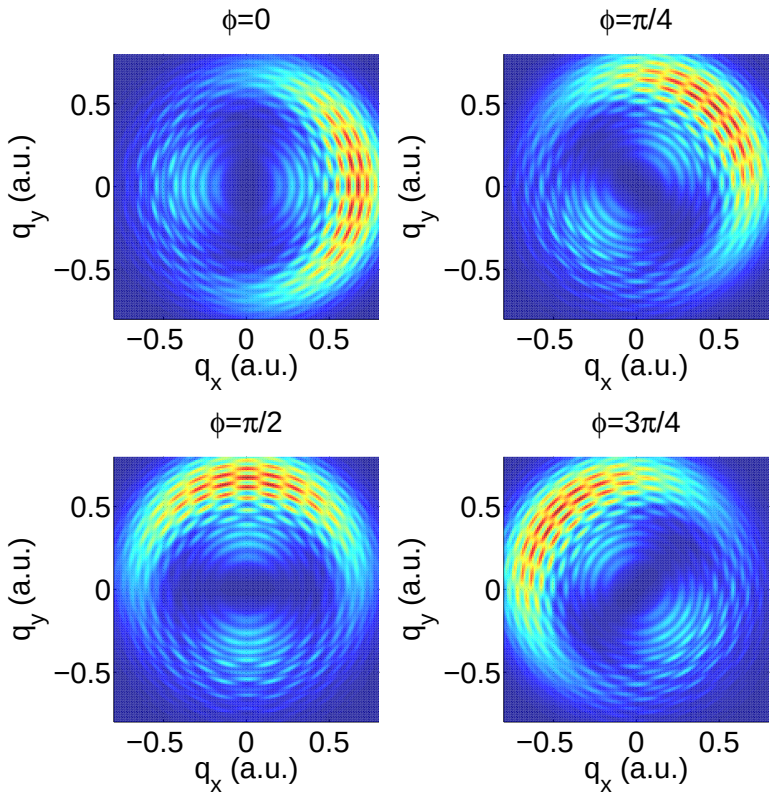

Figure 3.4. *The LG-SFA* (q_x, q_y) *distribution for strong-field ionization of H(1s) for various values of* ϕ*, with* $I = 5.0 \times 10^{13}$ *W/cm*^{2}*,* $\omega = 0.057$ *(*800*nm) and three cycles,* $N = 3$*. The grid size is* $\Delta q_x = \Delta q_y = 0.01$*.*

the system initially is described by a uniform incoherent mixture of magnetic substates. For simplicity, we give this part of the proof within the SAE and the dipole approximation. However, that validity of the characterization does not require the SAE or the dipole approximation as can be checked by going through the steps in the derivation. The ensemble average of $\partial^3 P/\partial q_x \partial q_y \partial q_z$ is defined as [40]

$$\left[\frac{\partial^3 P}{\partial q_x \partial q_y \partial q_z}(\vec{q}, \phi)\right] = \mathrm{Tr}(\rho(t;\phi)\hat{P}_{\vec{q}}), \tag{3.27}$$

where t is any time after the pulse, $\rho(\phi; t)$ is the density matrix of the total system, ϕ the CEP and $\hat{\mathcal{P}}_{\vec{q}} = |\Psi^-_{\vec{q}}\rangle\langle\Psi^-_{\vec{q}}|$ projects onto the exact scattering states $|\Psi^-_{\vec{q}}\rangle$, with

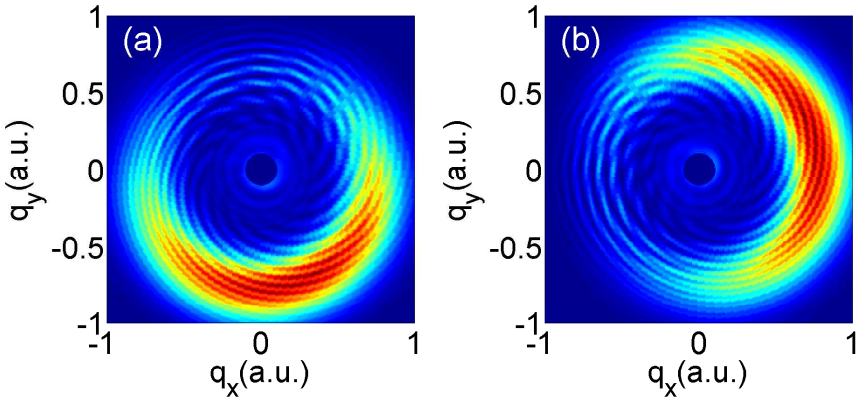

Figure 3.5. *Ensemble average of the SAE, TDSE momentum distributions in the xy polarization plane for Argon initially in a uniform incoherent mixture of $3p_x$ and $3p_y$ states. The laser parameters are: Angular frequency $\omega = 0.057$, corresponding to 800 nm, peak intensity $I = 1.06 \times 10^{14} W/cm^2$, CEP $\phi = -\pi/2$ (a), $\phi = 0$ (b) and number of optical cycles $N = 3$.*

asymptotic momentum $\vec{q}$. The density matrix is given by

$$\rho(t;\phi) = \sum_{M=-J}^{J} P_M |\Psi_{n_Q JM}(t;\phi)\rangle\langle\Psi_{n_Q JM}(t;\phi)|. \tag{3.28}$$

Here $P_M = \frac{1}{2J+1}$ and $|\Psi_{n_Q JM}(t;\phi)\rangle = U(t,0;\phi)|n_Q JM\rangle$, where U is the time-evolution operator for the total system and $|n_Q JM\rangle$ the field-free initial state with J denoting the total angular momentum of the system, M the corresponding magnetic quantum number and n_Q the remaining quantum numbers. We note, in passing, that the Hamiltonian, and hence the time-evolution operator, have a parametric dependence on ϕ through the interaction with the external field. We evaluate the ensemble average Eq. (3.27) using the position-eigenstate basis and thereby obtain

$$\left[\frac{\partial^3 P}{\partial q_x \partial q_y \partial q_z}(\vec{q},\phi)\right] = \frac{1}{2J+1} \sum_{M=-J}^{J} \left| \int (\Psi_{\vec{q}}^{-})^* \Psi_{n_Q JM}(t;\phi) d\vec{r} \right|^2 . \tag{3.29}$$

Using the relation [29]

$$\int D^J_{M'M}(\alpha,\beta,\gamma) D^{J*}_{M''M}(\alpha,\beta,\gamma) d\Omega = \frac{8\pi^2}{2J+1} \delta_{M'M''}, \tag{3.30}$$

where $D^J_{M'M}(\alpha,\beta,\gamma)$ are the Wigner rotation functions, (α,β,γ) the Euler angles and $d\Omega = \sin(\beta)d\beta d\alpha d\gamma$, Eq. (3.29) can also be expressed as

$$\left[\frac{\partial^3 P}{\partial q_x \partial q_y \partial q_z}(\vec{q},\phi)\right] = \frac{1}{8\pi^2}\int \left|\int (\Psi^-_{\vec{q}})^* \Psi_{n_{\rm Q}JM'}(t;\Omega,\phi)d\vec{r}\right|^2 d\Omega. \tag{3.31}$$

Here $\Psi_{n_{\rm Q}JM'}(t;\Omega,\phi)$ is a solution to the TDSE corresponding to the rotated initial state $\hat{\mathcal{D}}(\Omega)|n_{\rm Q}JM'\rangle$, with $\hat{\mathcal{D}}$ the rotation operator, in the active view, and $\Omega = (\alpha,\beta,\gamma)$. However, $\Psi_{n_{\rm Q}JM'}(t;\Omega,\phi) = \exp(-i\hat{J}_z\phi)\Psi_{n_{\rm Q}JM'}(t;\Omega',\phi=0)$ with $\Omega' = (\alpha-\phi,\beta,\gamma)$ (see Eq. (3.26)). Thus

$$\left[\frac{\partial^3 P}{\partial q_x \partial q_y \partial q_z}(\vec{q},\phi)\right] = \frac{1}{8\pi^2}\int \left|\int (\Psi^-_{\vec{q}})^* \exp(-i\hat{J}_z\phi)\Psi_{n_{\rm Q}JM'}(t;\Omega',\phi=0)d\vec{r}\right|^2 d\Omega. \tag{3.32}$$

The rotation of a scattering wave function, with asymptotic momentum $\vec{q}$, can be accomplished just by rotating the asymptotic momentum, i.e., $\exp(i\hat{J}_z\phi)\Psi^-_{\vec{q}} = \Psi^-_{\vec{q}'}$, where $\vec{q}' = \mathbf{R}_z(-\phi)\vec{q}$. This means that

$$\begin{aligned}\left[\frac{\partial^3 P}{\partial q_x \partial q_y \partial q_z}(\vec{q},\phi)\right] &= \frac{1}{8\pi^2}\int_0^{2\pi}\int_0^{2\pi}\int_0^{\pi}\sin(\beta)d\beta d\alpha d\gamma \\ &\times \left|\int d\vec{r}\,(\Psi^-_{\vec{q}'})^*\Psi_{n_{\rm Q}JM'}(t;\Omega',\phi=0)\right|^2.\end{aligned} \tag{3.33}$$

Finally this expression can be rewritten as

$$\begin{aligned}\left[\frac{\partial^3 P}{\partial q_x \partial q_y \partial q_z}(\vec{q},\phi)\right] &= \frac{1}{8\pi^2}\int_0^{2\pi}\int_{-\phi}^{2\pi-\phi}\int_0^{\pi}\sin(\beta)d\beta d\alpha d\gamma \\ &\times \left|\int d\vec{r}\,(\Psi^-_{\vec{q}'})^*\Psi_{n_{\rm Q}JM'}(t;\Omega,\phi=0)\right|^2 \\ &= \left[\frac{\partial^3 P}{\partial q_x \partial q_y \partial q_z}(\vec{q'},\phi=0)\right],\end{aligned} \tag{3.34}$$

due to the uniformity of the distribution function over the orientations, $G(\Omega) = 1/(8\pi^2)$. Thus, a change in the CEP from $\phi = 0$ to $\phi = \phi'$ corresponds to a rotation of the ensemble average of the momentum distribution around the z-axis by ϕ'. This is illustrated in Figure 3.5, which shows the ensemble average of the exact momentum distribution, in the xy polarization plane, for Ar atoms initially in an incoherent mixture of $3p_x$ or $3p_y$ states, for two different values of the CEP $\phi = -\pi/2$ and $\phi = 0$. This finishes the treatment of the characterization of the CEP for a circularly polarized laser pulse.

CHAPTER 4

The strong-field approximation

Having presented the *ab-initio* theory, we are now ready to present the strong-field approximation (SFA) which is an approximate method of calculating the response of an atom or molecule by an external electric field [11, 41–43]. The SFA for ionization has its origin in the length gauge Keldysh theory for ionization developed by L. V. Keldysh [11] in 1964, with subsequent contributions from F. H. M. Faisal [41] and H. R. Reiss [42]. Historical, the terminology "SFA" was put forward by H. R. Reiss and refer to the velocity-gauge S-matrix approach described in [42]. However, nowadays this terminology normally refers both to velocity-gauge approaches as well as Keldysh theories, we will follow this trend.

In order to fully account for the ionization of atoms and molecules in strong fields, one has to solve the TDSE. However, this is an extremely difficult task, in fact, only doable for the most simple atoms and molecules. This underlines the need for simple solvable models, like the SFA, providing us with basic physical insight.

4.1 Derivation of the strong-field approximation

Consider an atom or a molecule, initially described by the wave function Ψ_i, interacting with an external time-dependent potential $V(t)$, e.g., $V(t) = \vec{r} \cdot \vec{E}(t)$ in

length gauge or $V(t) = \vec{A}(t) \cdot \vec{\hat{p}} + A^2(t)/2$ in velocity gauge. The TDSE reads

$$i\frac{\partial}{\partial t}\Psi = (\hat{H}_0 + V(t))\Psi, \tag{4.1}$$

where $\hat{H}_0$ is the field-free Hamiltonian. It is easily checked, that a solution to Eq. (4.1) can be written as

$$\Psi(\vec{r}, t) = -i\int_0^t U(t, t')V(t')\Psi_i(\vec{r}, t')dt' + \Psi_i(\vec{r}, t), \tag{4.2}$$

where U is the time-evolution operator for the full Hamiltonian. The last term, Ψ_i, ensures that the solution satisfies the boundary condition $\Psi(\vec{r}, t = 0) = \Psi_i(\vec{r}, t = 0)$, i.e., ensures that the system before the pulse is described by the correct initial wave function. The initial wave function is given by

$$\Psi_i(\vec{r}, t) = \psi_i(\vec{r}) \exp(-iE_i t), \tag{4.3}$$

where ψ_i is a solution to the time-independent Schrödinger equation, $\hat{H}_0\psi_i = E_i\psi_i$, and E_i is the binding energy of the neutral atom or molecule. The calculation of the first term in Eq. (4.2) is just as difficult as solving Eq. (4.1) due to the full time-evolution operator U. However, the form of Eq. (4.2) together with physical intuition actually prompts the SFA. The probability amplitude for ionization, i.e., the transition amplitude for populating the exact continuum state $\Psi_{\vec{q}}$, with asymptotic momentum $\vec{q}$, describing the liberated electron in the combined fields is

$$T_{\vec{q}} = -i\int_0^\tau \langle \Psi_q(t')|V(t')|\Psi_i(t')\rangle dt', \tag{4.4}$$

which motivates the following physical interpretation. The field-free system interacts with the laser field at $t = t'$ and is subsequently propagated in the combined Coulomb and laser fields until we measure the momentum distribution at the end of the pulse [44]. The propagation in the combined fields is presumably dominated by the laser field due to large field strength. If we neglect the Coulomb potentials influence on the liberated electron, i.e., only include the laser field, we arrive at the following expression for the final state

$$\Psi_{\vec{q}}(\vec{r}, t) = \psi^{\mathrm{V}}_{\vec{q}}(\vec{r}, t), \tag{4.5}$$

with $\psi^{\mathrm{V}}_{\vec{q}}$ a Volkov state (Eq. (2.34) and Eq. (2.35)). Thus

$$T^{\mathrm{SFA}}_{\vec{q}} = -i\int_0^\tau \langle \psi^{\mathrm{V}}_{\vec{q}}(t')|V(t')|\psi_i\rangle \exp(iI_p t')dt', \tag{4.6}$$

where I_p denotes the ionization potential for the atom or molecule. Formula (4.6) is the celebrated SFA probability amplitude for strong-field ionization. The above derivation shows that the SFA relies on the following assumptions: (i) The binding potentials influence on the electron in the continuum is negligible. This assumption is legitimate provided that the field-strength is large enough to dominate the Coulomb term at the distances where ionization occurs. While this assumption is justified for zero-range potentials, e.g., negative ions, it is problematic in the case of neutral atoms or molecules due to the long range of the Coulomb potential. This is especially true in the case of a linearly polarized laser pulse [45–47], where the liberated electron is driven back towards the nucleus approximate one fourth of an optical cycle after ionization. (ii) Intermediate resonances do not play a role, only the transition initial $\rightarrow$ Volkov is accounted for within the SFA. This is again in many cases problematic and only strictly legitimate if the field is very strong. Despite of the many flaws and problems regarding the SFA it is often surprisingly successful for producing the basic physical features and many strong-field phenomena can be described qualitatively by the SFA.

Once $T_{\vec{q}}$ is known, it is, in principle, straightforward to calculate, for example, the momentum distribution

$$\frac{\partial^3 P}{\partial q_x \partial q_y \partial q_z} = |T_{\vec{q}}|^2. \tag{4.7}$$

Whether or not it is possible to calculate $T_{\vec{q}}$ in practice, of course, depends on the complexity of the matrix element $\langle \psi_{\vec{q}}^{\mathrm{V}} | V | \psi_i \rangle$ i.e., on the complexity of the initial state.

The SFA amplitude is by no means gauge invariant due to the massive approximations behind the derivation. Hence, the length-gauge SFA (LG-SFA) will in general differ from the velocity-gauge SFA (VG-SFA). As a result, there has in recent years been an ongoing debate on which gauge to use when examining strong-field phenomena such as strong-field ionization. Some authors have argued in favor of LG-SFA [22–24, 48–51] while others have claimed that VG-SFA [52–54] is superior. To make matters worse, the question may also be system dependent. However, in the case of ionization, two arguments speak in favor of LG-SFA. First, length gauge probes the asymptotic part of space, which is the region where the SFA is expected to work best due to the neglect of the binding potential in the final state. Furthermore, the LG-SFA amplitude reduces to the well-known tunneling formula in the limit $\omega \rightarrow 0$, this is not the case for the VG-SFA amplitude [48]. With this in mind, it does not come as a surprise that the majority of theoretical and experimental studies [22–24, 48–51] indicates that LG-SFA is indeed superior

compared to VG-SFA when it comes to describing strong-field ionization. All the SFA calculations shown in this thesis are obtained using the LG-SFA.

We will finish this section by deriving a general analytic expression for the LG-SFA transition amplitude. The transition amplitude is given by

$$T_{\vec{q}}^{\text{LG-SFA}} = -i \int_0^\tau \int \psi_{\vec{q}}^{\text{V}}(\vec{r},t)\vec{r}\cdot\vec{E}\psi_i(\vec{r})\exp(iI_p t)d\vec{r}dt, \tag{4.8}$$

where the length gauge Volkov wave ψ_q^{V} satisfies the differential equation

$$i\frac{\partial\psi_{\vec{q}}^{\text{V}}}{\partial t} = \left(-\frac{\nabla^2}{2} + \vec{r}\cdot\vec{E}\right)\psi_{\vec{q}}^{\text{V}}, \tag{4.9}$$

and consequently

$$\begin{aligned} T_{\vec{q}}^{\text{LG-SFA}} &= -i\int_0^\tau \int \left(\frac{\nabla^2}{2}\psi_{\vec{q}}^{\text{V}*} - i\frac{\partial\psi_{\vec{q}}^{\text{V}*}}{\partial t}\right)\psi_i d\vec{r}\exp(iI_p t)dt \\ &= -i\int_0^\tau \int \left(-\frac{(\vec{q}+\vec{A})^2}{2}\psi_{\vec{q}}^{\text{V}*} - i\frac{\partial\psi_{\vec{q}}^{V*}}{\partial t}\right)\psi_i d\vec{r}\exp(iI_p t)dt. \end{aligned} \tag{4.10}$$

Partial integration on the second term in Eq. (4.10) gives the following expression for the transition amplitude

$$\begin{aligned} T_{\vec{q}}^{\text{LG-SFA}} &= i\int_0^\tau \left(I_p + \frac{(\vec{q}+\vec{A})^2}{2}\right)\exp(iI_p t)\int \psi_{\vec{q}}^{\text{V}*}\psi_i d\vec{r}dt \\ &\quad - \left[\int \psi_{\vec{q}}^{\text{V}*}\psi_i d\vec{r}\exp\left(iI_p t\right)\right]_0^\tau \\ &= T_{\vec{q}}^{\text{LG-SFA,1}} + T_{\vec{q}}^{\text{LG-SFA,2}} \end{aligned} \tag{4.11}$$

Now remembering that

$$\psi_{\vec{q}}^{\text{V}}(\vec{r},t) = \frac{1}{\sqrt{(2\pi)^3}}\exp\left(i(\vec{q}+\vec{A}(t))\cdot\vec{r} - \frac{i}{2}\int_0^t(\vec{q}+\vec{A}(t'))^2dt'\right) \tag{4.12}$$

and $\vec{A}(\tau) = \vec{A}(0) = 0$ leads to the following two formulas

$$T_{\vec{q}}^{\text{LG-SFA,1}} = i\int_0^\tau S'(t)\exp\left(iS(t)\right)\tilde{\psi}_i(\vec{q}+\vec{A}(t))dt, \tag{4.13}$$

$$T_{\vec{q}}^{\text{LG-SFA,2}} = \left(1-\exp\left(iS(\tau)\right)\right)\tilde{\psi}_i(\vec{q}), \tag{4.14}$$

where

$$\tilde{\psi}_i(\vec{q}) = \frac{1}{\sqrt{(2\pi)^3}} \int \exp(-i\vec{q}\cdot\vec{r})\psi_i(\vec{r})d\vec{r} \tag{4.15}$$

is the initial state in momentum space and

$$S(t) = \frac{1}{2}\int_0^t \left(\vec{q} + \vec{A}(t')\right)^2 dt' + I_p t \tag{4.16}$$

denotes the semiclassical action. Ionization predominantly occurs at large distance and hence it is a good approximation to use the asymptotic form of the initial state. The asymptotic initial state is expanded in partial waves and reads

$$\psi_i(\vec{r}) = \sum_{lm} C_{lm} r^{\nu-1} \exp\left(-\kappa r\right) Y_{lm}(\hat{r}), \tag{4.17}$$

with C_{lm} the asymptotic expansion coefficients, $\kappa = \sqrt{2I_p}$ and $\nu = Z/\kappa$, where Z is the charge of the residual ion. It is shown in appendix B, that the Fourier transform of the asymptotic initial state is given by

$$\begin{aligned}\tilde{\psi}_i(\vec{q}) = &\sum_{lm} C_{lm} \left(\frac{q}{i\kappa}\right)^l \frac{\kappa^\nu \Gamma(l+\nu+2)}{2^{l+1/2}\Gamma(l+3/2)(\kappa^2+q^2)^{\nu+1}} \\ &\times_2 F_1\left(\frac{l-\nu}{2}, \frac{l-\nu+1}{2}; l+\frac{3}{2}; -\frac{q^2}{\kappa^2}\right) Y_{lm}(\hat{q}),\end{aligned} \tag{4.18}$$

with ${}_2F_1$ denoting the Gauss hypergeometric series

$${}_2F_1(a,b;c;x) = \sum_{n=0}^{\infty} \frac{(a)_n (b)_n}{(c)_n} \frac{x^n}{n!}. \tag{4.19}$$

Thus

$$\begin{aligned}T_{\vec{q}}^{\text{LG-SFA,1}} = &\sum_{lm} C_{lm} \frac{\kappa^\nu \Gamma(l+\nu+2)}{2^{l+\nu+3/2}\Gamma(l+3/2)} \int_0^\tau \frac{1}{S'(t)^\nu} \left(\frac{Q}{i\kappa}\right)^l Y_{lm}(\hat{Q}) \\ &\times_2 F_1\left(\frac{l-\nu}{2}, \frac{l-\nu+1}{2}; l+\frac{3}{2}; -\frac{Q^2}{\kappa^2}\right) \exp\left(iS(t)\right) dt\end{aligned} \tag{4.20}$$

and

$$\begin{aligned}T_{\vec{q}}^{\text{LG-SFA,2}} = &\sum_{lm} C_{lm} \left(\frac{q}{i\kappa}\right)^l \frac{\kappa^\nu \Gamma(l+\nu+2)}{2^{l+1/2}\Gamma(l+3/2)(\kappa^2+q^2)^{\nu+1}} \\ &\times_2 F_1\left(\frac{l-\nu}{2}, \frac{l-\nu+1}{2}; l+\frac{3}{2}; -\frac{q^2}{\kappa^2}\right) Y_{lm}(\hat{q}) \left(1 - \exp\left(iS(\tau)\right)\right),\end{aligned} \tag{4.21}$$

where $\vec{Q}(t) = \vec{q} + \vec{A}(t)$ is the kinematical momentum. Even though Eq. (4.20) and Eq. (4.21) can be used to calculate the transition amplitude it is often an advantage to invoke the saddle-point method [55, 56] in calculating the time integral in Eq. (4.20), since this speeds up the evaluation and furthermore provides us with a very intuitive and appealing physical picture of the ionization process.

4.1.1 The saddle-point approximation

Our goal is to solve the integral

$$\int_0^\tau \frac{1}{S'(t)^\nu} \left(\frac{Q}{i\kappa}\right)^l Y_{lm}(\hat{Q}) \\ \times_2 F_1\left(\frac{l-\nu}{2}, \frac{l-\nu+1}{2}; l+\frac{3}{2}; -\frac{Q^2}{\kappa^2}\right) \exp\left(iS(t)\right) dt, \tag{4.22}$$

using the saddle-point method [55, 56]. First, we extent the integrand to the upper complex plane, thereby defining a complex function $\mathcal{F}$ on the set $\{t \in \mathbb{C} \,|\mathrm{Im}(t) \geq 0\}$. Regarding the continuation of the spherical harmonics to the complex plane, we note that

$$\left(\frac{Q}{i\kappa}\right)^l Y_{lm}(\hat{Q}) \tag{4.23}$$

is a polynomial of order l in Cartesian coordinates. Accordingly, the continuation to the complex plane does not pose any problem. The function $\mathcal{F}$ is analytic except at the saddle-points for the semiclassical action, $S'(t_s) = 0$, where the function has a singularity, e.g., for a negative ion $\nu = 0$ and $\mathcal{F}$ has a removable singularity at t_s, while $\nu = 1$ for H(1s) and $\mathcal{F}$ has a simple pole at t_s. The equation $S'(t_s) = 0$ has in general $N + 1$ solutions belonging to $\{t \in \mathbb{C} \,|\mathrm{Im}(t) \geq 0, 0 \leq \mathrm{Re}(t) \leq \tau\}$ in the circular case and $2(N+1)$ in the linear case, where N is the number of optical cycles [56]. We will denote the number of saddle-points by N_{SP}, so $N_{\mathrm{SP}} = N+1$ in the circular case and $N_{\mathrm{SP}} = 2(N+1)$ in the linear case. Figure 4.1 shows a typical plot of $|\exp(iS)|$, for $(q_x, q_y, q_z) = (0.8, 0.0, 0.0)$, obtained using the parameters: ellipticity $\pi/2$, peak intensity $I = 1.0 \times 10^{14}$W/cm^2, $\omega = 0.057$ (800 nm), CEP $\phi = 0$, ionization potential $I_p = 0.5$ and number of optical cycles $N = 3$. We observe a rapidly oscillating surface with very deep valleys and high hills. The overall behavior of $|\exp(iS)|$ in Figure 4.1 does not, for fixed ellipticity, depend on the momentum nor on the system parameters and hence the overall behavior shown in Figure 4.1 is actually general. Now consider the path defined by

$$\gamma = C_0 + C_1 + ... + C_{N_{\mathrm{SP}}} - C_\tau, \tag{4.24}$$

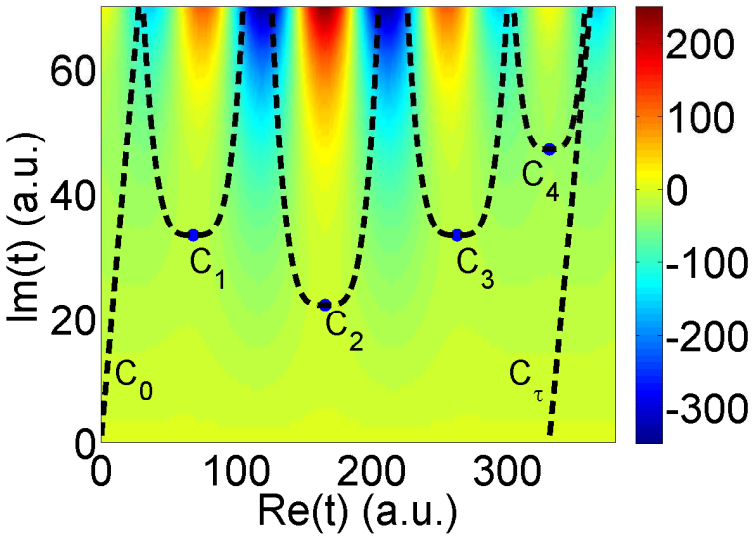

Figure 4.1. *The absolute value of the factor* $\exp(iS)$ *for strong-field ionization of H(1s), with* $(q_x, q_y, q_z) = (0.8, 0.0, 0.0)$*,* $I = 1.0 \times 10^{14}$ *W/cm*^{2}*,* $\omega = 0.057$ *(*800*nm), CEP* $\phi = 0$ *and three optical cycles,* $N = 3$*. The blue points show the position of the saddle-points obtained by solving* $S' = 0$*, while the dotted curve shows a sketch of* γ*. The color scale is logarithmic.*

where C_0 (C_τ) is the steepest descent from 0 (τ) towards $a + i\infty$ ($b + i\infty$) and C_s describes the steepest descent from the saddle-point t_s (see Figure 4.1). Notice, that the paths are patched together at infinity where the term $\exp(iS)$ completely kills the integrand. According to Cauchy's theorem [18]

$$\int_0^\tau \mathcal{F}(t)dt = \int_{C_0} \mathcal{F}(t)dt - \int_{C_\tau} \mathcal{F}(t)dt + \sum_{s=1}^{N_{\text{SP}}} \int_{C_s - i\epsilon} \mathcal{F}(t)dt, \tag{4.25}$$

where $C_1 ... C_{N_{\text{SP}}}$ have been modified slightly ($\epsilon \to 0^+$) such that they avoid the singularities from below in order to fulfill the prerequisite for Cauchy's theorem. The main contribution to the integral $\int_{C_0}$ ($\int_{C_\tau}$) comes from the point $t = 0$ ($t = \tau$) and a careful investigation shows that $\int_{C_0} - \int_{C_\tau}$ cancels the term $T_{\vec{q}}^{\text{LG-SFA,2}}$ [55, 56]. Thus

$$T_{\vec{q}}^{\text{LG-SFA}} = \sum_{lm} C_{lm} \frac{\kappa^\nu \Gamma(l + \nu + 2)}{2^{l+\nu+3/2}\Gamma(l + 3/2)} \sum_{s=1}^{N_{\text{SP}}} \int_{C_s - i\epsilon} \mathcal{F}(t)dt. \tag{4.26}$$

Figure 4.1 clearly illustrates that the main contribution to each of the integrals $\int_{C_{s\in\{1\dots N_{\mathrm{SP}}\}}}$ comes from the part close to the saddle-point t_s. Assuming that the spherical harmonic together with the Gauss hypergeometric series does not change substantially near $t = t_s$, compared to $\exp(iS)/(S')^\nu$, and hence can be regarded as a constant

$$\int_{C_s-i\epsilon} \mathcal{F}(t)dt = {}_2F_1\left(\frac{l-\nu}{2}, \frac{l-\nu+1}{2}; l+\frac{3}{2}; 1\right)\left(\frac{Q(t_s)}{i\kappa}\right)^l Y_{lm}(\hat{Q}(t_s)) \times \int_{C_s-i\epsilon} \frac{1}{(S'(t))^\nu}\exp\left(iS(t)\right)dt. \tag{4.27}$$

Finally expanding S to second order around the saddle-point yields the final expression for the integral (see appendix C)

$$\int_{C_s-i\epsilon} \frac{1}{(S'(t))^\nu}\exp\left(iS(t)\right)dt \approx i^\nu \frac{\Gamma(\nu/2)}{2\Gamma(\nu)}\sqrt{\frac{2\pi i}{S''(t_s)}}\left(-2iS''(t_s)\right)^{\nu/2}\frac{\exp(iS(t_s))}{(S''(t_s))^\nu} \tag{4.28}$$

and hence

$$T_{\vec{q}}^{\text{LG-SFA}} \approx \sum_{lm} i^\nu C_{lm}\frac{\kappa^\nu\Gamma(l+\nu+2)\Gamma(\nu/2)}{2^{l+\nu+5/2}\Gamma(l+3/2)\Gamma(\nu)}\,{}_2F_1\left(\frac{l-\nu}{2}, \frac{l-\nu+1}{2}; l+\frac{3}{2}; 1\right) \times \sum_{t_s}\left(\frac{Q(t_s)}{i\kappa}\right)^l Y_{lm}(\hat{Q}(t_s))\sqrt{\frac{2\pi i}{S''(t_s)}}(-2iS''(t_s))^{\nu/2}\frac{\exp(iS(t_s))}{(S''(t_s))^\nu} \tag{4.29}$$

The Gauss hypergeometric series can be calculated using the relation [18]

$${}_2F_1(a,b;c;1) = \frac{\Gamma(c)\Gamma(c-a-b)}{\Gamma(c-a)\Gamma(c-b)} \qquad c > \max(0, a+b). \tag{4.30}$$

For each momentum the saddle-point equation is solved giving a sequence of complex numbers $\{t_s\}$ which together with Eq. (4.29) allows us to calculate the transition amplitude. The most time-consuming part of this procedure is the solution of the saddle-point equation. While the saddle-points are analytically known in the case of a linearly polarized monochromatic field, they can, in general, only be found by solving the saddle-point equation $S'(t_s) = 0$ numerically, using, for instance, the Newton-Raphson method for nonlinear systems of equations [57]. We use an iterative method. The transition amplitude is calculated on a three-dimensional equidistant momentum grid, where the saddle-points for a given momentum is found using the Newton-Raphson method with the saddle-points from the previous momentum used as initial guesses.

The saddle-point method yields, if applicable, a quick and very intuitive way of calculating the LG-SFA transition amplitude for ionization. Whether or not the saddle-point method is valid depends highly on the field and system parameters such as field strength, pulse duration and ionization potential. We will return to this topic in chapter 5, where the validity of the saddle-point approximation is examined.

Now what about the saddle-points, are they just mathematical objects or is it possible to extract some physics from them and from the saddle-point method in general [56]. It turns out, that this question is closely connected to the following semiclassical model [58]. This very simple model describes ionization as a two-step process. First, the electron is born, via tunneling, in the continuum at time $t = t_0$, with initial velocity ($\vec{v}_0 = 0$) zero. Second, it moves as a classical particle in an electric field. The dynamics is govern by Newton's second law

$$\frac{d\vec{q}}{dt} = -\vec{E} - \nabla V, \tag{4.31}$$

where V is the binding potential. Neglecting the binding potential, once the electron is liberated, leads to the following expression for the momentum

$$\begin{aligned} \vec{q} &= -\int_{t_0}^{\infty} \vec{E} dt \\ &= -\vec{A}(t_0), \end{aligned} \tag{4.32}$$

providing us with a mapping from ionization time to final momentum. Even though the model describes ionization of a tunneling process, and we therefore expect the model to perform best in the tunneling regime, the applicability, at least from a qualitatively point of view, is not restricted to the tunneling regime. The model is restricted to the polarization plane (axis in the linear case), since $\vec{v}_0$ is fixed to zero. However, off-axis emission can be accounted for by replacing the ansatz $\vec{v}_0 = 0$ by a Gaussian distribution of initial velocities peaking at zero.
In the limit $I_p \to 0$, the saddle-point equation $S' = 0$ reduces to Eq. (4.32). In the general case this is no longer true, however, $-\mathrm{Re}(\vec{A}(t_s))$ still approximately points in the direction of $\vec{q}$ [56, 59]. Motivated by this, we interpret t_s as a ionization time, where the non-zero imaginary part is a consequence of the binding potential $I_p \neq 0$. Ionization is a classically forbidden process, except in the over-the-barrier regime, accordingly ionization occur via a quantum mechanical process, like tunneling, and the imaginary part of t_s is a consequence of this. Next, building on this interpretation of the saddle-points, we can make the following very appealing interpretation of the saddle-point method. The SFA probability amplitude can be

written as a Feynman path integral

$$T_{\vec{q}}^{\text{LG-SFA}} = \int D \exp(iS(t)), \tag{4.33}$$

where we integrate over all possible paths leading to ionization, with asymptotic momentum $\vec{q}$, and where D denotes the non-exponential part of the integrand and the measure of integration. If ionization is dominated by a few paths, this integral reduces to a finite sum over the relevant paths. Accordingly, the saddle-point method, at least in some sense, can be viewed as a way of finding these contributions [60]

$$T_{\vec{q}}^{\text{LG-SFA}} \approx \sum_{t_s} a(t_s) \exp(iS(t_s)). \tag{4.34}$$

The saddle-point method is very popular due to the features described in the previous discussion and it has been used to describe a variety of different physical process, for instance, above-threshold ionization and high-order above threshold ionization [56].

CHAPTER 5

Strong-field ionization of atoms by few-cycle circularly polarized laser pulses

The chapter is devoted to a detailed investigation of strong-field ionization of atoms by few-cycle laser pulses, in particular circularly polarized laser pulses. We will start out with a detailed comparison between the *ab-initio* theory described in chapter 3 and the LG-SFA introduced in chapter 4. This allows us to identify and explain striking effects of the Coulomb potential in the photoelectron momentum distribution, in particular counterintuitive angular shifts similar to the shifts observed in the recent experiment by Eckle *et.al* [61] on the ionization of Helium. We show that the shift is a consequence of the combined effect of the laser field and the Coulomb potential, hereby providing an alternative explanation to the one given in [61], based on the concept of tunneling time. Having established, in chapter 2, how the ionization process depends on the CEP it seems natural to investigate how ionization depends on the number of cycles. Thus, we proceed to an investigation of the ionization process, using the LG-SFA, with emphasis on finite bandwidth effects. Furthermore, we investigate the validity of the saddle-point method for evaluating the LG-SFA transition amplitude (SPM LG-SFA). The SPM LG-SFA is a popular tool for studying strong-field phenomena and it is therefore important to know how the validity of the SPM LG-SFA depends on different pulse parameters

such as ellipticity, pulse length and peak intensity.

Almost all the results presented in this chapter are on atomic hydrogen, which at first glance might seem as a serious limitation. However, the effects studied in this chapter are not related to a particular atomic system. The angular shifts, for instance, are related to a combined effect of the laser field and the Coulomb potential and is expected to occur for a wide range of different atomic species. The consideration of H as our test system is for computational convenience and actually not a restriction when it comes to an identification of the generic physics investigated here.

5.1 TDSE calculations versus SFA calculations: Imprints of the Coulomb potential on the photoelectron momentum distribution

We consider H(1s) interacting with an electric field, $\vec{E}(t) = -\partial_t \vec{A}(t)$, defined via the vector potential[1]

$$\vec{A}(t) = A_0 f(t) \begin{pmatrix} \cos(\omega t + \phi)\cos\left(\frac{\epsilon}{2}\right) \\ \sin(\omega t + \phi)\sin\left(\frac{\epsilon}{2}\right) \\ 0 \end{pmatrix}, \tag{5.1}$$

where the envelope f is given by

$$f(t) = \begin{cases} \sin^2\left(\frac{\omega t}{2N}\right) & t \in [0, \tau] \\ 0 & \text{elsewhere.} \end{cases}$$

Here A_0 is the amplitude, τ is the pulse length, ω is the carrier frequency, N the number of optical cycles, $\epsilon \in [0; \frac{\pi}{2}]$ the ellipticity and ϕ the CEP. The full dynamics of the system is govern by the TDSE, which we solve using the methods described in chapter 3. We solve the velocity gauge TDSE using a grid-based split-step method, where the wave function is expressed in a basis of spherical harmonics

$$\Psi(\vec{r}, t) = \sum_{lm} \frac{f_{lm}(r, t)}{r} Y_{lm}(\theta, \varphi), \tag{5.2}$$

and the initial state $\Psi(\vec{r}, 0)$ is obtained by propagation in imaginary time. Having obtained the final wave function, we can easily calculate the differential momentum

[1] Just to remind ourselves

distribution by projecting the wave packet after the pulse onto Coulomb continuum scattering eigenstates of asymptotic momentum $\vec{q}$

$$\Psi_{\vec{q}}^{C,-}(\vec{r}) = \exp(-\pi\gamma/2)\Gamma(1-i\gamma)\exp(i\vec{q}\cdot\vec{r})_1F_1(i\gamma;1;-i(qr+\vec{q}\cdot\vec{r})) \quad (5.3)$$

$$\frac{\partial^3 P}{\partial q_x \partial q_y \partial q_z} = |\langle \Psi_{\vec{q}}^{C,-}|\Psi(\vec{r},T)\rangle|^2. \quad (5.4)$$

Here γ is the Sommerfeld parameter and ${}_1F_1$ denotes the confluent hypergeometric function

$${}_1F_1(a;c;x) = \sum_{n=0}^{\infty} \frac{(a)_n}{(c)_n}\frac{x^n}{n!}. \quad (5.5)$$

For comparison, LG-SFA provides us with the following simpler formula for the differential momentum distribution[2]

$$\frac{\partial^3 P}{\partial q_x \partial q_y \partial q_z} = \left| \int_0^{\tau} \langle \psi_{\vec{q}}^{\mathrm{V}}(t)|\vec{r}\cdot\vec{E}(t)|\psi_i(t)\rangle dt \right|^2, \quad (5.6)$$

where $\Psi_{\vec{q}}^{\mathrm{V}}(t)$ denotes a Volkov wave function in length gauge and $\psi_i(t)$ the initial state.

Figure 5.1(a) and Figure 5.1(b) present calculated momentum distributions evaluated in the plane of circular polarization, $\partial^3 P/\partial q_x \partial q_y \partial q_z|_{q_z=0}$, for H(1s), obtained by solving the TDSE, for 800 nm, peak intensities[3] $5\times10^{13}\,\mathrm{W/cm^2}$ and $1.0\times10^{14}\,\mathrm{W/cm^2}$, ellipticity $\epsilon=\pi/2$, CEP $\phi=-\pi/2$ and 3 optical cycles. In order to obtain convergence, we used a radial grid consisting of 4096 points extending to 300, a time-step $\Delta t = 0.01$ and maximum angular momentum $l_{\max}=25$ for $5\times10^{13}\,\mathrm{W/cm^2}$ and $l_{\max}=35$ for $10^{14}\,\mathrm{W/cm^2}$. For better graphical display, we have removed the low energy part $\sqrt{q_x^2+q_y^2}<0.1$. Figure 5.1(e) and Figure 5.1(f) present distributions obtained using the LG-SFA, i.e., using Eq. (5.6) where the spatial integral is solved analytically[4] and the time integral is solved using Gauss-Legendre quadrature [57].

Our LG-SFA results follow the shape of the vector potential (curvy lines in Figure 5.1). This can easily be explained by the semiclassical model introduced in chapter 4. Due to the, exponential for a tunneling process, dependence of the rate on the field strength, the ionization rate is symmetric with respect to reflection in the symmetry axis of the electric field, with ionization predominantly occurring close to field maximum, i.e., when the instant of ionization is close to $t=\tau/2$.

[2] Chapter 4

[3] For hydrogen, $1.4\times10^{14}\,\mathrm{W/cm^2}$ is the critical intensity for over-the-barrier ionization

[4] Chapter 4

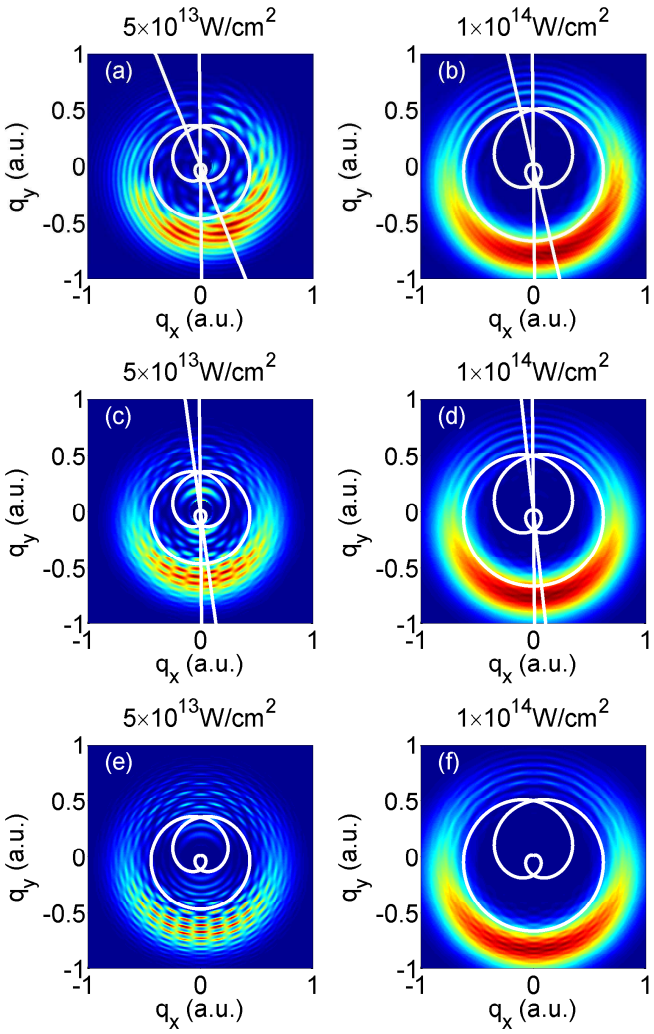

Figure 5.1. *Momentum distributions evaluated in the plane of polarization, $\partial^3 P/\partial q_x \partial q_y \partial q_z|_{q_z=0}$, for strong-field ionization of H(1s). Panels (a) and (b) show results obtained by solving the TDSE, (c) and (d) show results obtained using the Coulomb-Volkov corrected LG-SFA, while (e) and (f) show results obtained using the LG-SFA. The curves shows $-\vec{A}(t)$, while the straight lines in (a), (b), (c) and (d) highlight the angular shift (see text). The field parameters are $\omega = 0.057$ (800nm), $\epsilon = \pi/2$, $\phi = -\pi/2$, $I = 5\times10^{13}\,W/cm^2$ ((a), (c), (e)), $I = 10^{14}\,W/cm^2$ ((b), (d), (f)) and 3 optical cycles.*

Hence, the dominant direction of electron ejection is determined by $\vec{q}_f = -\vec{A}(\tau/2)$ and the momentum distributions are symmetric with respect to reflection in the symmetry axis of the vector potential. It can be checked that the ADK tunneling theory predicts similar behavior [62]. Note that, this conclusion only holds in the case of a symmetric initial state. In the general case, the shape of the initial orbital has to be taken into account. We will return to this point in chapter 6, where we study the ionization of oriented targets, e.g., ionization of Argon initially in a $3p_x$ or $3p_y$ state.

Comparison with the TDSE results show two important features not captured by the LG-SFA: (i) A spiral structure equivalent to the radial-fans observed in the linear case (see [63–67] and references therein). The presence of these structures is intimately connected to the interaction of the outgoing low-energy electrons with the long-range Coulomb part of the potential. (ii) Second, we observe counterintuitive angular shifts of the dominant direction of electron ejection. The dominant direction of electron ejection of the TDSE momentum distributions does not coincide with the symmetry axis of the vector potential, the former being shifted by a small angle, eg., $\sim 23^\circ$ for 5.0×10^{13}W/cm^2 and $\sim 12^\circ$ for 1.0×10^{14}W/cm^2. Notice that similar shifts are also seen on Figure 3.5 in chapter 3. The observed shift is seen to decrease as a function of intensity in good agreement with the fact that the validity of the LG-SFA is expected to improve with increasing intensity, as long as we do not reach the regime of saturation. Furthermore, TDSE calculations (not shown) show that the shifts disappear, as expected, in the long pulse limit, $N \to \infty$, where the electric field and consequently the momentum distribution becomes symmetric (see section 5.2).

Similar shifts was recently observed experimentally for the ionization of Helium by a near circularly polarized few-cycle pulse and explained using a Coulomb-modified ADK tunneling model in addition to a possible very small tunneling time [61]. In the following we present a more basic quantum mechanical explanation without reference to a tunneling time. The shifts are a consequence of a subtle interplay between the laser field and the atomic potential.

We note that in the many-cycles regime, where there is no effect of the carrier-envelope phase (CEP) and therefore no control over directionality in the ionization dynamics, similar loss of symmetry was studied extensively for elliptically polarized pulses interacting with atoms [68, 69] and several models were put forward [69–72] all including the effect of the Coulomb potential on the liberated electron.

In the case of a few-cycle linearly polarized pulse several studies have shown the importance of including the Coulomb potential in order to properly describe

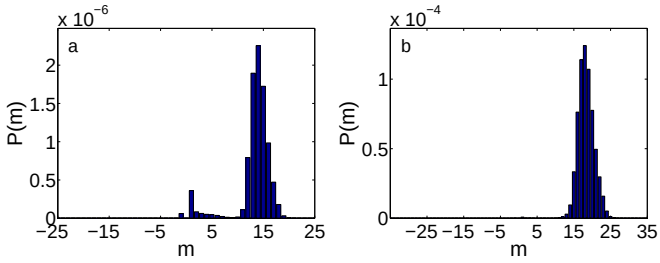

Figure 5.2. *The probability $P(m)$ for a specific magnetic quantum number m after the pulse: (a) for $I = 5 \times 10^{13} W/cm^2$, (b) for $I = 10^{14} W/cm^2$. The other field parameters are $\omega = 0.057$ (800nm), $\epsilon = \pi/2$, CEP $\phi = -\pi/2$ and $N = 3$.*

the ionization of atoms [45–47] and molecules [16, 73].

The shift is a manifestation of the fact that $\langle\Psi|\hat{L}_z|\Psi\rangle = \langle\hat{L}_z\rangle \neq 0$ after the pulse. Consequently the azimuthal velocity is non-vanishing which, in turn, makes the distribution rotate compared to the $\langle\hat{L}_z\rangle = 0$ case. This is a crucial point which will be elaborated in the following. The hydrogen atom is initially in the 1s ground state and hence $\langle\hat{L}_z\rangle = 0$ before the pulse. According to Ehrenfest's theorem

$$\frac{d}{dt}\langle\hat{L}_z\rangle = i\langle[\hat{H}, \hat{L}_z]\rangle, \tag{5.7}$$

which forces the liberated electron to pick up a nonzero value of $\langle\hat{L}_z\rangle$, since $[\hat{H}, \hat{L}_z] = i(\hat{p}_x A_y - A_x \hat{p}_y) \neq 0$ during the pulse for $\hat{H} = \hat{H}_0 + \vec{A}\cdot\vec{\hat{p}} + \vec{A}^2/2$, with $\hat{H}_0$ the field-free Hamiltonian. The mean value of $\hat{L}_z$ changes during the pulse, in accordance with Ehrenfest's theorem, until it becomes constant with the value

$$\langle\hat{L}_z\rangle = i\int_0^\tau \langle[\hat{H}, \hat{L}_z]\rangle dt, \tag{5.8}$$

after the pulse. Figure 5.2 shows the probability $P(m)$ for a specific magnetic quantum number m after the pulse, obtained using

$$P(m) = \sum_{l\geq|m|}\int_0^\infty |f_{lm}(r,T)|^2 dr. \tag{5.9}$$

We have removed the $m = 0$ component in order to focus on the ionized part of the wave packet. We see that $P(m)$ peaks around $m \cong 14$ for $5 \times 10^{13}\mathrm{W/cm^2}$ and shifts towards $m \cong 18$ for $1.0\times10^{14}\mathrm{W/cm^2}$. By studying the (l, m)-decomposition of the above-threshold-ionization spectrum, we have checked that these peaks indeed comes from the ionized part of the wave packet. The pulse mainly populates

states with $m \geq 0$, since the laser field is left-handed. The main point is that the mean value of $\hat{L}_z$ is different from zero, since $\langle \hat{L}_z \rangle = \sum_m mP(m)$. The behavior, described above, is in complete contrast with the behavior described by the LG-SFA. It is easily shown that in this case, even though the commutator $[\hat{H}, \hat{L}_z]$ is different from zero, the expectation in the Volkov continuum is zero, $\langle [\hat{H}, \hat{L}_z] \rangle = 0$, implying $\langle \hat{L}_z \rangle = 0$. Hence, $\langle \hat{L}_z \rangle$ is identically zero at all times within the LG-SFA. This explains why the exact distributions are shifted counterclockwise compared to the LG-SFA distributions. Notice, that the shift is a combined effect of the laser field and the Coulomb potential, the laser field alone does not induce any shift as explained above. However, the laser field ensures that $[\hat{H}, \hat{L}_z]$ is different from zero while the state evolved in the presence of both the field and the Coulomb potential ensures that $\langle [\hat{H}, \hat{L}_z] \rangle$ is different from zero. Thus, it is a truly combined effect which cannot be described by theories like ADK or the standard LG-SFA.

The discussion above illustrates a general problem with the standard LG-SFA: The mean value of $\hat{L}_z$ is always zero regardless of the parameters. For the interaction between an atom, initially in an s state, and a linearly polarized laser pulse this does not represent a limitation, but it is a critical problem for an elliptically polarized pulse interacting with an atom. In order to address the problem one has to include the Coulomb potential in the LG-SFA, either by going to higher order in the S-matrix formulation [74], or by putting in the Coulomb potential otherwise [47, 69, 71, 72, 75]. One approach is to replace the Volkov wave function by a Coulomb-Volkov wave function [47, 71, 75]

$$\psi_{\vec{q}}^{\mathrm{CV}}(\vec{r}, t) = N(\vec{r}, \vec{q}) \psi_{\vec{q}}^{\mathrm{V}}(\vec{r}, t), \tag{5.10}$$

where

$$N(\vec{r}, \vec{q}) = \exp(-\pi\gamma/2)\Gamma(1 - i\gamma)_1 F_1(i\gamma; 1; -iqr - i\vec{q} \cdot \vec{r}), \tag{5.11}$$

is a correction to the Volkov wave function taking the Coulomb potential into consideration. The Coulomb-Volkov wave function can be thought of as a kind of interpolation between a Volkov wave function and a Coulomb continuum scattering eigenstate. The matrix element in Eq. (5.6) is still analytical, using Nordsieck integrals [76], and the time-integral can be evaluated numerically using Gauss-Legendre quadrature. Figure 5.1(c) and Figure 5.1(d) present distributions obtained using this approach. The Coulomb-Volkov ansatz clearly improves the performance of the LG-SFA but it does not reproduce that angular shifts. The distributions are seen to be shifted slightly compared to the distributions obtained using the standard LG-SFA, but not nearly as much as the exact distributions, since the dynamics in the combined potentials is not fully accounted for.

The size of the shift can be estimated using the following argument. Consider a classical particle with radial velocity v_r and azimuthal velocity v_φ. It follows from the definition of L_z that $d\varphi/dt = L_z/r^2$ which, with reference to Ehrenfest's theorem, translates into $\frac{d}{dt}\langle\varphi\rangle = \left\langle \frac{\hat{L}_z}{r^2} \right\rangle$ in quantum mechanics. Consequently,

$$\Delta\langle\varphi\rangle = \int_{t_0}^{\infty} \left\langle \frac{\hat{L}_z}{r^2} \right\rangle dt \tag{5.12}$$

is the shift in φ obtained after ionization at time t_0, i.e., the shift in angle during the particles way towards the detector. In general $\Delta\langle\varphi\rangle \neq 0$, but the integral is zero regardless of t for the Volkov continuum and thus $\Delta\langle\varphi\rangle = 0$ in the LG-SFA. A very crude estimate of the integral from the end of the pulse τ to ∞ is given by the following

$$\begin{aligned}\int_{\tau}^{\infty} \left\langle \frac{\hat{L}_z}{r^2} \right\rangle dt &\sim \langle \hat{L}_z \rangle_{t=\infty} \left\langle \frac{1}{v_r} \right\rangle_{t=\infty} \int_{r(\tau)}^{\infty} \frac{1}{r^2} dr \\ &\sim \frac{\langle \hat{L}_z \rangle_{t=\infty}}{\langle r \rangle(\tau)} \left\langle \frac{1}{v_r} \right\rangle_{t=\infty},\end{aligned} \tag{5.13}$$

which gives $\sim 14^\circ$ for $5 \times 10^{13}\,\mathrm{W/cm^2}$ and $\sim 11^\circ$ for $10^{14}\,\mathrm{W/cm^2}$, following the trend in the actual shifts ($\sim 23^\circ$ for $5 \times 10^{13}\,\mathrm{W/cm^2}$ and $\sim 12^\circ$ for $10^{14}\,\mathrm{W/cm^2}$) shown in Figure 5.1.

Even though the Keldysh parameter γ [11] only has a well-defined meaning in the long-pulse limit, we note that $10^{14}\,\mathrm{W/cm^2}$ corresponds to $\gamma \approx 1.5$, comparable to the experimental value $\gamma \approx 1.45$ [61]. Our $5 \times 10^{13}\,\mathrm{W/cm^2}$ calculation corresponds to $\gamma \approx 2.1$ and hence the shift also occur at intensities corresponding to the multiphoton regime. Hence, the counterintuitive shifts occur across a wide range of laser intensities, in the few-cycle regime, and can be rationalized without reference to a tunneling time, contrary to the hypothesis in [61].

We proceed to a more qualitative investigation of the momentum distributions, using the LG-SFA, with emphasis on finite bandwidth effects.

5.2 LG-SFA description of the ionization process

Figure 5.3 presents the calculated (q_x, q_y) momentum distribution

$$\frac{\partial^2 P}{\partial q_x \partial q_y}(q_x, q_y) = \int_{-\infty}^{\infty} |T_{\vec{q}}^{\text{LG-SFA}}|^2 dq_z, \tag{5.14}$$

for different numbers of optical cycles N, with intensity $I = 5.0 \times 10^{13}\,\mathrm{W/cm^2}$, frequency $\omega = 0.057$ (800 nm) and CEP $\phi = \pi/2$. The integral in Eq. (5.6) is

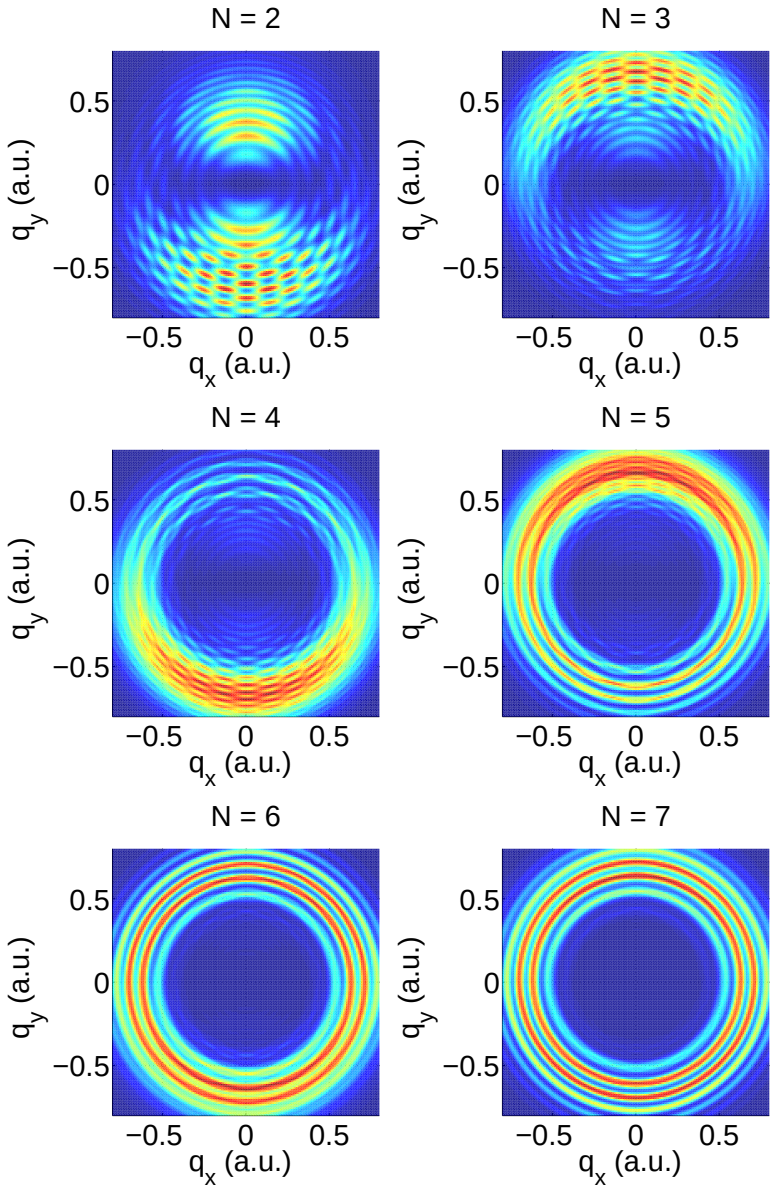

Figure 5.3. *LG-SFA* (q_x, q_y) *momentum distribution for strong-field ionization of H(1s) for various values of optical cycles* N*, with peak intensity* $I = 5.0 \times 10^{13}$ *W/cm*^{2}*, frequency* $\omega = 0.057$ *(800 nm) and CEP* $\phi = \pi/2$*. The grid size is* $\Delta q_x = \Delta q_y = 0.01$*.*

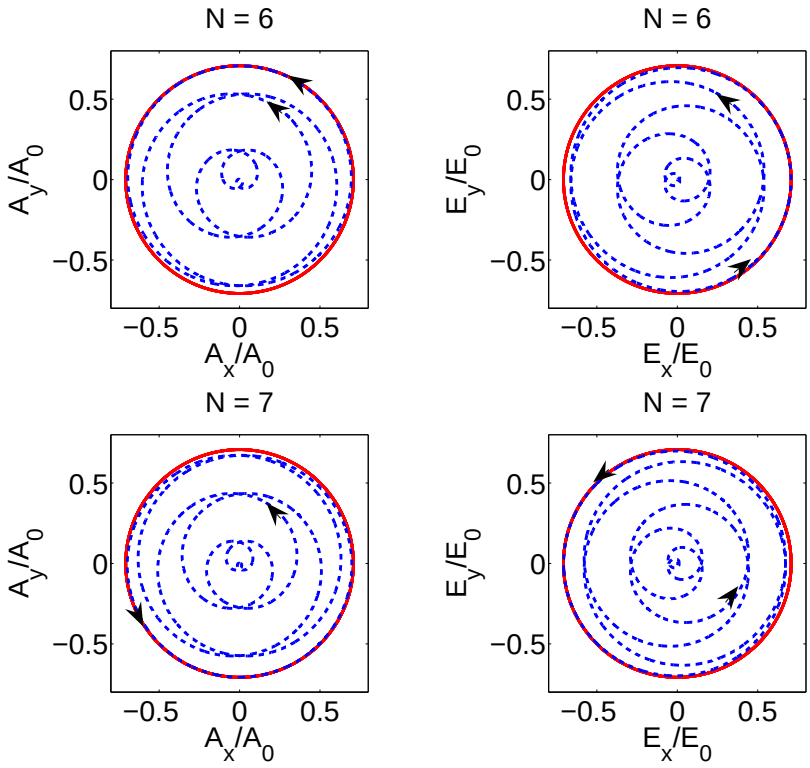

Figure 5.4. *Vector potential and electric field (blue dotted line) for 2 different values of N. The solid curve shows the carrier wave, i.e., the field without the envelope. The arrows show the natural time evolution for the pulse. The parameters are $I = 5.0 \times 10^{13}$ W/cm^2, $\omega = 0.057$ (800 nm) and $\phi = \pi/2$.*

calculated using Gauss-Legendre quadrature [57], while the integral over q_z is calculated using an equidistant grid on $[-Q_z, Q_z]$, where Q_z is chosen large enough to ensure convergence, $Q_z = 0.6$ in the present case. For $N \lesssim 5$ we observe (i) a substantial asymmetry in the direction of electron ejection, reflecting the shape of the vector potential as explained in the previous section, and (ii) a complicated interference pattern radially as well as angularly. The energy difference between two adjacent peaks is not a multiple of the laser frequency and hence the peaks do not correspond to ATI peaks. Notice, that equivalent interference is seen in the TDSE calculations (Figure 5.1). As the number of optical cycles increases we observe a gradual change to a symmetric distribution with well-resolved ATI peaks. The fact that the asymmetry disappears may again be understood classically. For example for $N = 6$ and $N = 7$ the field takes almost a full revolution on the circle,

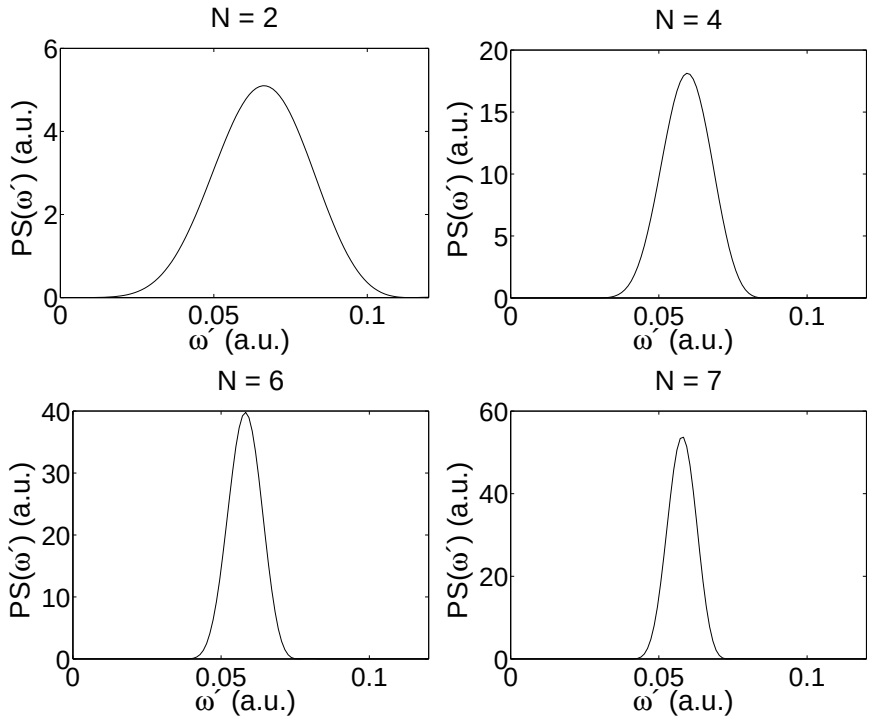

Figure 5.5. *Power spectrum* $|\int_{-\infty}^{\infty} E_x(t)e^{i\omega' t}dt|^2 + |\int_{-\infty}^{\infty} E_y(t)e^{i\omega' t}dt|^2$ *of the electric field for 4 different values of* N*. The parameters are* $\omega = 0.057$ *(800 nm), peak intensity* $I = 5.0 \times 10^{13}$ *W/cm*^{2} *and* $\phi = \pi/2$*.*

corresponding to a monochromatic field with our field strength (see Figure 5.4), and a preferred instant of ionization t_0 cannot be clearly defined. There is almost an entire period around $\frac{\tau}{2}$ where the electron is equally likely to emerge into the continuum, leading to an angularly symmetric distribution in agreement with Figure 5.3. Thus, the overall structure, disregarding the interference for small N, is simply just a signature of the shape of the vector potential.

5.2.1 Interference structures

The behavior of the interference features in Figure 5.3 for $N \lesssim 5$ can be understood by looking at the power spectrum of the pulse. Figure 5.5 shows the power spectrum for four different values of N. The spectrum is very broad for $N = 2$ and $N = 4$ with a lot of frequencies contributing with comparable magnitude. As a consequence there is a large number of different paths leading to the same final

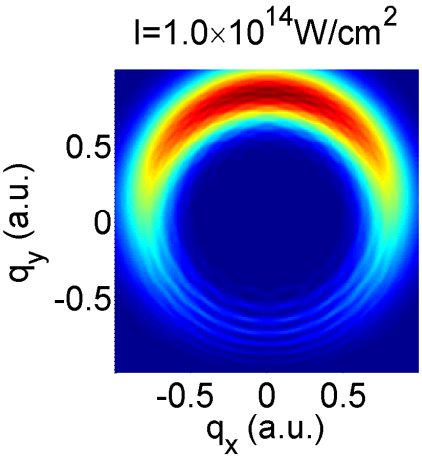

Figure 5.6. *LG-SFA (q_x, q_y) momentum distribution for strong-field ionization of H(1s), with ellipticity $\epsilon = \pi/2$, peak intensity 1.0×10^{14} W/cm^2, $\omega = 0.057$ (800 nm), $N = 3$ and $\phi = \pi/2$.The grid size is $\Delta q_x = \Delta q_y = 0.01$.*

energy and such paths can interfere with each other. We see from Figure 5.5 that the width of the spectrum for $N = 2$ is $\Delta\omega' \sim 0.05$, corresponding to $\Delta E \sim 0.05$. For a momentum of $q = 0.67$ this corresponds to a huge shift in momentum of $\Delta q \sim 0.07$ which is clearly visible with our grid discretization. This explains the observed interference pattern in Figure 5.3. The structure is simply caused by the fact that our pulse contains a very large number of frequencies when N is small, i.e., when the pulse duration is small. As N increases the width of the spectrum gets smaller and frequencies close to ω dominate completely. Thus, we regain the photon picture. For $N = 7$ we have $\Delta\omega' < 0.01$ which corresponds to $\Delta q < 0.015$ for $q = 0.67$. This explains why the interference pattern disappears and why we observe well-resolved ATI-peaks as N increases.

The spectrum of the pulse depends on the form of the envelope. It is therefore interesting to examine if we obtain the same effects with a different envelope. We have calculated the momentum distribution using a Gaussian envelope

$$f(t) = \exp(-(t - \tau/2)^2/\tau_p^2), \tag{5.15}$$

with $\tau_p = 2\arccos(2^{-\frac{1}{4}})\tau/\pi$ [33], and confirmed the interference effects reported above (not shown). The width of the spectrum for a pulse with a Gaussian envelope is a bit smaller for a given value of N, which leads to relatively small changes.

Now what happens if we increase the peak intensity. Figure 5.6 presents the calculated momentum distribution for a three-cycle pulse with frequency $\omega =$

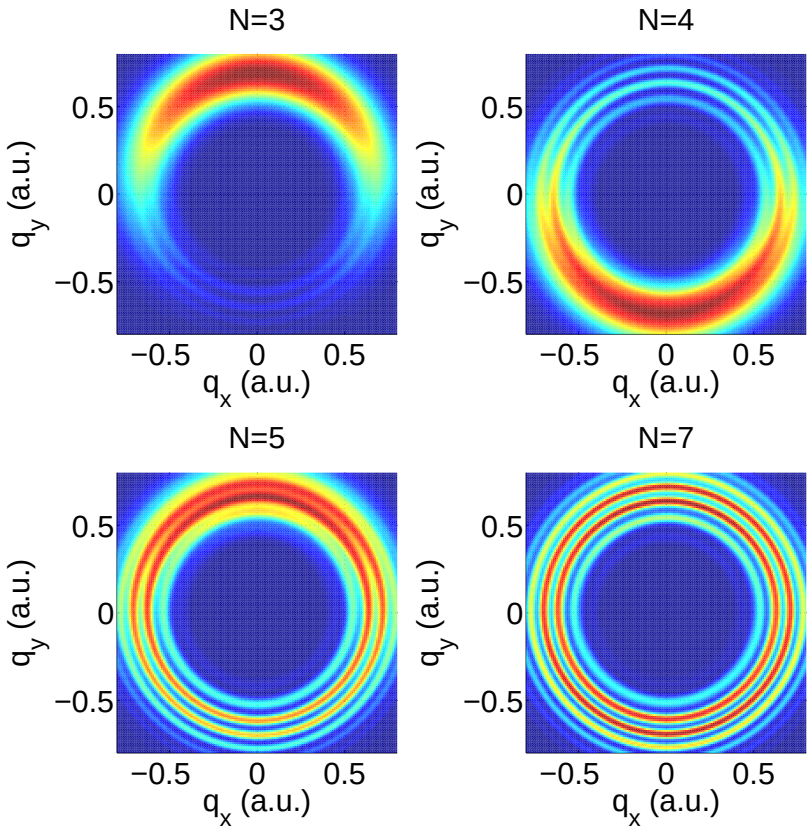

Figure 5.7. *SPM LG-SFA* (q_x, q_y) *momentum distribution of H(1s) for various values of* N*, with* $I = 5.0 \times 10^{13}$ *W/cm*^{2}*,* $\omega = 0.057$ *(800 nm) and* $\phi = \pi/2$*. The grid size is* $\Delta q_x = \Delta q_y = 0.01$*.*

0.057 (800 nm), CEP $\phi = \pi/2$ and peak intensity $I = 1.0 \times 10^{14}\mathrm{W/cm}^2$. We clearly see that the complicated interference structure observed in Figure 5.3 is diminished when the peak intensity is increased to $I = 1.0 \times 10^{14}\mathrm{W/cm}^2$. This behavior can be explained by remembering that the Keldysh parameter falls of as a function of intensity. For $I = 5.0 \times 10^{13}\mathrm{W/cm}^2$, $\gamma = 2.1$ while $\gamma = 1.5$ in the case of $I = 1.0 \times 10^{14}\mathrm{W/cm}^2$. Accordingly, the latter case is closer to the tunneling regime, where we would expect a smooth distribution without any interference structure.

An alternatively interpretation of the interference structure is based on time interference. Wave packets ionized at different instant of time can interfere, due to wave packet spreading, and lead to interference structures in the momentum

distribution. Having the interpretation of the SPM LG-SFA in mind this method seems like the obvious tool for studying such interference. The result of a SPM LG-SFA calculation for four different values of N, with $I = 5.0 \times 10^{13}$ W/cm^2, $\omega = 0.057$, and $\phi = \pi/2$, are shown in Figure 5.7. The SPM LG-SFA works well for large N, were it reproduces the LG-SFA distribution. However, the SPM LG-SFA does not capture the interference structure for small N, since the SPM LG-SFA gives smooth distributions without any interference. Consequently, the interference for small N is not a result of interference between different saddle-points corresponding to the same momenta. This, however, does not mean that the interference is not caused by time-interference, as we shall see shortly. It turns out that insight into this question can be gained by examining the ellipticity dependence of the validity of the SPM LG-SFA. Furthermore, in view of the popularity of the SPM LG-SFA, knowledge about the validity of this method is important.

5.3 Ellipticity dependence of the SPM LG-SFA

Figure 5.8 presents the calculated, LG-SFA and SPM LG-SFA, momentum distribution as a function of ellipticity ϵ in the case of three optical cycles $N = 3$, peak intensity 5.0×10^{13} W/cm^2, angular frequency $\omega = 0.057$ and CEP $\phi = 0$. Starting from above in Figure 5.8 and moving down, we note that as ϵ is increased the distribution gets more broad and in the LG-SFA results the interference pattern, seen in Figure 5.3, gradually appears. In the linear case, we observe a very narrow distribution, compared to the circular case, without any interference pattern. The overall angular structure can again be explained by the semiclassical model, emphasizing the power of this simple model in explaining the basic behavior of ionization, regardless of the value of ϵ.

The LG-SFA and SPM LG-SFA yield almost identical results in the case of a linearly polarized field while there are, as we have seen, clear discrepancies in the case of a circularly polarized field. The discrepancies between LG-SFA and SPM LG-SFA tend to increase with increasing ϵ ($0 \leq \epsilon \leq \frac{\pi}{2}$). Interference-like patterns appear in the LG-SFA results but are absent in the SPM LG-SFA results. This feature can also be explained by the semiclassical model. Newton's second law states that

$$\Delta\vec{q} = \vec{E}(t_0)\Delta t_0, \tag{5.16}$$

relating the spread in momentum, $\Delta\vec{q}$, to the spread in ionization time, Δt_0. Let us restrict ourselves to the region in (q_x, q_y) space with highest yield, i.e., the electrons ionized near field maxima. The ratio between $|\Delta\vec{q}|$ and Δt_0 is then the maximum

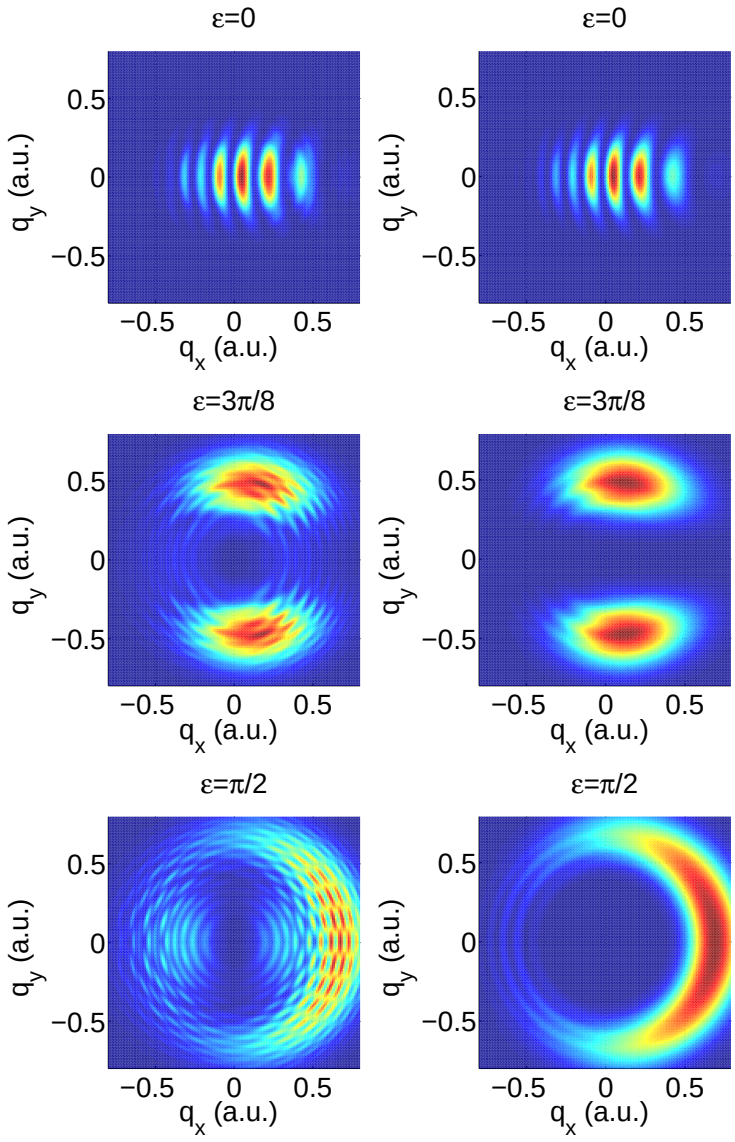

Figure 5.8. *SFA* (q_x, q_y) *momentum distribution for strong-field ionization of H(1s) for various values of ellipticity* ϵ*, with peak intensity* $I = 5.0 \times 10^{13}$ *W/cm*^{2}*,* $\omega = 0.057$ *(800 nm), number of cycles* $N = 3$ *and CEP* $\phi = 0$*. The left panels show results obtained with the LG-SFA while the right panels show results obtained with the SPM LG-SFA. The grid size is* $\Delta q_x = \Delta q_y = 0.01$*.*

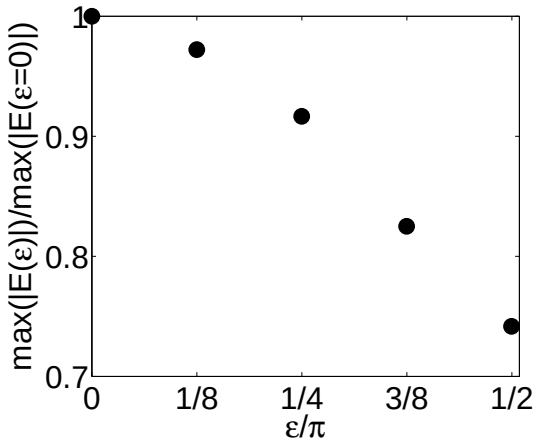

Figure 5.9. *Normalized maximum field strength during the pulse as a function of ellipticity ϵ, at peak intensity 5.0×10^{13} W/cm^2, 800nm and for three cycles, $N = 3$.*

field strength during the pulse. Figure 5.9 shows $\max(|\vec{E}(\epsilon)|)$ as a function of ϵ, normalized to $\max(|\vec{E}(\epsilon = 0)|)$, and we see that the field maximum during the pulse decreases monotonically as ϵ increases. The maximum field strength is about 25 pct. smaller in the circular case compared to the linear case. Thus, the spread in ionization time Δt_0 increases as a function of ϵ allowing more paths to contribute to the ionization process for a given spread in momentum. The width of the field maximum also increases as function of ϵ. As ϵ is increased more paths contribute making the SPM LG-SFA inaccurate, since it only accounts for a fixed number of paths.

This suggest an alternative interpretation, than the one given in section 5.2.1, of the interference seen in the circular case. Electrons ionized at different instants of time, close to $t = \tau/2$, interfere with each other, giving rise to the complicated interference structure seen for small N. The SPM LG-SFA does not capture this behavior, since it only includes a few of these paths. Figure 5.9 indicates that the SPM LG-SFA result for $\epsilon = \pi/2$ should improve considerably if $\max(|\vec{E}(\epsilon = \pi/2)|)$ is increases with a factor of 1.35, corresponding to a peak intensity of roughly 9.0×10^{13} W/cm^2. As Figure 5.10 shows, this is indeed the case. The interference pattern in the previous LG-SFA result is now almost completely absent and the agreement between the LG-SFA and SPM LG-SFA is quite good. The small discrepancies are due to the large width, of the field maximum, in the

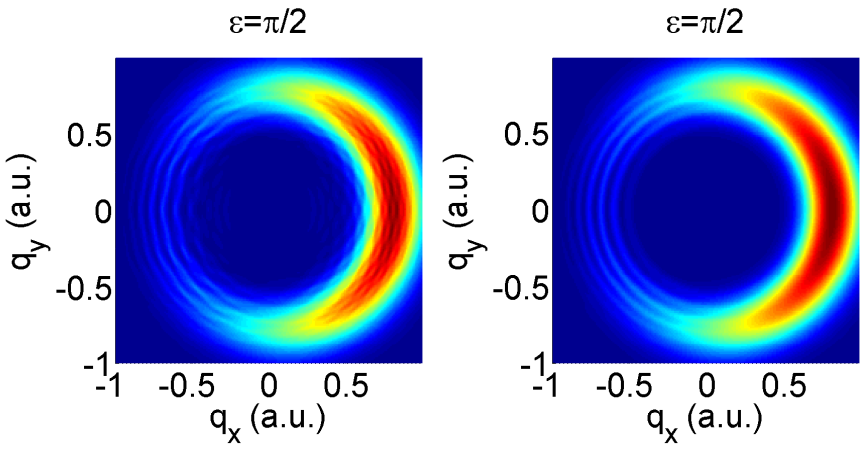

Figure 5.10. *Momentum distribution,* (q_x, q_y)*, for strong-field ionization of H(1s), with* $\epsilon = \pi/2$*, peak intensity* 9.0×10^{13} *W/cm*^{2}*,* $\omega = 0.057$ *(800 nm),* $N = 3$ *and* $\phi = 0$*. The left panel shows results obtained with the LG-SFA while the right panel shows results obtained with the SPM LG-SFA. The grid size is* $\Delta q_x = \Delta q_y = 0.01$*.*

$\epsilon = \pi/2$ case, which is independent of the peak intensity. Figure 5.9, on the other hand, suggests an increasing disagreement between LG-SFA and SPM LG-SFA if $\max(|\vec{E}(\epsilon = 0)|)$ is decreased by a factor of $1/1.35 \simeq 0.74$, corresponding to a peak intensity of about 2.7×10^{13} W/cm^2. This is indeed the case, as shown in Figure 5.11, where we observe serious discrepancies between LG-SFA and SPM LG-SFA. The discussion above shows that the validity of the SPM LG-SFA depends on: (i) The maximum field strength during the pulse and (ii) The width of the field maximum. The maximum field strength during the pulse has to exceed a certain minimum value depending on the pulse parameters (N, ω) and the width of the corresponding field maximum must be smaller than some maximum value, also depending on the pulse parameters. Notice, that this means, that the validity of the SPM LG-SFA may depend on the CEP for very short pulses, since $\max(|\vec{E}(\epsilon)|)$ depends on this quantity.

Point (i) above suggests the following formula for the minimum peak intensity $I_{\text{min}}(\epsilon)$, for which the SPM LG-SFA applies,

$$I_{\text{min}}(\epsilon) = I_{\text{min}}(\epsilon = 0) F(\epsilon)^2. \tag{5.17}$$

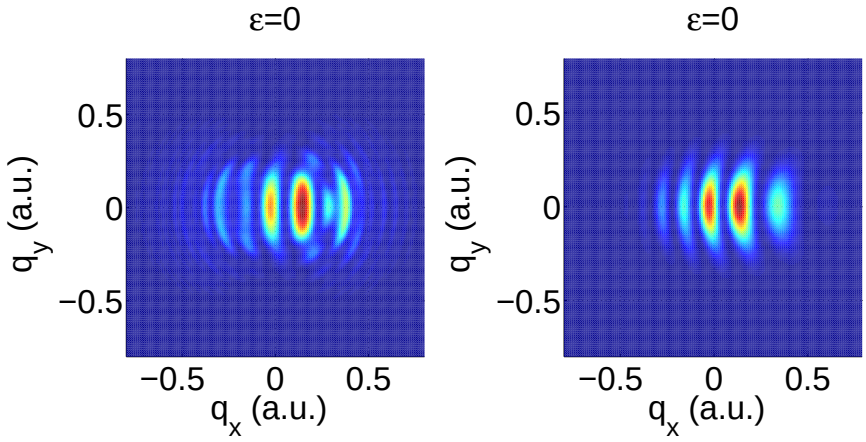

Figure 5.11. *Momentum distribution,* (q_x, q_y)*, of H(1s), with* $\epsilon = 0$*, peak intensity* 2.7×10^{13} *W/cm*^{2}*,* $\omega = 0.057$ *(800 nm),* $N = 3$ *and CEP* $\phi = 0$*. The left panel shows results obtain from the LG-SFA while the right panel shows results obtain from the SPM LG-SFA. The grid size is* $\Delta q_x = \Delta q_y = 0.01$*.*

The function F is given by

$$F(\epsilon) = \frac{\max(|\vec{E}(\epsilon = 0)|)}{\max(|\vec{E}(\epsilon)|)} \tag{5.18}$$

and in the case of $N = 3, \omega = 0.057$ and $\phi = 0$ the following empirical expression holds

$$F(\epsilon) = \exp\{-[(\epsilon + b)/c]^2\}, \tag{5.19}$$

where $b = 0.22$ and $c = 3.21$. A scan over different intensities shows that $I_{\text{min}}(\epsilon = 0, N = 3, \omega = 0.057) \simeq 5.0 \times 10^{13}$ W/cm^2, in good agreement with the present calculations. The agreement between SPM LG-SFA and LG-SFA increases (see Figure 5.7) when the number of optical cycles N increases, which seems to contradict with the explanation given here. The width in energy, however, decreases with increasing N giving an energy conserving delta function in the transition amplitude in the monochromatic limit $N \to \infty$. Thus, the above argument is not valid in the large N limit.

CHAPTER 6

Strong-field ionization of aligned molecules

There has in recent years been a substantial development in alignment and orientation techniques. Recent experiments not only succeeded in alignment of molecules but also in three dimensional orientation, thus giving unprecedented control over the molecular degrees of freedom [77–82]. This development provides even more fuel to branches like attoscience, femtochemistry among others. It is therefore natural to turn our attention towards aligned or oriented molecular targets. The topic of this chapter is strong-field ionization of aligned, or oriented, molecules by femtosecond laser pulses, with focus on the circularly polarized case. It is clear that, this topic is very difficult to handle in full generality. Full scale *ab-initio* calculations are only possible for the simplest molecules, H_2^+ and H_2, and even a molecule like H_2 is extremely difficult to treat with *ab-initio* approaches. Hence, if we wish to study larger molecules by *ab-initio* methods we are automatically lead to invoke the SAE. Methods exist for calculating effective potentials for selected molecules, but obtaining the potentials are not trivial and, regarding the subsequent solution of the TDSE, convergence is typically hard to achieve [83]. Furthermore, it is often far from trivial to extract the relevant physical quantity and physical picture, from a TDSE calculation. Thus, the situation calls for semi analytical approaches, like the LG-SFA, capturing the essential physical picture. However, we shall see that

the LG-SFA, as well as other semi analytical theories, runs into trouble with even small molecules, in the linear case.

Even though the main topic of this chapter is the circular case, we start by investigating how strong-field ionization of aligned O_2, N_2 and CS_2 molecules by linearly polarized pulses depend on the angle between the molecular axis and the polarization axis. Knowledge of the angular dependence is not only interesting from a fundamental point of view but also essential for applications, like molecular tomography [5, 6].

Next we turn to strong-field ionization of molecules by circularly polarized pulses, where we start with a general investigation on how angular nodal structure manifest in the photoelectron momentum distributions. Angular nodal structure is normally washed out in experiments on unaligned molecules, but in experiments on aligned, or oriented, molecules signatures show up in the ionization signal.

Finally, we study the strong-field ionization of polar molecules. While the first alignment experiments were on small linear molecules, the large polarizabilities and dipole moments of polar molecules makes it possible to, not only align, but also orient them, i.e., achieving a fixed head-to-tail ratio [77–82]. However, in order to model strong-field ionization of such molecules one need to take the Stark shift, of the energy levels, into consideration. The last section is devoted to this problem.

6.1 Strong-field ionization of laser-aligned molecules by linearly polarized laser pulses: Angular dependence of the ionization signal

Consider an aligned linear molecule interacting with an electric field, $\vec{E} = -\partial_t \vec{A}$, defined via the vector potential

$$\vec{A} = A_0 f(t) \cos(\omega t + \phi)\hat{e}_x, \tag{6.1}$$

where A_0 is the amplitude, ω the frequency and ϕ the CEP. We will start by examining two cases, N_2 and O_2, where the LG-SFA works quite well, at least for obtaining the angular dependence of the total ionization yield.

6.1.1 Strong-field ionization of laser-aligned O_2 and N_2 molecules by linearly polarized laser pulses: Comparison with experiments

Consider the ionization of an aligned $O_2(\pi_g)$ molecule by an 820 nm linearly polarized laser pulse with peak intensity $I = 1.3 \times 10^{14}$W/cm^2 and pulse duration

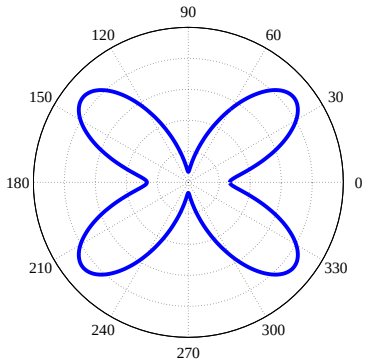

Figure 6.1. *The total ionization yield for O_2 as a function of the angle α obtained using the SPM LG-SFA with the initial wave function, i.e., the asymptotic form of the HOMO, given by $C_{21} = 1.04$, $C_{41} = 0.07$ and ionization potential 12 eV. The laser field parameters are, peak intensity $I = 1.3 \times 10^{14}$ W/cm^2, 820 nm and pulse duration 40 fs (FWHM)*

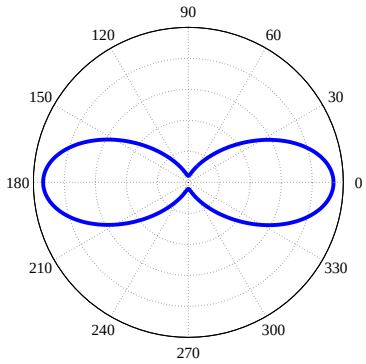

Figure 6.2. *The total ionization yield for N_2 as a function of the angle α obtained using the SPM LG-SFA with the initial wave function, i.e., the asymptotic form of the HOMO, given by $C_{00} = 3.46$, $C_{20} = 0.07$, $C_{40} = 0.12$ and ionization potential 15.6 eV. The laser field parameters are, peak intensity $I = 1.5 \times 10^{14}$ W/cm^2, 820 nm and pulse duration 40 fs (FWHM)*

40 fs (FWHM). Figure 6.1 shows the total ionization yield as a function of the angle α obtained using the SPM LG-SFA, with the initial wave function, i.e., the asymptotic form of the HOMO, Eq. (4.17), obtained in the following manner. First, the wave function is calculated using standard chemistry methods (see for instance [84]). Subsequently the asymptotic coefficients are calculated by fitting the wave function with the asymptotic form, with the asymptotic coefficients as fitting parameters. All the non-trivial asymptotic coefficients in this thesis are found using this procedure. The dependence of the yield on the angle, α, is evident from Figure 6.1, which predicts a maximum total yield for $\alpha = 40^\circ$, 140° and minimums in the yield for $\alpha = 0^\circ$, 90°. This result is in very good agreement, especially considering that laser-volume effects and alignment effects are not taken into account[1], with the recent measurements by Pavičić *et.al* [73] and appertaining MO-ADK calculations [85], taking laser volume effects into consideration.

Figure 6.2 shows the SPM LG-SFA total ionization yield for strong-field ionization of $N_2(\sigma_g)$, by an 820 nm linearly polarized laser pulse with peak intensity 1.5×10^{14}W/cm^2 and pulse duration 40 fs (FWHM), as a function of α. This results is again in very good agreement with the measurements on N_2 by Pavičić *et.al* [73]. The electron yield is highest for $\alpha = 0^\circ$ while $\alpha = 90^\circ$ provides the smallest yield.

The above shows that the LG-SFA is capable of providing the correct angle dependence of the ionization yield for the ionization of the simple molecules N_2 and O_2. However, the LG-SFA fails miserably for the ionization of molecules like CS_2 (and CO_2) as we now shall see.

6.1.2 Strong-field ionization of laser-aligned CS_2 molecules by linearly polarized laser pulses: Comparison with experiments

We start with a very brief review of the experiment performed by the group of H. Stapelfeldt, Department of Chemistry, Aarhus University [16]. They used a pump-probe scheme to investigate how ionization of the linear molecule CS_2 depends on the angle α between the internuclear axis and the polarization vector of the linearly polarized ionization pulse. More precisely, they investigated how the photoelectron angular distribution (PAD) from each multiphoton channel depends on α. Notice, that these measurements are energy-resolved, in contrast to the experiment by Pavičić *et.al* [73].

The $CS_2(\pi_g)$ molecules are first aligned along a given direction using a 0.5 ps (FWHM), $I = 2.9 \times 10^{12}$ W/cm^2 linearly polarized pump pulse. This pulse is too

[1] See the next section

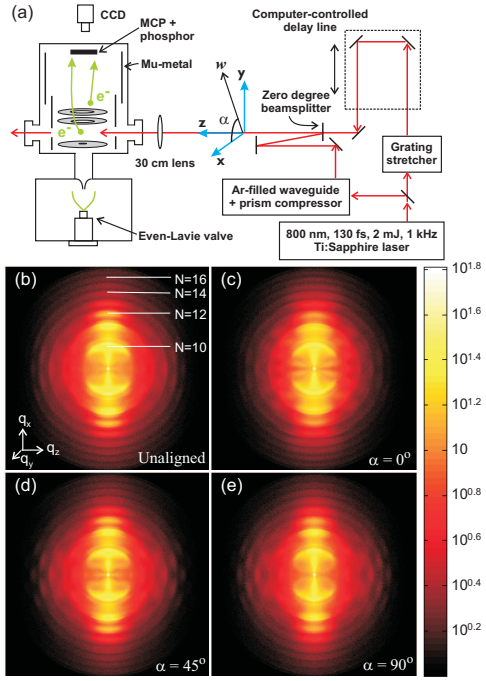

Figure 6.3. *The experimental setup in schematic form (a). The laser field is polarized along the x-axis, while the vector $\vec{w}$ shows the polarization of the alignment pulse. Figures (b)-(e) show the (q_x, q_z) momentum distributions for unaligned CS_2 molecules (b) and for aligned CS_2 molecules with $\alpha = 0^\circ$ (c), $\alpha = 45^\circ$ (d) and $\alpha = 90^\circ$ (e). The momentum distributions show clear ATI-peaks, see, for instance, (b) where N denotes the number of absorbed photons corresponding to the peak.*

weak to ionize CS_2 so its sole purpose is to align the molecules. The CS_2 molecules are then, after a delay corresponding to the first half revival, exposed to the 25 fs (FWHM), 800 nm and $I = 7.7 \times 10^{13}$ W/cm^2 ionizing pulse. This pulse is strong enough to eject the single HOMO electron of CS_2. Electrons emitted are detected using a velocity map imaging spectrometer and thereby recorded using a CCD camera. The results are shown in Figure 6.3, which shows the (q_x, q_z) momentum distribution for unaligned molecules (b) and for aligned molecules with $\alpha = 0^\circ$ (c), $\alpha = 45^\circ$ (d) and $\alpha = 90^\circ$ (e).

Clear ATI-peaks are observed in the momentum distributions. Furthermore, we observe radial substructures in the two lowest order multiphoton channels due to Rydberg states shifted into resonance by the Stark shift. However, our focus is on the dependence of α, not on the radial structure. Clear differences between the

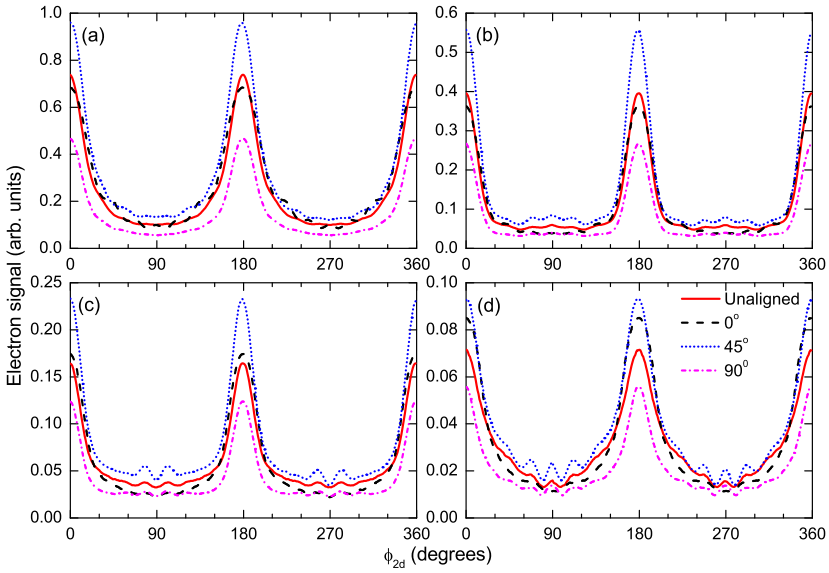

Figure 6.4. *Experimental PADs for the 11- (a), 12- (b), 13- (c) and 14-photon (d) ionization channels. Here ϕ_{2d} is the angle between the (q_x, q_z) projected electron ejection direction and the polarization axis of the laser pulse.*

momentum distributions corresponding to different alignment angles are observed, especially in the outermost ATI-peaks. In order to quantify this dependence on α, the photoelectron angular distribution (PAD) from each multiphoton channel is determined. The experimental results are shown in Figure 6.4. Here ϕ_{2d} denotes the angle between the direction of electron ejection and the polarization axis of the laser pulse. The first feature, we notice is that the total electron yield depends on α, $\alpha = 45^\circ$ provides the highest yield while $\alpha = 90^\circ$ provides the smallest. This is consistent with measurements on CO_2, which has the same symmetry, by Pavičić *et.al* [73]. The second feature, we notice is the change in the PADs along the z-axis, $\phi_{2d} = 90^\circ$ or $\phi_{2d} = 270^\circ$. For instance, in the 11-photon channel the $\alpha = 45^\circ$ signal is flat, without any oscillations, around $\phi_{2d} = 90^\circ$ or $\phi_{2d} = 270^\circ$, while the $\alpha = 45^\circ$ signal oscillates in the 14-photon channel.

In order to quantitative model this experiment, we have to take two important things into consideration: (i) Laser-volume effects and (ii) effects originating from the alignment pulse. Let us start with laser-volume effects. All the calculations in this thesis, so far, are performed on a single atom or molecule situated at the center

of the laser-beam. In an experiment, however, there is a large number of molecules and only a fraction of these are situated near the center of the beam, which means that only a fraction of the molecules actually experience the real peak intensity, i.e., the intensity at the center of the beam. The remaining molecules experience a lower intensity depending on where they are situated within the beam. We have to make a volume weighted average over all the different intensities in order to compensate for this effect. Assuming a uniform distribution of molecules within the beam, we obtain [65]

$$\frac{\partial^2 P}{\partial q_x \partial q_z}(q_x, q_z; I_{\text{peak}}) \propto \int_0^{I_{\text{peak}}} \frac{\partial^2 P}{\partial q_x \partial q_z}(q_x, q_z; I) \left(-\frac{\partial V}{\partial I} dI \right). \tag{6.2}$$

Here I_{peak} denotes the peak intensity and $(\partial V/\partial I)dI$ gives the volume element for the intensity between I and $I + dI$. When $dI > 0$, $dV < 0$ explaining the sign in the formula. Furthermore, assuming that the intensity profile is Lorentzian in the propagation direction and Gaussian in the transverse direction one can show that [65]

$$-\frac{\partial V}{\partial I} dI \propto \frac{1}{I} \sqrt{\frac{I_{\text{peak}}}{I} - 1} \left(\frac{I_{\text{peak}}}{I} + 2 \right). \tag{6.3}$$

Regarding the alignment part, the alignment pulse creates a coherent superposition of different rotational states, meaning that the orientation of the internuclear axis becomes time-dependent. Shortly after the alignment pulse, the molecules are primarily aligned along the polarization axis for the alignment pulse. As time goes, the molecules rotate and after a delay (0.76 ps in our case) the molecules are again primarily aligned along the polarization axis for the alignment pulse. This is the basic principle behind field-free alignment. Assume that the degree of alignment is described by the distribution $G_\alpha(\Omega_{\vec{R}})$, where $\vec{R}$ denotes the internuclear axis. We have to average our calculated signal over all the different orientations weighted by the alignment distribution in order to compare with the experiment signal [86]

$$S(q_x, q_z, \alpha) \propto \int G_\alpha(\Omega_{\vec{R}}) \frac{\partial^2 P}{\partial q_x \partial q_z}(q_x, q_z; I_{\text{peak}}, \Omega_{\vec{R}}) d\Omega_{\vec{R}}. \tag{6.4}$$

The procedure for calculating the alignment distribution is described in [16, 87].

We are now ready to go through the procedure. First, we calculate the single molecule momentum distribution $\frac{\partial^2 P}{\partial q_x \partial q_z}(q_x, q_z; I, \Omega_{\vec{R}})$ for a number of different intensities I and orientations $\Omega_{\vec{R}}$. This is done using the SPM LG-SFA[2], described in chapter 4, where the HOMO is expanded in partial waves with $C_{2,\pm 1} = \mp 2.14$,

[2]The SPM LG-SFA is expected to be accurate for the parameters considered here.

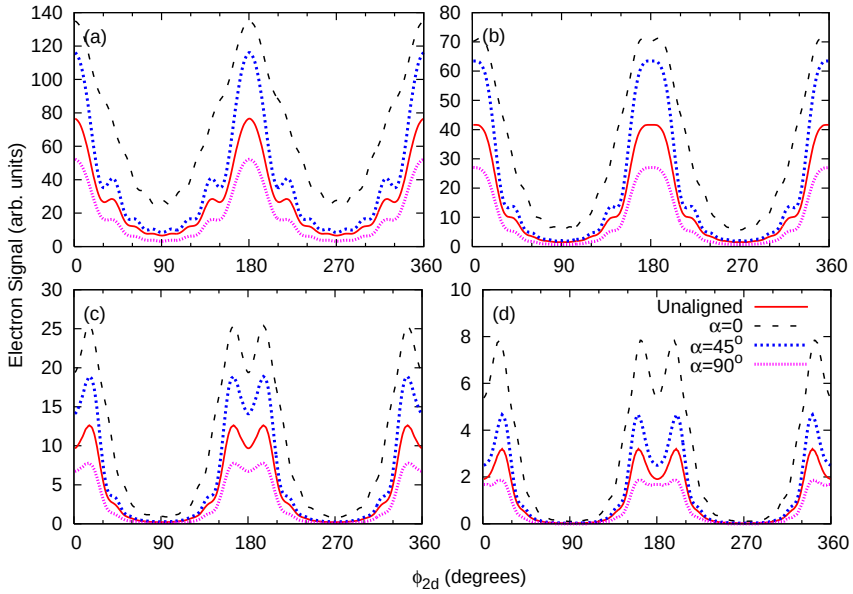

Figure 6.5. *Theoretical PADs for the 11- (a), 12- (b), 13- (c) and 14-photon (d) ionization channels. Here ϕ_{2d} is the angle between the (q_x, q_z) projected electron ejection direction and the polarization axis of the laser pulse.*

$C_{4,\pm1} = \mp 1.00$, $C_{6,\pm1} = \mp 0.16$ and ionization potential 10.08 eV. The coefficients are found using the procedure described in the previous section. Subsequently, we perform the intensity averaging and then average over all the different orientations to obtain the measurable signal. Finally, we integrate radially over each multiphoton peak in order to obtain the PAD for each multiphoton channel. Our results are shown in Figure 6.5. The theoretical results are clearly in qualitative agreement with the experimental results, with minima in the signals at $\phi_{2d} = 90°$ (270°) and maxima around $\phi_{2d} = 0°$ (180°). There are, however, significant discrepancies. Our SPM LG-SFA model generally overestimates the angle dependence. Furthermore, the order of the curves is wrong. Theory predicts in decreasing order $\alpha = 0°, 45°$, unaligned, $90°$ while the experimental data gives $\alpha = 45°$, unaligned, $0°, 90°$ for the 11 and 12 photon channels and $\alpha = 45°, 0°$, unaligned, $90°$ for the 13 and 14 photon channels.

A possible source to the discrepancies is the use of the SAE. Calculations show that the signal from the HOMO-1 is completely suppressed compared to the signal from the HOMO due to the large difference in binding energy, $I_{\text{HOMO}-1} - I_{\text{HOMO}} = 4.52$eV. Nevertheless, many electron effects may play a role. A second explanation

could be a bending of the linear CS_2 molecule, but this is ruled out by calculations (not shown). The discrepancies between theory and experiment could also be associated with the excited state spectrum of the CS_2 molecule and the neglect of the final Coulomb interaction. The SFA completely neglects the excited states and the final Coulomb interaction. Remember that we actually observed signature of intermediate Rydberg states in the experimental data [16], indicating that excited states indeed play a role in the experiment.

Similar breakdown of the LG-SFA is seen for the strong-field ionization of CO_2, where the LG-SFA, VG-SFA as well as the MO-ADK fail to reproduce the measured angular dependence of the total ionization yield [73]. This breakdown has motivated several different theoretical studies [88–92], attributing the discrepancies to electron correlation effects and multiple orbital contributions [88], dynamics in the excited state manifold [89], intermediate core excitation [91] and coherent core trapping [92]. Needless to say, no consensus regarding strong-field ionization of CO_2 has been reached. Understanding the PADs for molecules like CS_2 and CO_2 is one of the many challenges to theory in the future.

After this short detour, we now return to the main topic of this chapter, namely, strong-field ionization of aligned or oriented molecular targets by strong circularly polarized laser pulses. We start out with a general investigation with emphasis on orbital angular structure.

6.2 Strong-field ionization of oriented targets by circularly polarized pulses: Signatures of the orbital angular nodal structure

The development described in the introduction to this chapter motivates a detailed investigation of strong-field ionization of oriented targets, aligned in the case of symmetric molecules, by strong laser pulses with special emphasis on orbital structure, e.g., effects of orbital symmetry. The bulk of experimental and theoretical work within strong-field physics have dealt with linearly polarized laser pulses, however, there is now a growing interest in the study of ionization of atoms and molecules by elliptically polarized pulses [61, 93–96]. The effects of angular orbital structure in the ionization by linearly polarized laser fields have previously been studied for direct electrons [97,98] as well as for rescattered electrons [15,99]. When it comes to the probing of angular orbital structure through photoelectron angular distributions, or momentum distributions, the use of a strong circularly polarized probe rather than a linearly polarized one has, however, two major ad-

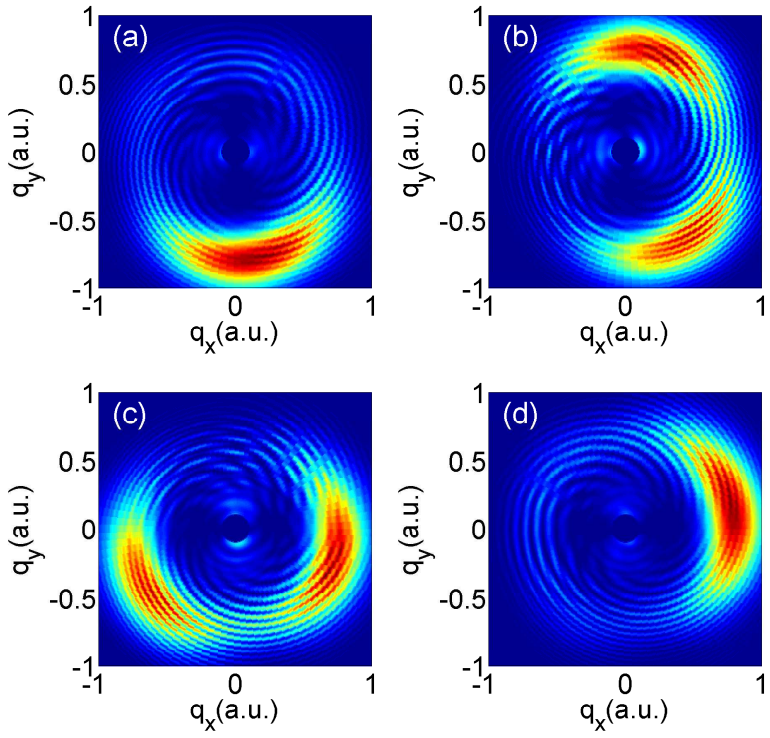

Figure 6.6. *Momentum distributions, $\partial^3 P/\partial q_x \partial q_y \partial q_z|_{q_z=0}$, from the SAE TDSE calculation for the $3p_x$ (a, b) and $3p_y$ (c, d) states of Ar for the following choice of laser parameters: Angular frequency $\omega = 0.057$, corresponding to 800 nm, peak intensity $I = 1.06 \times 10^{14} W/cm^2$, CEP $\phi = -\pi/2$ (a, c), $\phi = 0$ (b, d) and number of optical cycles $N = 3$.*

vantages: (i) In the circularly polarized field, an electron born in the continuum is constantly driven away from the nucleus due to the polarization. This dynamics minimizes rescattering effects as well as interference between wave packets launched at different instants of time during the ionizing pulse. Thus, the use of circularly polarized laser pulses entails a cleaner ionization signal with respect to orbital structure. (ii) The polarization plane is two-dimensional which permits for a more transparent interrogation of angular orbital structure, as we shall see in this section. In fact, it has recently been shown experimentally that strong-field ionization of three-dimensional oriented C_7H_5N molecules by a circularly polarized field, polarized in the nodal planes of the outermost orbitals, provides a unique probe of the angular nodal structure [10]. In this section, we focus on the case

where the laser polarization plane is perpendicular to a nodal plane and examine to what extent the angular nodal structure is imprinted in the momentum distribution. This also allows us to extent the discussion in chapter 5, section 5.1, to the general case, where the initial state is non-spherical.

Figure 6.6 shows the photoelectron momentum distributions for ionization of an Argon atom initially prepared in a $3p_x$ or $3p_y$ state, modeling an oriented target, aligned in the case of a symmetric target, with a single nodal plane. The $3p_x$ and $3p_y$ states, in particular, serve as models for investigating ionization of a molecular orbital with π symmetry. In the strong near infrared laser field, the ionization is tunneling-like and the photoelectron is born in the continuum at a relatively large distance from the centre-of-mass. After the ionization, the circularly polarized field drives the electron away from the core, which in turn minimizes the importance of the detailed structure of the molecular potential at small distances. Figure 6.6 is obtained by solving the SAE TDSE using the method described in chapter 3 (see Eq. (3.2)) with the frozen electrons described by an effective potential (see [100]). Note that, the scattering states entering Eq. (3.2) are obtained by solving the time-independent Schrödinger equation for the effective potential. More precisely Figure 6.6 shows the TDSE momentum distributions, evaluated in the xy plane of polarization, for the $3p_x$ (a, b) and $3p_y$ (c, d) initial states of Ar, probed by an 800 nm 3-cycle laser pulse with peak intensity $I = 1.06 \times 10^{14}\mathrm{W/cm}^2$ and CEP $\phi = -\pi/2$ (a, c) , $\phi = 0$ (b, d). The distributions are calculated using a 4096 points radial grid extending to $r_{\max} = 400$, maximum angular momentum $l_{\max} = 40$ and a time-step of 0.005. Notice that the ionization potential for the Ar(3p) state is 15.76 eV. The low-energy part $\sqrt{q_x^2 + q_y^2} < 0.1$ has been removed for better graphical display. For the $3p_x$ state with $\phi = -\pi/2$, Figure 6.6(a), and $3p_y$ state with $\phi = 0$, Figure 6.6(d), we observe a distribution with a single dominant peak, which as expected from the discussion in chapter 5 is located near $\vec{q} \approx -\vec{A}(\tau/2)$. In the two other cases we observe a splitting of this peak into two nearly symmetric peaks. As we now show these main features are explained using the SPM LG-SFA and are due to the nodal angular structure of the initial state.

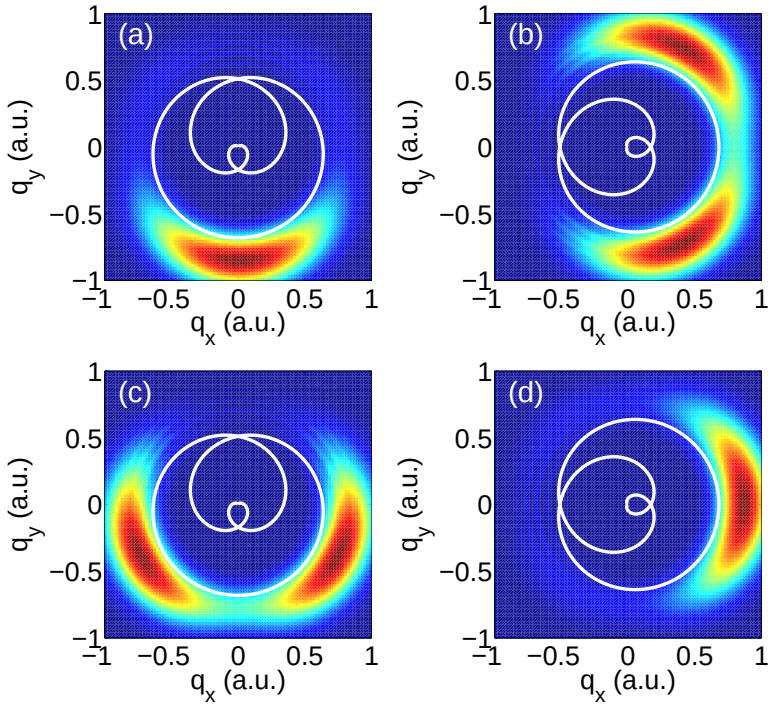

Figure 6.7. *SPM LG-SFA momentum distributions, $\partial^3 P/\partial q_x \partial q_y \partial q_z|_{q_z=0}$, for the $3p_x$ (a, b) and $3p_y$ (c, d) states of Ar for the following choice of laser parameters: Angular frequency $\omega = 0.057$, corresponding to 800 nm, peak intensity $I = 1.06 \times 10^{14} W/cm^2$, CEP $\phi = -\pi/2$ (a, c), $\phi = 0$ (b, d) and number of optical cycles $N = 3$. The white curves show a parametric plot of $-\vec{A}(t)$ from Eq. (2.14). If no nodal planes are along the polarization at time $t = \tau/2$, the dominating peak in the distribution follows the simple formula $\vec{q}_{final} \simeq -\vec{A}(\tau/2)$ as seen in (a) and (d). If on the other hand the field peaks in the direction of the angular node (b), (c), the dominating peak in the distribution splits.*

Figure 6.7 shows the momentum distributions obtained using the SPM LG-SFA, evaluated in the plane of polarization, for the $3p_x$ (a, b) and $3p_y$ (c, d) initial states of Ar, for 800 nm light and peak intensity $I = 1.06 \times 10^{14}\mathrm{W/cm^2}$, CEP $\phi = -\pi/2$ (a, c), $\phi = 0$ (b, d) and three optical cycles $N = 3$. The SPM LG-SFA results clearly reproduce the general structures of the TDSE distributions, except for an overall angular shift and a spiral like interference structure, both discussed in chapter 5. It was shown in chapter 5, in the case of a spherically symmetric initial state, that the SPM LG-SFA momentum distribution reflects the shape of the vector potential. For completeness, we repeat the argument: Due to the exponential dependence of the rate on the field strength, ionization predominantly occurs at the times t when the magnitude of the electric field is close to the maximum $|\vec{E}(\tau/2)|$. Assuming that the (classical) electron is born in the continuum with zero initial velocity and that it subsequently moves under the influence of the electric field only, we obtain $\vec{q}_{\text{final}} = -\vec{A}(t_i)$ with t_i the instant of ionization ($\vec{q}_{\text{final}} = -\vec{A}(\tau/2)$ dominates). However, in the case of a non-spherical initial state, this simple argument has to be extended to take into account the shape of the initial state, the angular nodal structure in particular. For example, it may happen that the field is in a nodal plane of the initial state at $t = \tau/2$ and hence ionization at field maximum will be suppressed due to symmetry reasons[3]. In other words, it is in this more general case the shape of the vector potential, electric field and initial state that determines the overall structure of the momentum distribution. The results in Figure 6.6 and Figure 6.7 clearly illustrate this combined effect. Let us start by analyzing the results for the $3p_x$ state and let us concentrate on the SPM LG-SFA results to make the discussion as simple as possible. Figure 6.7(a) shows the SPM LG-SFA momentum distribution in the plane of polarization for $\phi = -\pi/2$ and $3p_x$ initial state. We observe a distribution with a single peak located near $-\vec{A}(\tau/2)$, in good agreement with the semiclassical model. In the case of $\phi = -\pi/2$, $\vec{E}(\tau/2) = E_x(\tau/2)\hat{x}$ points in the direction of maximum electron density (see Figure 6.8(a)), while both $\vec{E}$ and $3p_x$ are symmetric with respect to $(x, y) \to (x, -y)$. This leads to a single peak situated at $\vec{q} \sim -\vec{A}(\tau/2) \propto -\hat{y}$ and symmetric with respect to $(q_x, q_y) \to (-q_x, q_y)$, in good agreement with the calculated distribution. Figure 6.7(b) shows the SPM LG-SFA momentum distribution, in the plane of polarization, for $\phi = 0$ and a $3p_x$ initial state. We observe two peaks, symmetric with respect to $(q_x, q_y) \to (q_x, -q_y)$, in contrast to the simplest single peak semiclassical prediction. In the case of $\phi = 0$, $\vec{E}(\tau/2) = E_y(\tau/2)\hat{y}$

[3]The time-evolution operator and the Fourier transform preserves the angular nodal plane, provided that the field coincides with the angular nodal plane. Consequently, emission along the field direction at $\tau/2$ is suppressed.

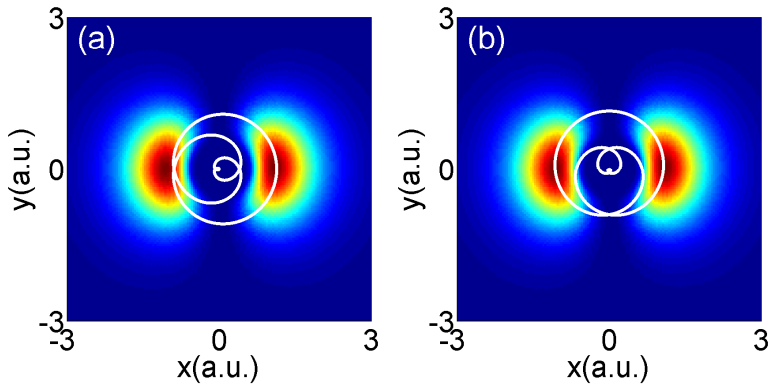

Figure 6.8. *Electron density in the $3p_x$ state of Ar together with a parametric plot of the electric field, corresponding to the vector potential shown in Figure 6.7, scaled by a factor. In (a), $\phi = -\pi/2$, the electric field at the peak of the pulse $t = \tau/2$ points in a direction where the orbital density is largest. In (b), $\phi = 0$, the electric field at the peak of the pulse runs through the orbital node (no electron density).*

lies in the nodal plane of $3p_x$ (see Figure 6.8(b)), i.e., there is no electron density to ionize at $t = \tau/2$, and hence ionization at field maximum is suppressed. Thus, the single peak from before splits into two symmetric peaks, due to the fact that $\vec{E}$ and $3p_x$ are symmetric with respect to $(x, y) \rightarrow (-x, y)$, again in good agreement with the obtained distribution. The precise location of the peaks is determined by a competition between the rate arising from the electric field and the density profile of the initial state. The results shown in Figure 6.7(c) and Figure 6.7(d) are explained using similar reasoning. Notice, that the signature of the nodal plane in the momentum distribution is advanced by $\pi/2$ compared to the orbital angular nodal structure, reflecting the $\pi/2$ phase between the electric field and the vector potential.

The above discussion of Figure 6.6, Figure 6.7 and Figure 6.8 clearly shows, that the nodal structure of the initial orbital is mapped uniquely to the momentum distribution, when the laser polarization plane is perpendicular to the nodal plane. This effect is even more visible in the case of a slightly longer femtosecond pulse, where the asymmetry caused by the CEP of the pulse is smaller. Figure 6.9 shows the SPM LG-SFA (q_x, q_y) momentum distribution, $\partial^2 P/\partial q_x \partial q_y$, for H(1s), H($2p_x$), H($2p_y$) and H($3d_{xy}$) states obtained using the same parameters as in Figure 6.6 and Figure 6.7 except that the number of optical cycles is increased to

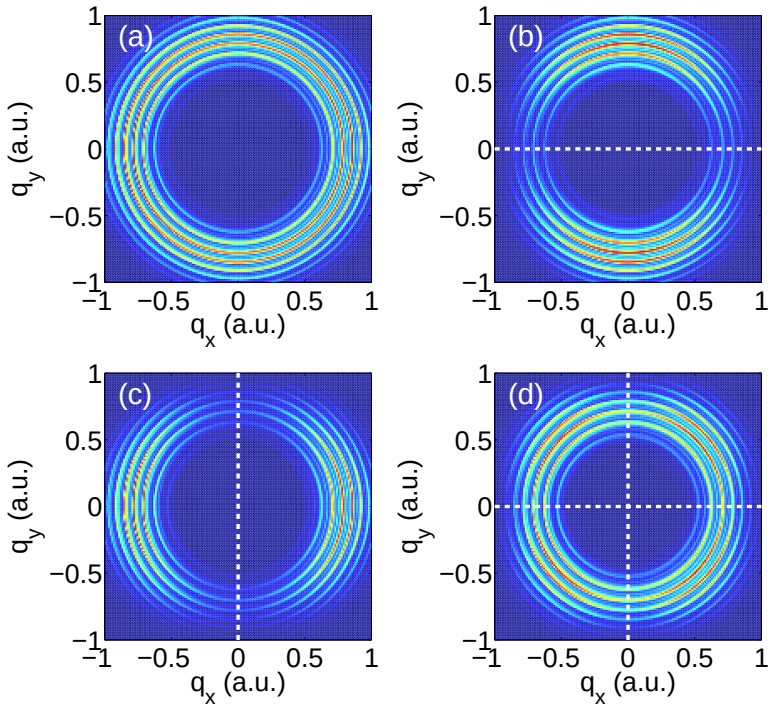

Figure 6.9. *SPM LG-SFA momentum distributions* $\partial^2 P/\partial q_x \partial q_y = \int (\partial^3 P/\partial q_x \partial q_y \partial q_z) dq_z$ *for 1s (a),* $2p_x$ *(b),* $2p_y$ *(c) and* $3d_{xy}$ *(d) obtained using the following laser parameters: Angular frequency* $\omega = 0.057$*, corresponding to 800 nm, peak intensity* $I = 1.0 \times 10^{14} W/cm^2$*, CEP* $\phi = 0$ *and number of optical cycles* $N = 20$*. The binding energy of the* $2p_x$*,* $2p_y$ *and* $3d_{xy}$ *states are modified to the ground state energy of H. The white dashed lines show regions where ionization is suppressed.*

$N = 20$ and $I = 1.0 \times 10^{14}\mathrm{W/cm^2}$. The use of the SPM LG-SFA is for computational convenience and is justified by the results presented on Ar and the discussion in chapter 5. The binding energy of the H($2p_x$), H($2p_y$) and H($3d_{xy}$) states have been artificial modified to -0.5, by modifying $\kappa = \sqrt{2I_p}$ (see Eq. (4.17)), in order to compare with the H(1s) result. Figure 6.9 clearly shows, that the angular nodal structure is mapped uniquely to the momentum distribution. This is particular clear, when compared with Figure 6.10, which shows the asymptotic densities for the 1s, $2p_x$, $2p_y$ and $3d_{xy}$ states. The electric field is almost constant during the dominant cycles of the field, i.e., there is no competition between the rate arising from the electric field and the density profile. In the case of H(1s) we observe a

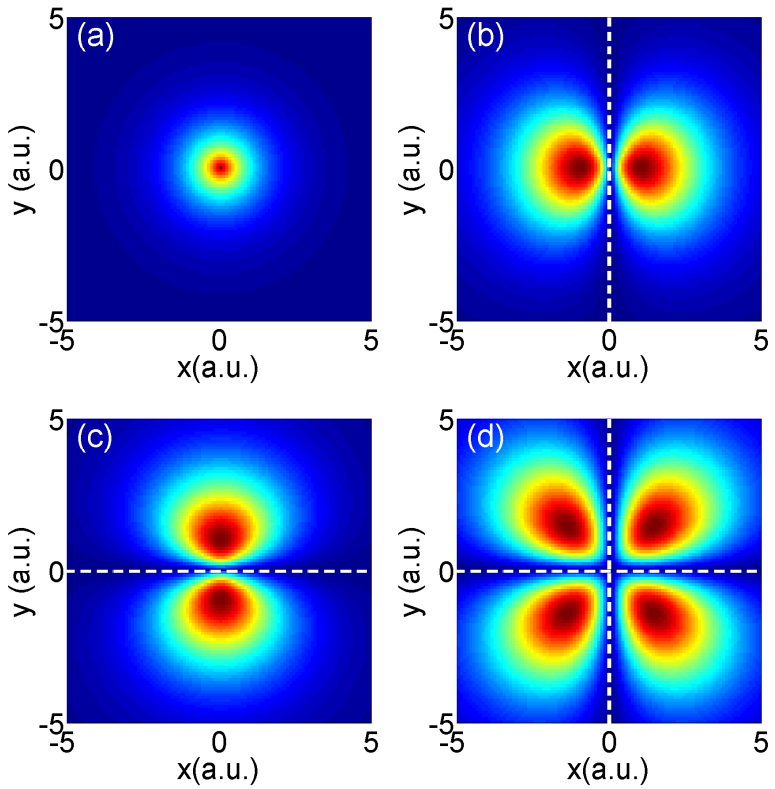

Figure 6.10. *The asymptotic density for H(1s) (a), H(2p$_x$) (b), H(2p$_y$) (c) and H(3d$_{xy}$) (d). The white dashed lines show the angular nodal planes.*

completely symmetric distribution with well-resolved ATI peaks while ionization is strongly suppressed along the x-axis (y-axis) in the case of H(2p$_x$) (H(2p$_y$)) and along the x-axis and y-axis in the case of H(3d$_{xy}$), reflecting the angular nodal structures in Figure 6.10. Ionization is suppressed along the x-axis (y-axis) in the case of H(2p$_x$) (H(2p$_y$)) due to the yz (xz) nodal plane which is shifted 90° by the vector potential. There are two angular nodal planes for H(3d$_{xy}$), namely the xz and yz planes, suppressing ionization along the y-axis and x-axis. Until now, we have only examined model systems. Hence, in order to stress the generality of the method we show that the angular nodal structure of a real molecule, benzene, is mapped uniquely to the momentum distribution.

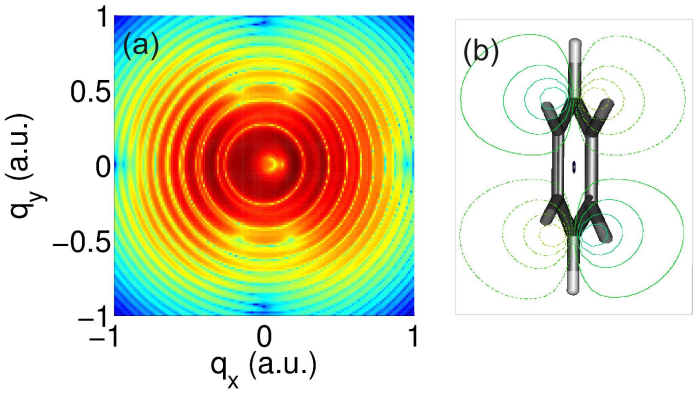

Figure 6.11. *(a): SPM LG-SFA momentum distribution evaluated in the xy polarization plane for a benzene molecule oriented in the yz plane. (b): Plot of the participating orbital. The calculation is performed with the following laser parameters: Angular frequency $\omega = 0.057$, corresponding to 800 nm, peak intensity $I = 5.0 \times 10^{13} W/cm^2$, CEP $\phi = 0$ and number of optical cycles $N = 10$. The color scale is logarithmic*

Figure 6.11 shows the momentum distribution evaluated in the $xy-$plane associated with strong field ionization of the HOMO of the benzene molecule (Figure 6.11(b)), the molecule lies in the $yz-$plane. The laser parameters are: $\omega = 0.057$, laser peak intensity 5.0×10^{13} W/cm^2, CEP $\phi = 0$ and $N = 10$ optical cycles. Benzene has two degenerate HOMO orbitals: The first one (not shown) has a nodal plane coinciding with the $xy-$plane, whereas the second, $(C_{2-1}, C_{21}, C_{4-1}, C_{41}, C_{6-1}, C_{61}) = (0.74, -0.74, -0.27, 0.27, 0.04, -0.04)$ and $I_p = 9.24$ eV, (contours in Figure 6.11(b)) has a nodal plane coinciding with the $xz-$plane. The first degenerate orbital does not contribute to ionization in the $xy-$plane, from symmetry arguments. The second degenerate orbital has one additional nodal plane in yz, which makes it similar to the H$(3d_{xy})$. However, note that the charge density is not four-fold symmetric and that one node is shallower than the other. All these features are indeed mapped uniquely to the momentum distribution (Figure 6.11(a)), which reveal two nodal structures, one of which is more clear than the other. The benzene case demonstrates the potential of this

method for interrogating the orbital structure of large and complex molecules. The results shown in this section indicates that strong-field ionization by a circularly polarized pulse may serve as a probe for revealing changes in the angular nodal structure, e.g., changes occurring during a chemical reaction. Note, however, that the LG-SFA does not account for the distortion of the initial orbital, due to the non-zero polarizability of benzene, which may wash out some of the angular nodal structure. In general, one should be aware that, for polar molecules with large dipole moments and polarizabilities, the interaction with the field may blur some of the angular nodal structure of the molecule. However, in the cases where the angular nodal plane coincides with the polarization plane the angular nodal structure cannot be washed out.

6.3 Strong-field ionization of asymmetric polar molecules by circularly polarized pulses: Inclusion of the Stark shift in the LG-SFA

The alignment experiments described in section 6.1 were on symmetric molecules with permanent dipole moments zero, however, there has recently been a large interest in the ionization of polar molecules [10, 101]. In the case of strong-field ionization of polar molecules with large permanent dipole moments, e.g., HF, HCl, LiF and OCS, the Stark shift of the energy levels cannot, in general, be neglected. The strong laser field induces large modulations of the energy levels leading to large modulations of the ionization potential and accordingly the ionization rate. Consequently, ionization of such molecules gives rise to new interesting phenomena, not seen for non-polar systems, e.g., strong suppression of the ionization yield in specific parts of momentum space [10].

The LG-SFA, and the MO-ADK, does not account for the Stark shift. Hence, the standard LG-SFA is not appropriate for studying strong-field ionization of molecules with large permanent dipole moments and polarizabilities. The MO-ADK was recently Stark shift corrected, by replacing the field-free ionization potential with the Stark shift corrected time-dependent ionization potential, in order to explain recent experimental results on the strong-field ionization of one-dimensional oriented OCS and three-dimensional oriented C_7H_5N [10]. However, a tunneling model does not account for two important features: (i) The coherence of the ionizing wave packet is automatically lost in a tunneling model and, consequently, interference effects of the ionizing wave packet is lost. (ii) Consider a polar molecule oriented in such a way that the electric field polarization

plane coincides with a nodal plane of the ionizing molecule orbital. Then emission along the field direction is forbidden, due to symmetry reasons, and accordingly ionization is suppressed. Nevertheless, in the ADK and MO-ADK one assumes that tunneling occurs opposite to the field direction, which, in this case, cannot be true. The ADK and MO-ADK momentum distribution, at time of emission, is proportional to $\exp(-q_\perp\sqrt{2I_p}/|\vec{E}(t)|)$, where $q_\perp$ is the momentum of the emitted electron transverse to the instantaneous field direction and I_p the ionization potential at time of emission [15, 102]. This, of course, is not correct due to the presence of the nodal plane. In order to circumvent this problem, an ad-hoc modification of the pre-exponent factor of the tunneling amplitude is necessary [10]. The LG-SFA automatically accounts for the angular nodal structure of the initial state, as exemplified in the previous section.

The above discussion motivates the development of a Stark shift corrected LG-SFA, which has the simplicity of the standard LG-SFA and in addition captures the basic physics in the strong-field ionization of polar molecules. This can be done in the tunneling limit, $\gamma < 1$, as we shall see in the following section.

6.3.1 The static Stark shift

Consider a polar molecule interacting with a strong static electric field, $\vec{E}$. The presence of the electric field perturbs the energy levels of the molecule according to

$$E^{\mathrm{M}}(\vec{E}) = E^{\mathrm{M}}(0) - \vec{\mu}^{\mathrm{M}} \cdot \vec{E} - \frac{1}{2}\vec{E} \cdot \alpha^{\mathrm{M}}\vec{E} + ..., \tag{6.5}$$

where $E^{\mathrm{M}}(0)$ is the field-free energy of the molecule, $\vec{\mu}^{\mathrm{M}}$ is the dipole moment and α^{M} is the polarizability tensor. Higher order terms, e.g., the hyperpolarizability, is not shown and will be neglected in the following discussion. The energy of the cation can be expanded in a similar way leading to the following expression for the ionization potential of the molecule

$$I_p(\vec{E}) = I_p(0) + \Delta\vec{\mu} \cdot \vec{E} + \frac{1}{2}\vec{E} \cdot \Delta\alpha\vec{E}, \tag{6.6}$$

where $I_p(0) = E^{\mathrm{I}}(0) - E^{\mathrm{M}}(0)$ is the ionization potential under field-free conditions and

$$\Delta\vec{\mu} = \vec{\mu}^{\mathrm{M}} - \vec{\mu}^{\mathrm{I}}, \tag{6.7}$$

$$\Delta\alpha = \alpha^{\mathrm{M}} - \alpha^{\mathrm{I}}. \tag{6.8}$$

Here M/I refer to the molecule/cation. Hence, the ionization potential of the molecule depends on the size of the applied electric field, the angle between the electric field and the effective dipole moment $\Delta\vec{\mu}$ and the angle between the electric field and the effective polarizability term, $\Delta\alpha\vec{E}$. Note, that we do not account for different ionization channels leading to different ion states with possibly different dipole moments and polarizabilities.

Consider the ionization of a polar molecule by a strong electric field in the tunneling limit. The above discussion shows, that the ionization potential change during the pulse duration, i.e., the ionization probability is modulated by the ionization potential in addition to the shape of the electric field and the orbital angular structure. The LG-SFA does not account for the Stark shift, since it describes a transition from the field-free initial state to a Volkov state. However, it is possible to approximately Stark shift correct the LG-SFA in the tunneling limit.

6.3.2 Stark shift corrected LG-SFA

The Stark shift affects both the neutral molecule and the cation and it is therefore natural to start the derivation in the many particle picture, i.e., without invoking the SAE at first. However, the first part of the discussion closely resembles the derivation given in chapter 4 and is therefore omitted here. The transition amplitude from the initial state Ψ_0 to the final state Ψ_f, describing the liberated electron and the residual ion, is

$$T_{\vec{q}} = -i \int_0^\tau \langle \Psi_f(t)|V(t)|\Psi_0(t)\rangle dt, \tag{6.9}$$

where $V(t) = \sum_{j=1}^{n} \vec{r}_j \cdot \vec{E}(t)$ is the length gauge interaction operator, with n the number of electrons. We are only interested in single ionization and furthermore restrict the discussion to the independent particle model. Hence, the initial wave function is approximated with a Slater determinant

$$\Psi_0(t) = \frac{1}{\sqrt{n!}}\text{det}|\psi_1(\vec{r}_1)\psi_2(\vec{r}_2)...\psi_n(\vec{r}_n)| \exp(-iE^M(0)t), \tag{6.10}$$

where ψ_i and $\vec{r}_i$ denotes the ith electron orbital and spatial coordinate, respectively. In the SFA, the interaction between the liberated electron and the residual ion is neglected. In addition, we also neglect the interaction between the field and the residual ion. Thus

$$\Psi_f(t) = \frac{1}{\sqrt{n!}}\text{det}|\psi_1(\vec{r}_1)\psi_2(\vec{r}_2)...\psi^{\text{V}}_{\vec{q}}(\vec{r}_n,t)| \exp(-iE^I(0)t), \tag{6.11}$$

with $\psi^{\mathrm{V}}_{\vec{q}}(\vec{r}_n, t)$ denoting a length gauge Volkov wave function with asymptotic momentum $\vec{q}$. Neglecting the non-orthogonality of the Volkov wave function with the remaining wave functions, we arrive at the standard LG-SFA expression for the transition amplitude

$$T^{\text{LG-SFA}}_{\vec{q}} = -i \int_0^\tau \langle \psi^{\mathrm{V}}_{\vec{q}}(\vec{r}, t) | \vec{r} \cdot \vec{E} | \psi_n(\vec{r}) \rangle \exp(iI_p(0)t) dt. \tag{6.12}$$

This formula does not account for the Stark shift. However, it is possible, in the adiabatic limit, to include the Stark shifts in the wave functions Ψ_0 and Ψ_f. If we assume, that the neutral molecule, before ionization, and the cation, after ionization, are affected adiabatically by the presence of the electric field the two wave functions Ψ_0 and Ψ_f are changed to

$$\begin{aligned}\Psi_0(t) =& \frac{1}{\sqrt{n!}} \det|\psi_1(\vec{r}_1, \vec{E}(t))\psi_2(\vec{r}_2, \vec{E}(t))...\psi_n(\vec{r}_n, \vec{E}(t))| \\ & \times \exp\left(-i \int_0^t E^M(\vec{E}(t'))dt'\right)\end{aligned} \tag{6.13}$$

and

$$\begin{aligned}\Psi_f(t) =& \frac{1}{\sqrt{n!}} \det|\psi_1(\vec{r}_1, \vec{E}(t))\psi_2(\vec{r}_2, \vec{E}(t))...\psi^{\mathrm{V}}_{\vec{q}}(\vec{r}_n, t)| \\ & \times \exp\left(-i \int_0^t E^I(\vec{E}(t'))dt'\right).\end{aligned} \tag{6.14}$$

The adiabatic ansatz is valid provided that $\omega \ll I_p(\vec{E}(t))$[4]. In addition to the modification of the energy phase, due to the Stark shift of the energy levels, we have indicated the modification of the single particle orbitals by the field. It is very difficult to account for such distortions of the single particle orbitals, but it is nevertheless clear, in the case of large polarizabilities[5], that the distortion can be very substantial and that the use of the field-free orbitals is, in general, not appropriate. In this regard, we expect that the single particle orbital for the outermost bound electron will be the one that is mostly changed while the other orbitals will be affected by the field to a less extent. However, in the case where the spatial distortions of the single particle orbitals can be neglected, the transitions amplitude reduces to the following

$$T_{\vec{q}} = -i \int_0^\tau \langle \psi^{\mathrm{V}}_{\vec{q}}(\vec{r}, t) | \vec{r} \cdot \vec{E} | \psi_n(\vec{r}) \rangle \exp\left(i \int_0^t I_p(\vec{E}(t'))dt'\right) dt. \tag{6.15}$$

[4]The cation is, of course, more tightly bound than the neutral molecule. Hence, if the adiabatic ansatz is valid for the molecule then it is automatically valid for the cation.

[5]The polarizability term is responsible for the distortion of the orbital

This integral can be evaluated using the method described in chapter 4, section 4.1, in connection with the derivation of the standard LG-SFA. Invoking the saddle-point approximation, using the asymptotic form of the initial state, leads to

$$T_{\vec{q}} = \sum_{t_s} f(t_s) \sqrt{\frac{2\pi i}{S''(t_s)}} \exp(iS(t_s)), \tag{6.16}$$

with

$$S(t) = \frac{1}{2}\int_0^t (\vec{q} + \vec{A}(t'))^2 dt' + \int_0^t I_p(\vec{E}(t'))dt' \tag{6.17}$$

the Stark shift corrected semiclassical action and t_s a relevant saddle-point. Notice, that the inclusion of the Stark shift in some cases, one example is C_7H_5N, modifies the overall behavior of the $\exp(iS)$ surface compared to the non-Stark case, discussed in chapter 4. This means that the rule regarding the number of relevant saddle-points, discussed in chapter 4, not necessarily applies in the Stark case. The function f is given by

$$\begin{aligned} f(t_s) \propto & \sum_{lm} \frac{C_{lm}}{2^l} \frac{\Gamma(l+\nu+2)}{\Gamma(l+3/2)} \left(\frac{Q(t_s)}{i\kappa}\right)^l Y_{lm}(\hat{Q}(t_s)) \\ & {}_2F_1\left(\frac{l-\nu}{2}, \frac{l-\nu+1}{2}; l+\frac{3}{2}; -\frac{Q(t_s)^2}{\sqrt{2I_p(0)}}\right) \frac{1}{S_0'(t_s)^\nu}, \end{aligned} \tag{6.18}$$

provided that we neglect the Stark shift in pre-exponent. Here $\vec{Q}(t) = \vec{q} + \vec{A}(t)$, $\nu = Z/\sqrt{2I_p(0)}$, Z is the ionic charge and

$$S_0'(t_s) = \frac{1}{2}(\vec{q} + \vec{A}(t_s))^2 + I_p(0). \tag{6.19}$$

6.3.3 Application of the Stark shift corrected LG-SFA

We are now ready to illustrate the performance of the corrected LG-SFA by calculating the photoelectron momentum distributions for strong-field ionization of one-dimensional oriented OCS and three-dimensional oriented C_7H_5N. The relevant dipole moments and polarizabilities are taken from [10][6]. Notice that $\gamma = 0.89$ for the OCS case and $\gamma = 1.16$ for the C_7H_5N case, slightly stressing the applicability of the method. Let us start with OCS. Consider a one-dimensional oriented, in such

[6] Supplementary information

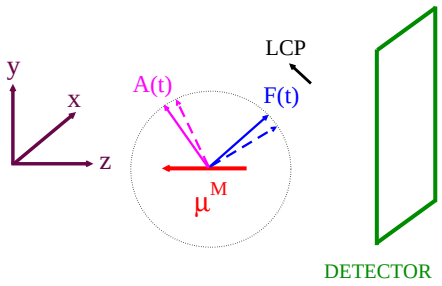

Figure 6.12. *The experimental geometry that is considered in the present calculations. See text for details.*

a way that the O-end points in the positive z-direction, OCS molecule interacting with a left-handed circularly polarized laser pulse described by the vector potential

$$\vec{A}(t) = \frac{A_0}{\sqrt{2}} f(t) \begin{pmatrix} 0 \\ \sin(\omega t + \phi) \\ \cos(\omega t + \phi) \end{pmatrix}, \tag{6.20}$$

where A_0 is the amplitude, f the envelope, ω the frequency and ϕ the CEP. All the results shown in this section are obtained using "long" pulses, $N = 10$, and hence the CEP does not a play a role. Notice that, this field is polarized in the yz-plane contrary to the convention used in the rest of the thesis. This is done in order to better compare with the experimental and theoretical results in [10]. The setup is shown in Figure 6.12. Figure 6.13(a) shows the standard SPM LG-SFA momentum distribution (see Eq. (4.29)), $\partial^2 P/\partial q_x \partial q_y$, for strong-field ionization of OCS by a circularly polarized field, with the parameters: frequency $\omega = 0.057$ (800 nm), peak intensity $I = 2.44 \times 10^{14}$W/cm^2, number of optical cycles $N = 10$, and CEP $\phi = 0$. The HOMO of OCS is two-fold degenerate with one orbital in the (y, z)-plane, with a nodal plane in the (x, z)-plane, and the other orbital perpendicular to the first one[7]. The momentum distribution shown in Figure 6.13(a) is obtained by incoherently adding the momentum distributions from each HOMO. However, the contribution from the (y, z)-plane orbital dominates, since the polarization plane coincide with the nodal plane of the (x, z)-orbital thereby suppressing ionization

[7]The C_{lm} coefficients for the (y, z)-plane orbital are $C_{1\pm1} = \mp 0.27$, $C_{2\pm1} = \pm 1.77$, $C_{3\pm1} = \mp 0.53$, $C_{4\pm1} = \pm 0.14$ and $C_{5\pm1} = \mp 0.09$. The coefficients for the (x, z)-plane orbital are obtained by a rotation of the (y, z)-plane orbital by $\pi/2$ around the molecular axis.

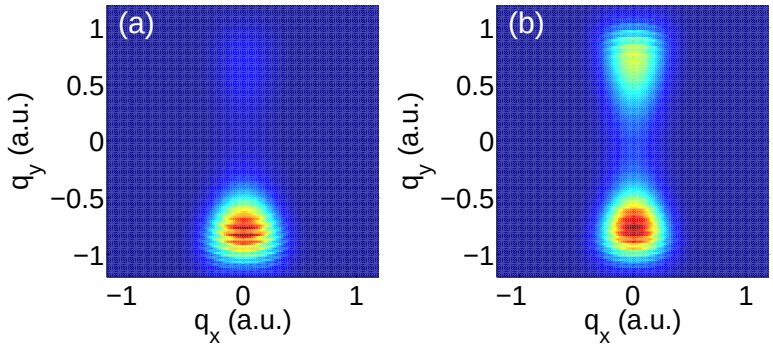

Figure 6.13. *Photoelectron momentum distributions, $\partial^2 P/\partial q_x \partial q_y$, for the ionization of OCS, one-dimensional oriented such that the O-end points in the positive z-direction. The laser parameters are: frequency $\omega = 0.057$ (800 nm), peak intensity $I = 2.44 \times 10^{14}$ W/cm^2, number of optical cycles $N = 10$ and CEP $\phi = 0$. The distribution (a) is obtained using the standard SPM LG-SFA while the distribution (b) is obtained by including the Stark shift in the exponent, i.e., using Eq. (6.16) and Eq. (6.18).*

from this orbital. The discussion of Figure 6.13(a) is therefore restricted to the (y, z)-plane orbital.

The standard LG-SFA produces an asymmetric distribution, where the probability for ionization with $q_y < 0$ is larger than the probability for ionization with $q_y > 0$. This can be explained by looking at the HOMO orbital, i.e., the (y, z)-orbital (see Figure 6.14(a)). The geometric structure of the HOMO favors ionization when the electric field has a component in the positive $z-$direction compared to the case where the electric has a negative z component, since the majority of the charge is situated near the S-end. According to the semiclassical model

$$\vec{q} = -\vec{A}(t_0), \tag{6.21}$$

where t_0 is the instant of ionization. When $\vec{E}$ points in the positive z-direction $\vec{A}$ points in the positive y-direction and hence the final momentum has a negative y-component. Contrary, when $\vec{E}$ points in the negative z-direction $\vec{A}$ points in the negative y-direction and accordingly the final momentum has a positive y-component. Thus, ionization with a positive q_y-component is suppressed compared to ionization with a negative q_y-component. This explains the observed asymmetry in Figure 6.13(a). Unfortunately, this contradicts the recent experimental results from [10], where the $q_y < 0$ part is suppressed compared to $q_y > 0$ part. Figure

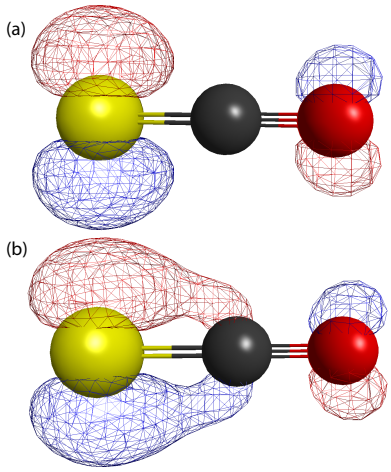

Figure 6.14. *The OCS molecule with the S pointing to the left and the O to the right. The nuclei are at the equilibrium nuclear positions: -2 (Sulfur), 0.99 (Carbon) and 3.2 (Oxygen). (a) Iso-contour of the HOMO of OCS at spatial points where the norm of the wave function is 0.1. (b) As (a) but now including a static field of magnitude 0.0586 pointing towards the S-end. The comparison between (a) and (b) illustrates how the external field pulls the electron charge density in the direction opposite to the field. In both cases the calculations were performed, using GAMESS [84] with a triple-zeta valence basis set and added diffuse orbitals.*

6.13(b) shows the Stark shift corrected momentum distribution, obtained using Eq. (6.16) and Eq. (6.18), for the same parameters as in Figure 6.13(a). The inclusion of the Stark-shift in the exponent clearly increases the $q_y > 0$ part but clearly not enough to reproduce the trend seen in [10]. The exponent $\exp(iS)$ favors ionization when the electric field has a negative z component, since the Stark-shift corrected ionization potential is smaller in that case. Nevertheless, this effect is not enough to beat the non-Stark shifted pre-exponent, containing the field-free HOMO. Consequently, in the case of OCS, we cannot neglect the Stark shifts influence on the pre-exponent, i.e., the field modification of the initial orbital. The modification of the initial orbital is due to polarization term in Eq. (6.5) and at the peak of the electric field the polarization term is actually much larger than the dipole term. Consequently, the HOMO charge distribution simply follows the quasi-static field during the interaction (this is illustrated in Figure 6.14(b)). As a result, the pre-exponent should not favor ionization in any specific direction and it seems reasonable to model the initial HOMO by an s-state. This approach was also

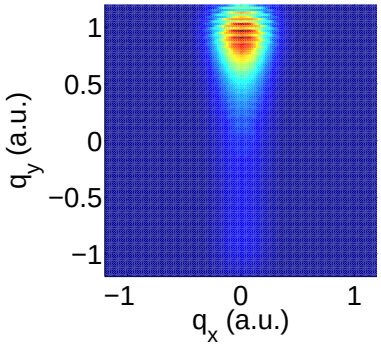

Figure 6.15. *Stark shift corrected photoelectron momentum distribution, $\partial^2 P/\partial q_x \partial q_y$, for the ionization of an artificial OCS molecule, one-dimensional oriented such that the O-end points in the positive z-direction, where the initial orbital entering Eq. (6.18) is modeled by a simple s-orbital. The laser parameters are the same as in Figure 6.13.*

used in [10] in order to reproduce the experimental findings using the Stark shift corrected MO-ADK. Figure 6.15 shows the Stark shift corrected momentum distribution, with the same parameters as in Figure 6.13, for an OCS molecule with the initial state modeled by an s-state retaining the Stark shifted ionization potential of OCS. Now, the momentum distribution show asymmetry in the correct direction, viz in agreement with the experimental findings, and furthermore compare very well with the Stark shift corrected tunneling results, see Figure 3(a) in [10]. This agreement is due to the general accordance between tunneling and LG-SFA in the adiabatic limit [48].

Next we turn to the case of strong-field ionization of three-dimensional oriented C_7H_5N. Assume that the molecule is oriented in such a way that the CN-end points in the positive z-direction while the benzene ring is fixed in the (y, z)-plane. The HOMO, and the HOMO-1, then has a nodal plane in the (y, z)-plane, i.e., a nodal plane coinciding with the polarization plane. For the purpose of describing the ionization of this molecule, using the Stark shift corrected MO-ADK, an ad-hoc correction accounting for the nodal plane structure is needed. For the LG-SFA no such correction is needed, nodal plane structure is automatically taken into account. The structure of the HOMO off the nodal plane, which is not washed away by the field, is modified by the field. The polarizability term is even more dominant than in the case of OCS and it is therefore inaccurate to use the field-free HOMO as initial state. Similar reasoning as before suggest the use of an

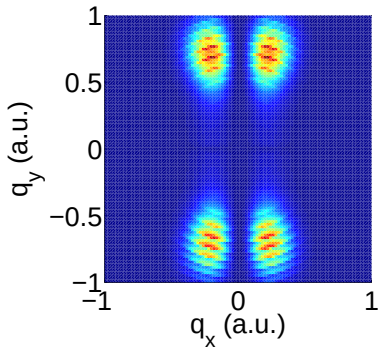

Figure 6.16. *Stark shift corrected photoelectron momentum distribution, $\partial^2 P/\partial q_x \partial q_y$, for the ionization of an artificial C_7H_5N molecule, three-dimensional oriented such that the N-end points in the positive z-direction while the benzene-ring is fixed in the (y,z) plane. The initial orbital entering Eq. (6.18) is modeled by a simple p_x-orbital. The laser intensity is $I = 1.2 \times 10^{14}$ W/cm^2. The other laser parameters are the same as in Figure 6.13.*

initial p_x orbital [10, 102]. Figure 6.16 shows the Stark shift corrected momentum distribution[8], obtained using Eq. (6.16) and Eq. (6.18), for strong-field ionization of C_7H_5N modeled by an initial p_x state. We clearly see the signature of the nodal plane of C_7H_5N in the distribution and we observe very good agreement with the tunneling calculations on C_7H_5N presented in Figure 3(c) in [10].

[8]Notice, that only the most dominant saddle-point have been included in Eq. (6.16).

CHAPTER 7

Summary and outlook

Strong-field ionization is a fundamental part of strong-field physics, nonetheless because it triggers other strong-field processes. We have, in this thesis, investigated several different aspects of strong-field ionization, ranging from finite-bandwidth effects in the ionization of atoms by few-cycle circularly polarized laser pulses to effects of the static Stark shifts in strong-field ionization of polar molecules.

We started with a general geometric characterization of carrier-envelope phase (CEP) effects in the ionization of atoms and molecules by circularly polarized few-cycle pulses. Under special conditions, e.g., a physical system rotational invariant with respect to rotations around the propagation direction of the field, a change in the CEP manifest itself as a simple rotation around the axis of propagation. The temporal shape of a few-cycle pulse depends critically on the CEP making the ionization dynamics, just like other strong-field processes, sensitive to the CEP.

Moving on, we compared the length-gauge strong-field approximation (LG-SFA) with *ab-initio* calculations, based on the time-dependent Schrödinger equation. This allowed us to identify and explain striking signatures of the Coulomb potential in the photoelectron momentum distribution. More precisely, we observed counterintuitive angular shifts in the photoelectron momentum distribution for strong-field ionization of atoms by circularly polarized few-cycle laser pulses, similar to the shifts recently observed experimentally by P. Eckle *et.al* [61]. The dominant direction of electron ejection is shifted compared to the direction pre-

dicted by strong-field theories like LG-SFA and ADK. We showed that such angular shifts was due to the non-vanishing commutator between the Hamiltonian and the z-component of the angular momentum, i.e., the shifts are caused by a subtle interplay between the field and the binding potential.

Moreover, we investigated bandwidth effects, giving rise to complicated interference structures, in strong-field ionization of atoms by few-cycle circularly polarized laser pulses. In addition, we examined how the validity of the saddle-point method for evaluation of the LG-SFA transition amplitude (SPM LG-SFA) depends on the ellipticity of the pulse for fixed peak intensity. For different pulse parameters, the validity of the SPM LG-SFA depends on two criteria: (i) The maximum field strength during the pulse has to exceed a certain value and (ii) The width of the field maximum must be smaller than some certain value.

Next we turned our attention towards molecules interacting with strong femtosecond laser pulses. We started with the ionization of aligned molecules by linear polarized laser pulses, with focus on the following question: How does the ionization signal depend on the angle between the alignment axis and the polarization axis. We showed that while the LG-SFA was able to explain experimental results on O_2 and N_2 [73], it breaks down for molecules like CO_2 [73] and CS_2 [16]. The precise physical origin of this breakdown is still open, although several theoretical explanations have been proposed.

After this short detour, we moved on to the main topic of the chapter, strong-field ionization of aligned, or oriented, molecules by circularly polarized laser pulses. First, we examined how the angular nodal structure of aligned, or oriented, molecules shows up in the ionization signal. More precisely, we showed, using simple model systems, that the angular nodal structure is mapped uniquely to the momentum distribution. As a result, strong-field ionization by circularly polarized pulses may serve as probes for investigating changes in the angular nodal structure during chemical reactions. This conclusion was further strengthen by strong-field calculations on benzene, C_6H_6. However, it is still unclear, how robust the method is against, for instance, Stark and polarizability effects.

Finally, we examined strong-field ionization of polar molecules with large permanent dipole moments and polarizabilities. In order to describe the ionization of such molecules, the Stark shift of the energy levels of both the neutral molecule and the cation has to be accounted for. Unfortunately, the LG-SFA does not account for the Stark shift. Nevertheless, we showed how to systematic Stark shift correct the LG-SFA in the tunneling limit, using the adiabatic ansatz, thereby deriving a simple formula for the Stark shift corrected LG-SFA transition amplitude for ionization. It is possible to Stark shift correct the MO-ADK, however, the MO-ADK

does not account for two important features included in the LG-SFA, namely wave packet interference and nodal plane structure (if the field is located in an angular nodal plane) [10, 102]. The results obtained using this simple approach compared well with recent experimental results.

The rapid experimental development within strong-field physics necessitates theory capable of explaining the different measurements. From a theoretical point of view our main tools are either *ab-initio* theory or semi analytical theories, like the LG-SFA. On one hand, *ab-initio* theory is hindered by the complexity of the numerics involved. The time-dependent Schrödinger equation is in principle exact, but that does not help us if convergence is almost impossible to achieve or the relevant physical quantity completely impossible to extract. Semi analytical theories like the strong-field approximation or molecular tunneling theory are more accessible, but it is also clear that further development are needed for such theories to meet the requirements set up by the experimental development. The Stark shift corrected LG-SFA, for instance, falls short regarding several important issues. First, the Stark shift corrected LG-SFA does not properly account for the distortion of the initial molecular orbital. This distortion can be very substantial, as we have seen, and it would be desirable with a model including this distortion. One approach is to calculate the asymptotic coefficients for the HOMO in a static electric field for each field orientation, thus, giving a sequence of time-dependent asymptotic coefficients which could be used in a LG-SFA calculation. However, this is on very shaky ground from a theoretical point of view, since the asymptotic expansion is not valid when the electric field is present. Second, the method, being based on the SFA, does not account for the molecular potential, including the dipole term, in the final state. One possible solution to this problem is to include the dipole term in the same way the Coulomb potential was approximately included in [72]. Furthermore, the LG-SFA neglects the excited state spectrum, which may play an essential role due to resonances.

Consequently both tools, *ab-initio* theory and semi-analytical theories, needs to be improvement, which, luckily, will provide interesting and important work for the theoretical physicists in the years to come.

APPENDIX A

Transformation of the Schrödinger equation

The TDSE for an atom interacting with an electric field described by the vector potential ($\eta = \omega t - \vec{k}\cdot\vec{r}$)

$$\vec{A}(\vec{r},t;\phi) = \frac{A_0}{\sqrt{2}}\sin^2\left(\frac{\eta}{2N}\right)(\cos(\eta+\phi)\hat{e}_x + \sin(\eta+\phi)\hat{e}_y) \tag{A.1}$$

reads

$$i\frac{\partial}{\partial t}\Psi = \left(\hat{H}_0 + \sum_{j=1}^{n}\vec{A}(\vec{r},t;\phi)\cdot\vec{\hat{p}}_j + \frac{1}{2}\sum_{j=1}^{n}\vec{A}(\vec{r},t;\phi)^2\right) \tag{A.2}$$

We now perform the unitary transformation

$$\Psi' = \exp\left(i\hat{J}_z\phi\right)\Psi, \tag{A.3}$$

which corresponds to a rotation by $-\phi$ around the z-axis. The transformed TDSE is given by

$$\begin{aligned} i\frac{\partial}{\partial t}\Psi' = \Bigg(&\hat{H}_0 + \sum_{j=1}^{n}\exp\left(i\hat{J}_z\phi\right)\vec{A}(\vec{r}_j,t;\phi)\cdot\vec{\hat{p}}_j\exp\left(-i\hat{J}_z\phi\right) \\ &+\frac{1}{2}\sum_{j=1}^{n}\exp\left(i\hat{J}_z\phi\right)\vec{A}(\vec{r},t;\phi)^2\exp\left(-i\hat{J}_z\phi\right)\Bigg)\Psi'. \end{aligned} \tag{A.4}$$

Applying the Baker-Hausdorff lemma

$$\exp(i\hat{G}\lambda)\hat{A}\exp(-i\hat{G}\lambda) = \hat{A} + i\lambda[\hat{G},\hat{A}] + \frac{i^2\lambda^2}{2!}[\hat{G},[\hat{G},\hat{A}]] + \frac{i^3\lambda^3}{3!}[\hat{G},[\hat{G},[\hat{G},\hat{A}]]] + ... \tag{A.5}$$

on the term $\exp(i\hat{J}_z\phi)A_x(\vec{r}_j,t;\phi)\hat{p}_{x_j}\exp(-i\hat{J}_z\phi)$ yields

$$\begin{aligned}
&\exp(i\hat{J}_z\phi)A_x(\vec{r}_j,t;\phi)\hat{p}_{x_j}\exp(-i\hat{J}_z\phi) = A_x(\vec{r}_j,t;\phi)\exp(i\hat{J}_z\phi)\hat{p}_{x_j}\exp(-i\hat{J}_z\phi)\\
&= A_x(\vec{r}_j,t;\phi)\left(\hat{p}_{x_j} + i\phi[\hat{J}_z,\hat{p}_{x_j}] + \frac{i^2}{2!}[\hat{J}_z,[\hat{J}_z,\hat{p}_{x_j}]] + \frac{i^3}{3!}[\hat{J}_z,[\hat{J}_z,[\hat{J}_z,\hat{p}_{x_j}]]] + ...\right)\\
&= A_x(\vec{r}_j,t;\phi)\left(\hat{p}_{x_j} - \phi\hat{p}_{y_j} - \frac{1}{2}\phi^2\hat{p}_{x_j} + \frac{1}{3!}\phi^3\hat{p}_{y_j} + ...\right)\\
&= A_x(\vec{r}_j,t;\phi)(\hat{p}_{x_j}\cos(\phi) - \hat{p}_{y_j}\sin(\phi)),
\end{aligned} \tag{A.6}$$

as expected. Similar, one can show that

$$\exp(i\hat{J}_z\phi)A_y(\vec{r}_j,t;\phi)\hat{p}_{y_j}\exp(-i\hat{J}_z\phi) = A_y(\vec{r}_j,t;\phi)(\hat{p}_{y_j}\cos(\phi) + \hat{p}_{x_j}\sin(\phi)). \tag{A.7}$$

Consequently

$$\begin{aligned}
&\exp(i\hat{J}_z\phi)\vec{A}(\vec{r}_j,t;\phi)\cdot\vec{\hat{p}}_j\exp(-i\hat{J}_z\phi)\\
&= (A_x(\vec{r}_j,t;\phi)\cos(\phi) + A_y(\vec{r}_j,t;\phi)\sin(\phi))\hat{p}_{x_j}\\
&+ (A_y(\vec{r}_j,t;\phi)\cos(\phi) - A_x(\vec{r}_j,t;\phi)\sin(\phi))\hat{p}_{y_j}\\
&= \vec{A}(\vec{r}_j,t;\phi=0)\cdot\vec{\hat{p}}_j.
\end{aligned} \tag{A.8}$$

Furthermore

$$\exp\left(i\hat{J}_z\phi\right)\vec{A}(\vec{r}_j,t;\phi)^2\exp\left(-i\hat{J}_z\phi\right) = \frac{A_0^2}{2}\sin^2\left(\frac{\eta}{2N}\right) \tag{A.9}$$

Putting this together we have shown that

$$i\frac{\partial}{\partial t}\Psi' = \left(\hat{H}_0 + \sum_{j=1}^{n}\vec{A}(\vec{r}_j,t;\phi=0)\cdot\vec{\hat{p}}_j + \frac{1}{2}\sum_{j=1}^{n}\vec{A}(\vec{r},t,\phi=0)^2\right)\Psi'. \tag{A.10}$$

APPENDIX B

The initial state in momentum space

The purpose of this appendix is to calculate the Fourier transform of the wave function

$$\psi(\vec{r}) = \sum_{lm} C_{lm} r^{\nu-1} \exp(-\kappa r) Y_{lm}(\hat{r}), \tag{B.1}$$

i.e., ψ in momentum space $\tilde{\psi}(\vec{q})$. By definition

$$\begin{aligned}\tilde{\psi}(\vec{q}) &= \frac{1}{\sqrt{(2\pi)^3}} \int \exp(-i\vec{q}\cdot\vec{r})\psi(\vec{r})d\vec{r} \\ &= \frac{1}{\sqrt{(2\pi)^3}} \sum_{lm} C_{lm} \int \exp(-i\vec{q}\cdot\vec{r}) r^{\nu-1} \exp(-\kappa r) Y_{lm}(\hat{r}) d\vec{r}.\end{aligned} \tag{B.2}$$

We now expand the plane wave, $\exp(-i\vec{q}\cdot\vec{r})$, in spherical harmonics [103]

$$\begin{aligned}\exp(-i\vec{q}\cdot\vec{r}) &= 4\pi \sum_{l'=0}^{\infty} \sum_{m'=-l'}^{l'} (-i)^{l'} j_{l'}(qr) Y_{l'm'}(\hat{q}) Y^*_{l'm'}(\hat{r}) \\ &= 4\pi \sum_{l'm'} (-i)^{l'} j_{l'}(qr) Y_{l'm'}(\hat{q}) Y^*_{l'm'}(\hat{r}),\end{aligned} \tag{B.3}$$

where j_l is a spherical Bessel function, and thereby obtains

$$\begin{aligned}\tilde{\psi}(\vec{q}) &= \sqrt{\frac{2}{\pi}} \sum_{lml'm'} C_{lm} \int (-i)^{l'} j_{l'}(qr) Y_{l'm'}(\hat{q}) Y^*_{l'm'}(\hat{r}) r^{\nu-1} \exp(-\kappa r) Y_{lm}(\hat{r}) d\vec{r} \\ &= \sqrt{\frac{2}{\pi}} \sum_{lml'm'} C_{lm} (-i)^{l'} Y_{l'm'}(\hat{q}) \int_0^\infty r^{\nu+1} j_{l'}(qr) \exp(-\kappa r) dr \\ &\times \int Y_{l'm'}(\hat{r}) Y_{lm}(\hat{r}) d\Omega \\ &= \sqrt{\frac{2}{\pi}} \sum_{lm} C_{lm} (-i)^{l} Y_{lm}(\hat{q}) \int_0^\infty j_l(qr) r^{\nu+1} \exp(-\kappa r) dr. \end{aligned} \tag{B.4}$$

The spherical Bessel functions are related to the ordinary Bessel functions via the relation [103]

$$j_l(\rho) = \sqrt{\frac{\pi}{2\rho}} J_{l+1/2}(\rho), \tag{B.5}$$

which yields the following relation

$$\tilde{\psi}(\vec{q}) = \sum_{lm} C_{lm} (-i)^l Y_{lm}(\hat{q}) \sqrt{\frac{1}{q}} \int_0^\infty J_{l+1/2}(qr) r^{\nu+1/2} \exp(-\kappa r) dr. \tag{B.6}$$

Finally, we evaluate the radial integral using Gauss hypergeometric series [104]

$$\begin{aligned}\int_0^\infty J_{l+1/2}(qr) r^{\nu+1/2} \exp(-\kappa r) dr = \left(\frac{q}{2\kappa}\right)^{l+1/2} \frac{\Gamma(l+\nu+2)}{\Gamma(l+3/2)} \frac{\kappa^\nu \sqrt{\kappa}}{(\kappa^2+q^2)^{\nu+1}} \\ \times {}_2F_1\left(\frac{l-\nu}{2}, \frac{l-\nu+1}{2}; l+\frac{3}{2}; -\frac{q^2}{\kappa^2}\right),\end{aligned} \tag{B.7}$$

and obtain

$$\begin{aligned}\tilde{\psi}(\vec{q}) = \sum_{lm} C_{lm} \left(\frac{q}{i\kappa}\right)^l \frac{\kappa^\nu \Gamma(l+\nu+2)}{2^{l+1/2}\Gamma(l+3/2)(\kappa^2+q^2)^{\nu+1}} \\ \times {}_2F_1\left(\frac{l-\nu}{2}, \frac{l-\nu+1}{2}; l+\frac{3}{2}; -\frac{q^2}{\kappa^2}\right) Y_{lm}(\hat{q}).\end{aligned} \tag{B.8}$$

APPENDIX C

Asymptotic expansion of the integral $\int_{C_s - i\epsilon} \frac{\exp(iS)}{S'^{\nu}}$

This appendix is based on the derivation given in [48, 105]. We want to calculate the integral $\int_{C_s - i\epsilon} \frac{\exp(iS)}{S'^{\nu}}$, where C_s is the path defined by following the steepest descent from the saddle-point t_s, satisfying $S'(t_s) = 0$, and $\epsilon \to 0^+$. The integral gets is main contribution from the part of the path close to the saddle-point. This subpath can be parameterized as follows

$$t - t_s = (x - i\epsilon)Q_s, \tag{C.1}$$

where $x \in [-\delta; \delta]$, $\delta > 0$, and $Q_s = \sqrt{\frac{2i}{S''(t_s)}}$ is the direction of the steepest descent at $t = t_s$[1]. Expanding S to second order in $t - t_s$ gives

$$\begin{aligned} S(t) &= S(t_s) + \frac{1}{2}S''(t_s)(t - t_s)^2 \\ &= S(t_s) + ix^2 + 2\epsilon x - i\epsilon^2, \end{aligned} \tag{C.2}$$

[1] $-\frac{\pi}{4} \leq \arg(Q_s) \leq \frac{\pi}{4}$

and accordingly

$$\begin{aligned}\int_{C_s-i\epsilon} \frac{\exp(iS)}{S'^\nu} dt &\approx i^\nu \frac{\exp(iS(t_s))}{(S''(t_s))^\nu} \frac{1}{Q_s^{\nu-1}} \int_{-\delta}^{\delta} \frac{\exp(-x^2+2\epsilon i x+\epsilon^2)}{(\epsilon+ix)^\nu} dx \\ &\approx i^\nu \frac{\exp(iS(t_s))}{(S''(t_s))^\nu} \frac{1}{Q_s^{\nu-1}} \int_{-\infty}^{\infty} \frac{\exp(-x^2+2\epsilon i x+\epsilon^2)}{(\epsilon+ix)^\nu} dx\end{aligned} \tag{C.3}$$

The term $1/(\epsilon+ix)^\nu$ can be expanded as [48, 105]

$$\frac{1}{(\epsilon+ix)^\nu} = \frac{1}{\Gamma(\nu)} \int_0^\infty \eta^{\nu-1} \exp(-\eta\epsilon) \exp(-i\eta x) d\eta, \tag{C.4}$$

and hence

$$\begin{aligned}\int_{C_s-i\epsilon} \frac{\exp(iS)}{S'^\nu} dt \approx i^\nu \frac{\exp(iS(t_s))}{(S''(t_s))^\nu} \frac{1}{Q_s^{\nu-1}\Gamma(\nu)} \int_0^\infty \eta^{\nu-1} \exp(-\eta\epsilon) \\ \int_{-\infty}^{\infty} \exp(-x^2+i(2\epsilon-\eta)x+\epsilon^2) dx d\eta\end{aligned} \tag{C.5}$$

All what remains is now to calculate the two integrals

$$\begin{aligned}\int_{-\infty}^{\infty} \exp(-x^2+i(2\epsilon-\eta)x+\epsilon^2) dx &= \exp(\epsilon^2) \int_{-\infty}^{\infty} \exp(-x^2) \\ &\quad \times (\cos((2\epsilon-\eta)x) + i\sin((2\epsilon-\eta)x))\, dx \\ &= 2\exp(\epsilon^2) \int_0^\infty \cos((2\epsilon-\eta)x) \exp(-x^2) dx \\ &= \sqrt{\pi} \exp(\epsilon^2) \exp\left(-\frac{(2\epsilon-\eta)^2}{4}\right),\end{aligned} \tag{C.6}$$

which yields

$$\begin{aligned}\int_{C_s-i\epsilon} \frac{\exp(iS)}{S'^\nu} dt &\approx i^\nu \sqrt{\pi} \exp(\epsilon^2) \frac{\exp(iS(t_s))}{(S''(t_s))^\nu} \frac{1}{Q_s^{\nu-1}\Gamma(\nu)} \\ &\quad \times \int_0^\infty \eta^{\nu-1} \exp(-\eta\epsilon) \exp\left(-\frac{(2\epsilon-\eta)^2}{4}\right) d\eta \\ &\approx i^\nu \sqrt{\pi} \frac{\exp(iS(t_s))}{(S''(t_s))^\nu} \frac{1}{Q_s^{\nu-1}\Gamma(\nu)} \int_0^\infty \eta^{\nu-1} \exp(-\eta^2/4) d\eta \\ &\approx i^\nu \frac{\exp(iS(t_s))}{(S''(t_s))^\nu} \frac{\Gamma(\nu/2)}{2Q_s^{\nu-1}\Gamma(\nu)} 2^\nu \sqrt{\pi} \\ &\approx i^\nu \frac{\Gamma(\nu/2)}{2\Gamma(\nu)} \sqrt{\left(\frac{2\pi i}{S''(t_s)}\right)} (-2iS''(t_s))^{\nu/2} \frac{\exp(iS(t_s))}{(S''(t_s))^\nu}\end{aligned} \tag{C.7}$$

Bibliography

[1] A. Scrinzi, M. Y. Ivanov, R. Kienberger, and D. M. Villeneuve, "Attosecond physics", *J. Phys. B* **39**, R1 (2006).

[2] A. H. Zewail, "Femtochemistry: Recent Progress in Studies of Dynamics and Control of Reactions and Their Transition States", *J. Phys. Chem.* **100**, 12701 (1996).

[3] S. Baker, J. S. Robinson, C. A. Haworth, H. Teng, R. A. Smith, C. C. Chirilă, M. Lein, J. W. G. Tisch, and J. P. Marangos, "Probing Proton Dynamics in Molecules on an Attosecond Time Scale", *Science* **312**, 424 (2006).

[4] F. Krausz and M. Ivanov, "Attosecond physics", *Rev. Mod. Phys.* **81**, 163 (2009).

[5] J. Itatani, J. Levesque, D. Zeidler, H. Niikura, H. Pépin, J. C. Kieffer, P. B. Corkum, and D. M. Villeneuve, "Tomographic imaging of molecular orbitals", *Nature* **432**, 867 (2004).

[6] M. Lein, "Molecular imaging using recolliding electrons", *J. Phys. B* **40**, R135 (2007).

[7] O. Smirnova, Y. Mairesse, S. Patchkovskii, N. Dudovich, D. Villeneuve, P. Corkum, and M. Y. Ivanov, "High harmonic interferometry of multi-electron dynamics in molecules", *Nature* **460**, 972 (2009).

[8] S. Haessler, J. Caillat, W. Boutu, C. Giovanetti-Teixeira, T. Ruchon, T. Auguste, Z. Diveki, P. Breger, A. Maquet, B. Carré, R. Taïeb, and P. Salières, "Attosecond imaging of molecular electronic wavepackets", *Nature Physics* **6**, 200 (2010).

[9] C. Z. Bisgaard, O. J. Clarkin, G. Wu, A. M. D. Lee, O. Geßner, C. C. Hayden, and A. Stolow, "Time-Resolved Molecular Frame Dynamics of Fixed-in-Space CS_2 Molecules", *Science* **323**, 1464 (2009).

[10] L. Holmegaard, J. L. Hansen, L. Kalhøj, S. L. Kragh, H. Stapelfeldt, F. Filsinger, J. Küpper, G. Meijer, D. Dimitrovski, M. Abu-samha, C. P. J. Martiny, and L. B. Madsen, "Photoelectron angular distributions from strong-field ionization of oriented molecules", *Nature Physics* **6**, 428 (2010).

[11] L. V. Keldysh, "Ionization in the field of a strong electromagnetic field", *J. Exp. Theor. Phys.* **47**, 1945 (1964).

[12] G. L. Yudin and M. Y. Ivanov, "Nonadiabatic tunnel ionization: Looking inside a laser cycle", *Phys. Rev. A* **64**, 013409 (2001).

[13] P. Agostini, F. Fabre, G. Mainfray, G. Petite, and N. K. Rahman, "Free-Free Transitions Following Six-Photon Ionization of Xenon Atoms", *Phys. Rev. Lett.* **42**, 1127 (1979).

[14] J. Ullrich, R. Moshammer, A. Dorn, R. Dörner, L. Schmidt, and H. Schmidt-Böcking, "Recoil-ion and electron momentum spectroscopy: reaction-microscopes", *Rep. Prog. Phys.* **66**, 1463 (2003).

[15] M. Meckel, D. Comtois, D. Zeidler, A. Staudte, D. Pavičić, H. C. Bandulet, H. Pépin, J. C. Kieffer, R. Dörner, D. M. Villeneuve, and P. B. Corkum, "Laser-induced Electron Tunneling and Diffraction", *Science* **320**, 1478 (2008).

[16] V. Kumarappan, L. Holmegaard, C. Martiny, C. B. Madsen, T. K. Kjeldsen, S. S. Viftrup, L. B. Madsen, and H. Stapelfeldt, "Multiphoton Electron Angular Distributions from Laser-Aligned CS_2 Molecules", *Phys. Rev. Lett.* **100**, 093006 (2008).

[17] J. D. Jackson, *Classical Electrodynamics* (Wiley, New York, 1999).

[18] G. B. Arfken and H. J. Weber, *Mathematical Methods For Physicists* (Elsevier, Boston, 2005).

[19] L. B. Madsen, Ph.D. thesis, Institute of Physics and Astronomy, University of Aarhus, 1998.

[20] L. B. Madsen, "Gauge invariance in the interaction between atoms and few-cycle laser pulses", *Phys. Rev. A* **65**, 053417 (2002).

[21] E. Cormier and P. Lambropoulos, "Optimal gauge and gauge invariance in non-perturbative time-dependent calculation of above-threshold ionization", *J. Phys. B* **29**, 1667 (1996).

[22] T. K. Kjeldsen and L. B. Madsen, "Strong-field ionization of N_2: length and velocity gauge strong-field approximation and tunnelling theory", *J. Phys. B* **37**, 2033 (2004).

[23] T. K. Kjeldsen and L. B. Madsen, "Strong-field ionization of diatomic molecules and companion atoms: Strong-field approximation and tunneling theory including nuclear motion", *Phys. Rev. A* **71**, 023411 (2005).

[24] D. Bauer, D. B. Milošević, and W. Becker, "Strong-field approximation for intense-laser-atom processes: The choice of gauge", *Phys. Rev. A* **72**, 023415 (2005).

[25] K. C. Kulander, K. J. Schafer, and J. L. Krause, *Atoms in Intense Laser Fields* (Academic Press, New York, 1992).

[26] T. K. Kjeldsen, Ph.D. thesis, Department of Physics and Astronomy, University of Aarhus, 2007.

[27] H. G. Muller, "An efficient Propagation Scheme for the Time-Dependent Schrödinger Equation in the velocity Gauge", *Laser Phys.* **9**, 138 (1999).

[28] T. K. Kjeldsen, L. A. A. Nikolopoulos, and L. B. Madsen, "Solving the m-mixing problem for the three-dimensional time-dependent Schrödinger equation by rotations: Applications to strong-field ionization of H_2^+", *Phys. Rev. A* **75**, 063427 (2007).

[29] R. N. Zare, *Angular Momentum* (Wiley-Interscience, New York, 1988).

[30] M. Bouten, "On the rotation operators in quantum mechanics", *Physica* **42**, 572 (1969).

[31] E. Cormier and P. Lambropoulos, "Effect of the initial phase of the field in ionization by ultrashort laser pulses", *Eur. Phys. J. D* **2**, 15 (1998).

[32] G. G. Paulus, F. Grasbon, H. Walther, P. Villoresi, M. Nisoli, S. Stagira, E. Priori, and S. D. Silvestri, "Absolute-phase phenomena in photoionization with few-cycle laser pulses", *Nature* **414**, 182 (2001).

[33] S. Chelkowski and A. D. Bandrauk, "Sensitivity of spatial photoelectron distributions to the absolute phase of an ultrashort intense laser pulse", *Phys. Rev. A* **65**, 061802 (2002).

[34] A. Baltuška, T. Udem, M. Uiberacker, M. Hentschel, E. Goulielmakis, C. Gohle, R. Holzwarth, V. S. Yakovlev, A. Scrinzi, T. W. Hänsch, and F. Krausz, "Attosecond control of electronic processes by intense light fields", *Nature* **421**, 611 (2003).

[35] G. G. Paulus, F. Lindner, H. Walther, A. Baltuška, E. Goulielmakis, M. Lezius, and F. Krausz, "Measurement of the Phase of Few-Cycle Laser Pulses", *Phys. Rev. Lett.* **91**, 253004 (2003).

[36] M. F. Kling, C. Siedschlag, A. J. Verhoef, J. I. Khan, M. Schultze, T. Uphues, Y. Ni, M. Uiberacker, M. Drescher, F. Krausz, and M. J. J. Vrakking, "Control of Electron Localization in Molecular Dissociation", *Science* **312**, 246 (2006).

[37] C. P. J. Martiny and L. B. Madsen, "Symmetry of Carrier-Envelope Phase Difference Effects in Strong-Field, Few-Cycle Ionization of Atoms and Molecules", *Phys. Rev. Lett.* **97**, 093001 (2006).

[38] V. Roudnev and B. D. Esry, "General Theory of Carrier-Envelope Phase Effects", *Phys. Rev. Lett.* **99**, 220406 (2007).

[39] J. J. Hua and B. D. Esry, "The role of mass in the carrier-envelope phase effect for H_2^+ dissociation", *J. Phys. B* **42**, 085601 (2009).

[40] J. J. Sakurai, *Modern Quantum Mechanics* (Addison-Wesley, Reading, Massachusetts, 1994).

[41] F. H. M. Faisal, "Multiple absorption of laser photons by atoms", *J. Phys. B* **6**, L89 (1973).

[42] H. R. Reiss, "Effect of an intense electromagnetic field on a weakly bound system", *Phys. Rev. A* **22**, 1786 (1980).

[43] M. Lewenstein, P. Balcou, M. Y. Ivanov, A. L'Hullier, and P. B. Corkum, "Theory of high-harmonic generation by low-frequency laser fields", *Phys. Rev. A* **49**, 2117 (1994).

[44] M. Y. Ivanov, M. Spanner, and O. Smirnova, "Anatomy of strong field ionization", *J. Mod. Opt.* **52**, 165 (2005).

[45] A. de Bohan, B. Piraux, L. Ponce, R. Taïeb, V. Véniard, and A. Marquet, "Direct and Indirect Pathways in Strong Field Atomic Ionization", *Phys. Rev. Lett.* **89**, 113002 (2002).

[46] O. Smirnova, M. Spanner, and M. Ivanov, "Coulomb and polarization effects in sub-cycle dynamics of strong-field ionization", *J. Phys. B* **39**, S307 (2006).

[47] D. Arbó, J. E. Miraglia, M. S. Gravielle, K. Schiessl, E. Persson, and J. Burgdörfer, "Coulomb-Volkov approximation for near-threshold ionization by short laser pulses", *Phys. Rev. A* **77**, 013401 (2008).

[48] G. F. Gribakin and M. Y. Kuchiev, "Multiphoton detachment of electrons from negative ions", *Phys. Rev. A* **55**, 3760 (1997).

[49] B. Bergues, Z. Ansari, D. Hanstorp, and I. Y. Kiyan, "Photodetachment in a strong laser field: An experimental test of Keldysh-like theories", *Phys. Rev. A* **75**, 063415 (2007).

[50] B. Bergues, Z. Ansari, D. Hanstorp, and I. Y. Kiyan, "Reply to: Comment on: Photodetachment in a strong laser field: An experimental test of Keldysh-like theories", *Phys. Rev. A* **77**, 067402 (2008).

[51] Y. J. Chen and B. Hu, "Strong-field approximation for diatomic molecules: Comparison between the length gauge and the velocity gauge", *Phys. Rev. A* **80**, 033408 (2009).

[52] V. I. Usachenko and S.-I. Chu, "Strong-field ionization of laser-irradiated light homonuclear diatomic molecules: A generalized strong-field approximation linear combination of atomic orbitals model", *Phys. Rev. A* **71**, 063410 (2005).

[53] H. R. Reiss, "Comment on: Photodetachment in a strong laser field: An experimental test of Keldysh-like theories", *Phys. Rev. A* **77**, 067401 (2008).

[54] V. I. Usachenko, P. E. Pyak, and V. V. Kim, "Comparative study of strong-field ionization in laser-irradiated F_2 and other diatomic molecules: Density-functional-theory-based molecular strong-field approximation", *Phys. Rev. A* **79**, 023415 (2009).

[55] N. Bleistein and R. Handelsman, *Asymptotic Expansions of Integrals* (Holt, Rinehart and Winston, New York, 1975).

[56] D. B. Milošević, G. G. Paulus, D. Bauer, and W. Becker, "Above-threshold ionization by few-cycle pulses", *J. Phys. B* **39**, R203 (2006).

[57] W. H. Press, S. A. Teukolsky, W. T. Vetterling, and B. P. Flannery, *Numerical Recipes in Fortran* (Cambridge University Press, Cambridge, 1992).

[58] P. B. Corkum, "Plasma perspective on strong field multiphoton ionization", *Phys. Rev. Lett.* **71**, 1994 (1993).

[59] D. B. Milošević, G. G. Paulus, and W. Becker, "Phase-Dependent Effects of a Few-Cycle Laser Pulse", *Phys. Rev. Lett.* **89**, 153001 (2002).

[60] P. Salières, B. Carré, L. D. Déroff, F. Crasbon, G. G. Paulus, H. Walther, R. Kopold, W. Becker, D. B. Milošević, A. Sanpera, and M. Lewenstein, "Feynman's Path-Integral Approach for Intense-Laser-Atom Interactions", *Science* **292**, 902 (2001).

[61] P. Eckle, A. N. Pfeiffer, C. Cirelli, A. Staudte, R. Dörner, H. G. Muller, M. Büttiker, and U. Keller, "Attosecond Ionization and Tunneling Delay Time Measurements in Helium", *Science* **322**, 1525 (2008).

[62] M. V. Ammosov, N. B. Delone, and V. P. Krainov, "Tunnel ionization of complex atoms and atomic ions by an alternating electromagnetic field", *Sov. Phys. JETP.* **64**, 1191 (1986).

[63] A. Rudenko, K. Zrost, C. D. Schröter, V. L. B. de Jesus, B. Feuerstein, R. Moshammer, and J. Ullrich, "Resonant structures in the low-energy electron continuum for single ionization of atoms in the tunnelling regime", *J. Phys. B* **37**, L407 (2004).

[64] C. M. Maharjan, A. S. Alnaser, I. Litvinyuk, P. Ranitovic, and C. L. Cocke, "Wavelength dependence of momentum-space images of low-energy electrons generated by short intense laser pulses at high intensities", *J. Phys. B* **39**, 1955 (2006).

[65] T. Morishita, Z. Chen, S. Watanabe, and C. D. Lin, "Two-dimensional electron momentum spectra of argon ionized by short intense lasers: Comparison of theory with experiment", *Phys. Rev. A* **75**, 023407 (2007).

[66] D. G. Arbó, K. I. Dimitriou, E. Persson, and J. Burgdörfer, "Sub-Poissonian angular momentum distribution near threshold in atomic ionization by short laser pulses", *Phys. Rev. A* **78**, 013406 (2008).

[67] M. Abu-samha, D. Dimitrovski, and L. B. Madsen, "The role of the atomic potential in the regime of strong-field tunnelling ionization: imprints on longitudinal and 2D momentum distributions", *J. Phys. B* **41**, 245601 (2008).

[68] M. Bashkansky, P. H. Bucksbaum, and D. W. Schumacher, "Asymmetries in Above-Threshold Ionization", *Phys. Rev. Lett.* **60**, 2458 (1988).

[69] S. P. Goreslavski, G. G. Paulus, S. V. Popruzhenko, and N. I. Shvetsov-Shilovski, "Coulomb Asymmetry in Above-Threshold Ionization", *Phys. Rev. Lett.* **93**, 233002 (2004).

[70] H. G. Muller, G. Petite, and P. Agostini, "Comment on: Asymmetries in Above-Threshold Ionization", *Phys. Rev. Lett.* **61**, 2507 (1988).

[71] A. Jaroń, J. Z. Kamiński, and F. Ehlotzky, "Asymmetries in the angular distributions of above threshold ionization in an elliptically polarized laser field", *Opt. Commun.* **163**, 115 (1999).

[72] S. V. Popruzhenko, G. G. Paulus, and D. Bauer, "Coulomb-corrected quantum trajectories in strong-field ionization", *Phys. Rev. A* **77**, 053409 (2008).

[73] D. Pavičić, K. F. Lee, D. M. Rayner, P. B. Corkum, and D. M. Villeneuve, "Direct Measurement of the Angular Dependence of Ionization for N_2, O_2, and CO_2 in Intense Laser Fields", *Phys. Rev. Lett.* **98**, 243001 (2007).

[74] G. G. Paulus, F. Grasbon, A. Dreischuh, H. Walther, R. Kopold, and W. Becker, "Above-Threshold Ionization by an Elliptically Polarized Field: Interplay between Electronic Quantum Trajectories", *Phys. Rev. Lett.* **84**, 3791 (2000).

[75] G. Duchateau, E. Cormier, and R. Gayet, "Coulomb-Volkov approach of ionization by extreme-ultraviolet laser pulses in the subfemtosecond regime", *Phys. Rev. A* **66**, 023412 (2002).

[76] M. R. C. McDowell and J. P. Coleman, *Introduction to the Theory of Ion-Atom Collisions* (North-Holland, Amsterdam, 1970).

[77] R. Baumfalk, N. H. Nahler, and U. Buck, "Photodissociation of oriented HXeI molecules in the gas phase", *J. Chem. Phys.* **114**, 4755 (2001).

[78] H. Sakai, S. Minemoto, H. Nanjo, H. Tanji, and T. Suzuki, "Controlling the Orientation of Polar Molecules with Combined Electrostatic and Pulsed, Nonresonant Laser Fields", *Phys. Rev. Lett.* **90**, 083001 (2003).

[79] H. Tanji, S. Minemoto, and H. Sakai, "Three-dimensional molecular orientation with combined electrostatic and elliptically polarized laser fields", *Phys. Rev. A* **72**, 063401 (2005).

[80] U. Buck and M. Farnik, "Oriented xenon hydride molecules in the gas phase", *Int. Rev. Phys. Chem.* **25**, 583 (2006).

[81] L. Holmegaard, J. H. Nielsen, I. Nevo, H. Stapelfeldt, F. Filsinger, J. Küpper, and G. Meijer, "Laser-Induced Alignment and Orientation of Quantum-State-Selected Large Molecules", *Phys. Rev. Lett.* **102**, 023001 (2009).

[82] I. Nevo, L. Holmegaard, J. H. Nielsen, J. L. Hansen, H. Stapelfeldt, F. Filsinger, G. Meijer, and J. Küpper, "Laser-induced 3D alignment and orientation of quantum state-selected molecules", *Phys. Chem. Chem. Phys.* **11**, 9912 (2009).

[83] M. Abu-samha and L. B. Madsen, "Single-active-electron potentials for molecules in intense laser fields", *Phys. Rev. A* **81**, 033416 (2010).

[84] M. W. Schmidt, K. K. Baldridge, J. A. Boatz, S. T. Elbert, M. S. Gordon, J. H. Jensen, S. Koseki, N. Matsunaga, K. A. Nguyen, S. Su, T. L. Windus, M. Dupuis, and J. A. Montgomery, "General atomic and molecular electronic structure system", *J. Comput. Chem.* **14**, 1347 (1993).

[85] X. M. Tong, Z. X. Zhao, and C. D. Lin, "Theory of molecular tunneling ionization", *Phys. Rev. A* **66**, 033402 (2002).

[86] C. B. Madsen, A. S. Mouritzen, T. K. Kjeldsen, and L. B. Madsen, "Effects of orientation and alignment in high-order harmonic generation and above-threshold ionization", *Phys. Rev. A* **76**, 035401 (2007).

[87] J. Ortigoso, M. Rodriguez, M. Gupta, and B. Friedrich, "Time evolution of pendular states created by the interaction of molecular polarizability with a pulsed nonresonant laser field", *J. Chem. Phys.* **110**, 3870 (1999).

[88] S.-K. Son and S.-I. Chu, "Multielectron effects on the orientation dependence and photoelectron angular distribution of multiphoton ionization of CO_2 in strong laser fields", *Phys. Rev. A* **80**, 011403 (2009).

[89] M. Abu-samha and L. B. Madsen, "Theory of strong-field ionization of aligned CO_2", *Phys. Rev. A* **80**, 023401 (2009).

[90] S.-F. Zhao, C. Jin, A.-T. Le, T. F. Jiang, and C. D. Lin, "Analysis of angular dependence of strong-field tunneling ionization for CO_2", *Phys. Rev. A* **80**, 051402 (2009).

[91] M. Spanner and S. Patchkovskii, "One-electron ionization of multielectron systems in strong nonresonant laser fields", *Phys. Rev. A* **80**, 063411 (2009).

[92] S. Petretti, Y. V. Vanne, A. Saenz, A. Castro, and P. Decleva, "Alignment-Dependent Ionization of N_2, O_2 and CO_2 in Intense Laser Fields", *Phys. Rev. Lett.* **104**, 223001 (2010).

[93] P. Eckle, M. Smolarski, P. Schlup, J. Biegert, A. Staudte, M. Schöffler, H. G. Muller, R. Dörner, and U. Keller, "Attosecond angular streaking", *Nature Physics* **4**, 565 (2008).

[94] A. Staudte, S. Patchkovskii, D. Pavičić, H. Akagi, O. Smirnova, D. Zeidler, M. Meckel, D. M. Villeneuve, R. Dörner, M. Y. Ivanov, and P. B. Corkum, "Angular Tunneling Ionization Probability of Fixed-in-Space H_2 Molecules in Intense Laser Pulses", *Phys. Rev. Lett.* **102**, 033004 (2009).

[95] M. Magrakvelidze, F. He, S. De, I. Bocharova, D. Ray, U. Thumm, and I. V. Litvinyuk, "Angular dependence of the strong-field ionization measured in randomly oriented hydrogen molecules", *Phys. Rev. A* **79**, 033408 (2009).

[96] C. P. J. Martiny, M. Abu-samha, and L. B. Madsen, "Counterintuitive angular shifts in the photoelectron momentum distribution for atoms in strong few-cycle circularly polarized laser pulses", *J. Phys. B* **42**, 161001 (2009).

[97] T. K. Kjeldsen, C. Z. Bisgaard, L. B. Madsen, and H. Stapelfeldt, "Role of symmetry in strong-field ionization of molecules", *Phys. Rev. A* **68**, 063407 (2003).

[98] T. K. Kjeldsen, C. Z. Bisgaard, L. B. Madsen, and H. Stapelfeldt, "Influence of molecular symmetry on strong-field ionization: Studies on ethylene, benzene, fluorobenzene and chlorofluorobenzene", *Phys. Rev. A* **71**, 013418 (2005).

[99] M. Busuladžić, A. Gazibegović-Busuladžić, D. B. Milošević, and W. Becker, "Angle-Resolved High-Order Above-Threshold Ionization of a Molecule: Sensitive Tool for Molecular Characterization", *Phys. Rev. Lett.* **100**, 203003 (2008).

[100] H. G. Muller and F. C. Kooiman, "Bunching and Focusing of Tunneling Wave Packets in Enhancement of High-Order Above-Threshold Ionization", *Phys. Rev. Lett.* **81**, 1207 (1998).

[101] H. Akagi, T. Otobe, A. Staudte, A. Shiner, F. Turner, R. Dörner, D. M. Villeneuve, and P. B. Corkum, "Laser Tunnel Ionization from Multiple Orbitals in HCl", *Science* **325**, 1364 (2009).

[102] J. L. Hansen, L. Holmegaard, L. Kalhøj, S. L. Kragh, H. Stapelfeldt, F. Filsinger, J. Küpper, G. Meijer, D. Dimitrovski, M. Abu-samha, C. P. J. Martiny, and L. B. Madsen, submitted to Phys. Rev. A (unpublished).

[103] B. H. Bransden and C. J. Joachain, *Physics of Atoms and Molecules* (Prentice Hall, Harlow, England, 2003).

[104] I. S. Gradshteyn and I. M. Ryzhik, *Table of Integrals, Series, and Products* (Academic Press, New York, 2000).

[105] Y. V. Vanne and A. Saenz, "Exact Keldysh theory of strong-field ionization: Residue method versus saddle-point method", *Phys. Rev. A* **75**, 033403 (2007).